DEPOSITIONAL PROCESSES AND RESERVOIR

QUALITY OF THE LOWER PERMIAN WOLFCAMP

FORMATION IN THE DELAWARE BASIN, WEST

TEXAS

By

MARIA T. REISTROFFER

Bachelor of Science in Geology

The University of Texas at Austin

Austin, TX

2017

DEPOSITIONAL PROCESSES AND RESERVOIR

QUALITY OF THE LOWER PERMIAN WOLFCAMP

FORMATION IN THE DELAWARE BASIN, WEST

TEXAS

Thesis Approved:

Dr. G. Michael Grammer

Thesis Adviser

Dr. Jay Gregg

Dr. James Puckette

ACKNOWLEDGEMENTS

I would like to sincerely thank my advisor Dr. Michael Grammer for his guidance and encouragement throughout the time I've spent at Oklahoma State University. I am grateful for the tremendous amount of knowledge he's shared and for constantly reminding me to ask important questions such as "so what?". Thank you to Devon Energy for providing the dataset and to the AAPG Foundation and Oklahoma Geological Foundation for contributing to the funding of this thesis.

Additionally, I would like to thank the past and present members of the carbonate reservoir characterization lab group, especially McKensie Mitsdarffer, Ibukun Bode, Yulun Wang, Julie Cains, and Alejandra Santiago Torres for collaborating and for their assistance in editing my thesis. Thank you to my committee members Dr. Jim Puckette and Dr. Jay Gregg for their interest and input, family, friends, and faculty of the BPSOG that have helped me along the way.

I dedicate this thesis to my loving parents, John and Mitzi Reistroffer. Without their unwavering support, none of this would have been possible.

Name: MARIA T. REISTROFFER

Date of Degree: MAY, 2021

Title of Study: DEPOSITIONAL PROCESSES AND RESERVOIR QUALITY OF THE LOWER PERMIAN WOLFCAMP FORMATION IN THE DELAWARE BASIN, WEST TEXAS

Major Field: GEOLOGY

Abstract: The Delaware Basin, located in southeast New Mexico and west Texas, is the westernmost sub-basin of the Permian Basin. With an estimated 24 billion barrels of recoverable oil, the lower Permian Wolfcamp Formation is one of the most productive unconventional petroleum systems in the U.S. and is characterized by significant lateral and vertical heterogeneity in a mixed carbonate-siliciclastic system. Understanding the depositional processes and petrophysical parameters associated with the reservoir facies in the lower Permian Wolfcamp Formation has major implications for maximizing hydrocarbon production.

Upper Wolfcamp A lithologies in the Delaware Basin vary from calcareous and siliciclastic organic–rich mudstones, siltstones, wackestones, and grain dominated packstones. These Leonardian-aged slope to basin deposits were primarily sourced from the adjacent carbonate-dominated Central Basin Platform and the siliciclastic-dominated Northwest Shelf. As a result, upper Wolfcamp sedimentation is dominated by a mix of carbonate and siliciclastic sediment gravity flow deposits. These deposits are driven by high amplitude global sea level fluctuations associated with the growth and ablation of continental ice during Permian icehouse conditions. During these periods of eustatic fluctuation, increased siliciclastic bypass and deposition into the Basin occurred during low-stands of sea level. Carbonate materials dominated transgressive and highstand sedimentation, with carbonate detritus being shed off the Central Basin Platform.

This study evaluates the reservoir quality of two Wolfcamp A cores in the west Texas area of the Delaware Basin and how reservoir quality in these cores varies on a sub-meter scale as a result of depositional processes and diagenesis. The integration of datasets including cores, thin sections, wireline logs, and laboratory measured petrophysical properties, illustrates that the Wolfcamp A is heterogeneous in composition and characterized by low porosity and varying permeability. The pore system architecture is analyzed using ion milled environmental scanning electron microscopy (ESEM) and digital image analysis of micro- to nanometer scale pores. Siliceous and argillaceous mudstones to siltstones show simpler pore structures and overall larger pores that contribute to higher permeability in measured core samples. In contrast, carbonate mudstones to packstones have complex pore structures and smaller pores that contribute less to permeability in samples measured from core.

TABLE OF CONTENTS

LIST OF TABLES

LIST OF FIGURES

Figure   Page

CHAPTER I

INTRODUCTION

In 2017, the Permian Basin produced a record of 815 million barrels of oil, making it one of the most productive unconventional hydrocarbon plays in the United States (Ortega, 2017). With a large volume of the targeted reservoirs derived from slope to basin gravity flow deposits, it is essential to understand the spatial and temporal distribution of these deep-water facies, and on a sub-meter scale, the associated pore types and pore structures that can be related to permeability and increased hydrocarbon recovery.

Within the western sub-basin of the Permian Basin lies the Delaware Basin (Figure 1a). Located in northwest Texas and southeast New Mexico, the Wolfcamp formation (Early Permian and Leonardian in age) is characterized by significant lateral and vertical heterogeneity in a mixed carbonate-siliciclastic system (Kvale et al., 2019; Playton and Kerans, 2002). Identifying the depositional processes controlling sedimentation of the lower Permian Wolfcamp Formation is essential for facies characterization, reservoir quality, and the determination of probable geometrical attributes. The Wolfcamp A formation is divided into three units: upper Wolfcamp A, middle Wolfcamp A, and lower Wolfcamp A (Figure 2). This study focuses on the complex, mixed siliciclastic-carbonate sedimentation and petrophysical properties of the upper Wolfcamp A. Lithologies within the upper Wolfcamp A range from calcareous and siliciclastic organic–rich

mudstones, siltstones, wackestones, packstones, grainstones, and megabreccias. Targets for horizontal drilling and hydraulic fracturing in this play are the siliceous and argillaceous mudstones to siltstones that are associated with the upper Bouma sequence, planar laminated muddy turbidites (Td) and massive to graded muddy turbidites (Te). Average porosity and permeability values in these target zones are 11% and 1.4 microdarcies (μd). Lithologic changes are characterized by both sharp, abrupt contacts and gradational contacts (Kvale et al., 2019). Vertical facies variations occur on the centimeter to decimeter scale. Each facies contain unique petrophysical properties including porosity, permeability, as well as various diagenetic overprints. Recognizing these lithologic patterns in the core on a finer scale (cm) can help to create more accurate petrophysical models through the upscaling process to enhance reservoir characterization and hydrocarbon recovery in the Wolfcamp Formation.

Gravity flow deposits in the Delaware Basin can be related to transgressive to highstand carbonate shedding (a topic originally discussed by Eberli 1991; Grammer and Ginsburg, 1992; Handford and Loucks 1993; Mullins et al. 1984; Schlager et al. 1994; Shanmugam and Moiola 1984) and Ouachita-related tectonism persisting throughout the lower Permian (Playton and Kerans, 2002). Based on these previous investigations, the carbonate dominated gravity flow deposits in the Wolfcamp A of the Delaware Basin were likely sourced during transgressions and early highstands by the mobilization of large volumes of carbonate materials derived from the margin and proximal foreslope of the Central Basin Platform. The temporal and spatial distribution of these gravity flow deposits resulted in a combination of cyclically-stacked, channelized, and likely amalgamated, sub-meter scale turbidites and debris flow deposits divided by pelagic and hemipelagic siltstone and mudstone, with the majority of siliciclastic input deposited during lowstands of sea-level.

Identifying the facies, distribution, and pore architecture associated with heterogeneous gravity flow deposits has direct implications on reservoir quality and distribution in the

subsurface. Understanding these relationships results in the production of more accurate facies and petrophysical models. This study uses an integrated approach involving core and petrographic analysis, and environmental scanning electron microscopy (ESEM) of core plug samples to:

1. Identify the major depositional facies and distribution of sediment gravity flow deposits within two Wolfcamp A cores in a detailed cm-scale core description and provide a first-order interpretation on the subsurface distribution of the different deposit types.

2. Assess pore systems architecture of the major facies using digital image analysis of ion milled ESEM photomicrographs in conjunction with laboratory measured porosity and permeability.

3. Evaluate the relationship between pore type, pore system architecture, and permeability as a means to develop a proxy for predicting permeability that can be potentially applied to other mixed carbonate-siliciclastic mudrock units.

CHAPTER II

GEOLOGIC BACKGROUND

2.1 Location

The Delaware Basin, located in northwest Texas and southeast New Mexico is the westernmost sub-basin of the Permian Basin (Figure 1). It covers an area of approximately 33,500 km^2 (Hill, 1996). The Central Basin Platform (CBP) is located directly east of the Delaware Basin, and the Northwest Shelf, a shallow-water carbonate shelf, borders the northern margin of the Basin (Figure 1). It is bounded to the west and southwest by the Diablo Platform, Marfa Basin and Hovey Channel (Figure 1). On the southern edge, the Marathon-Ouachita Fold and Thrust Belt border the Basin (Hill, 1996).
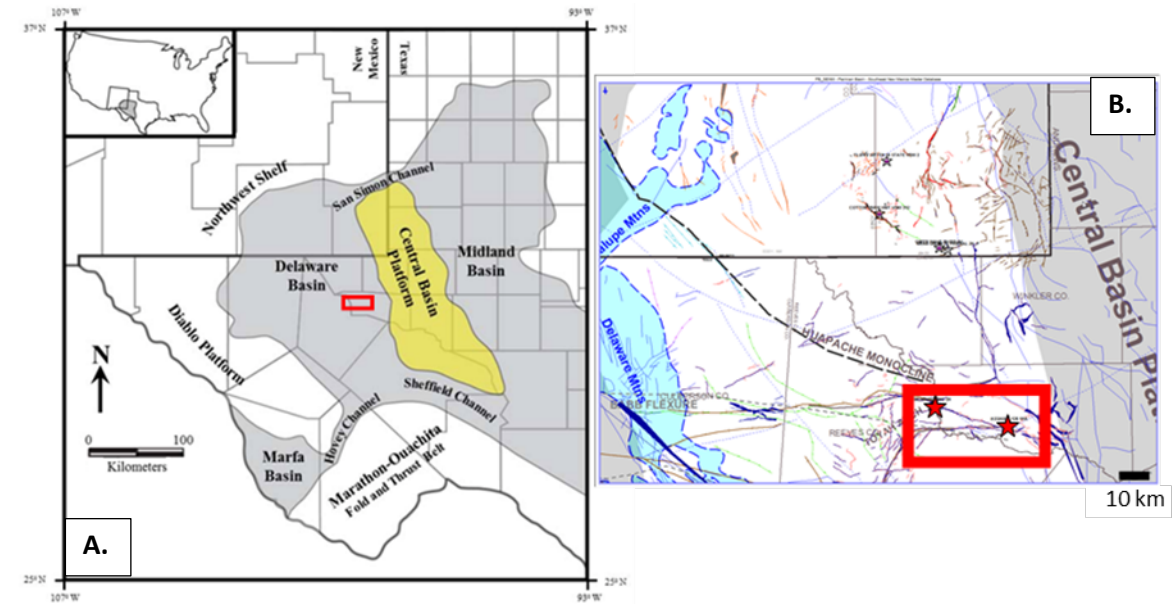
Figure 1: Map of the Permian Basin (A). Structural elements of the Delaware Basin (B). The red box in (A) and in (B) indicates the area of study, and the two red stars in (B) represent the two northwest Texas cores being utilized in this study (Modified from Asmus and Grammer (A), 2013 and Devon Energy (B), 2018).

2.2 Geologic History

A major tectonic event initiated the formation and later deformation of the Permian Basin north of the Marathon-Ouachita orogenic fold and thrust belt beginning in Late Mississippian (~326 Ma) through most of the Permian (~253 MA). This tectonic episode occurred concurrently with the aggregation of Laurasia, Gondwana, and African continental plates as Pangea (Schumaker, 1992). Active tectonism (east-west compressional stress) in the late Mississippian caused the reactivation of deep Precambrian basement faults, which eventually led to the uplift of the Central Basin Platform and the separation of the original Tabosa Basin into two sub-basins: 1) the Delaware Basin in the west, and 2) the Midland Basin to the east (Hill, 1996; Hills, 1984; Schumaker, 1992). By the Late Wolfcampian, episodic platform failure mobilized carbonate detritus from the Central Basin Platform down the slope into the Delaware Basin. This basinward sedimentation occurred in the form of sediment gravity flows. Trigger mechanisms for the

mobilization of unstable sediment along the margin and foreslopes include oversteepening of the slope (Kenter, 1990), transgressive to highstands shedding related to high frequency sea level changes (Glaser and Droxler, 1991; Grammer and Ginsburg, 1992), storm events (Normark and Piper, 1991), and active tectonism throughout the lower Permian (Playton and Kerans, 2002). These mechanisms occur both coincidentally and independently from one another.

2.3 Paleogeography and Paleoclimate

During the lower Permian, the Delaware Basin was located near the equator with paleo-winds blowing from present day north-northeast to south-southwest (Fischer and Sarnthein, 1988). The presence of compound leaves of *peltaspermou*s plants from the Wolfcamp A in the Delaware Basin (predominantly *Germaropteris martinsii*) indicates a semiarid (1-2 wet months) paleoclimate (Kustatscher et al., 2014; Baumgardner et al., 2016).

The Permian marks a period of icehouse conditions in which high-amplitude eustatic fluctuations were driven by the growth and ablation of continental ice (Montañez, et al., 2007; Read, 1985; Rygel et al., 2008; Saller et al., 1989). During these periods of sea-level fluctuation, siliciclastic deposition dominated lowstands of sea level and carbonate deposition dominated transgression (Handford and Loucks, 1993).

2.4 Regional Stratigraphy

In this study, operational stratigraphic nomenclature is used. The Wolfcamp Formation in the Delaware Basin is Early Permian (Leonardian) in age and is a mixed, carbonate-siliciclastic system. It is subdivided from youngest to oldest into the upper A, middle A, and lower A (Figure 2). The Bone Spring Formation overlies the Wolfcamp in the Delaware Basin. This study focuses on two cores in the Delaware Basin representing the upper Wolfcamp A interval (Figure 2).
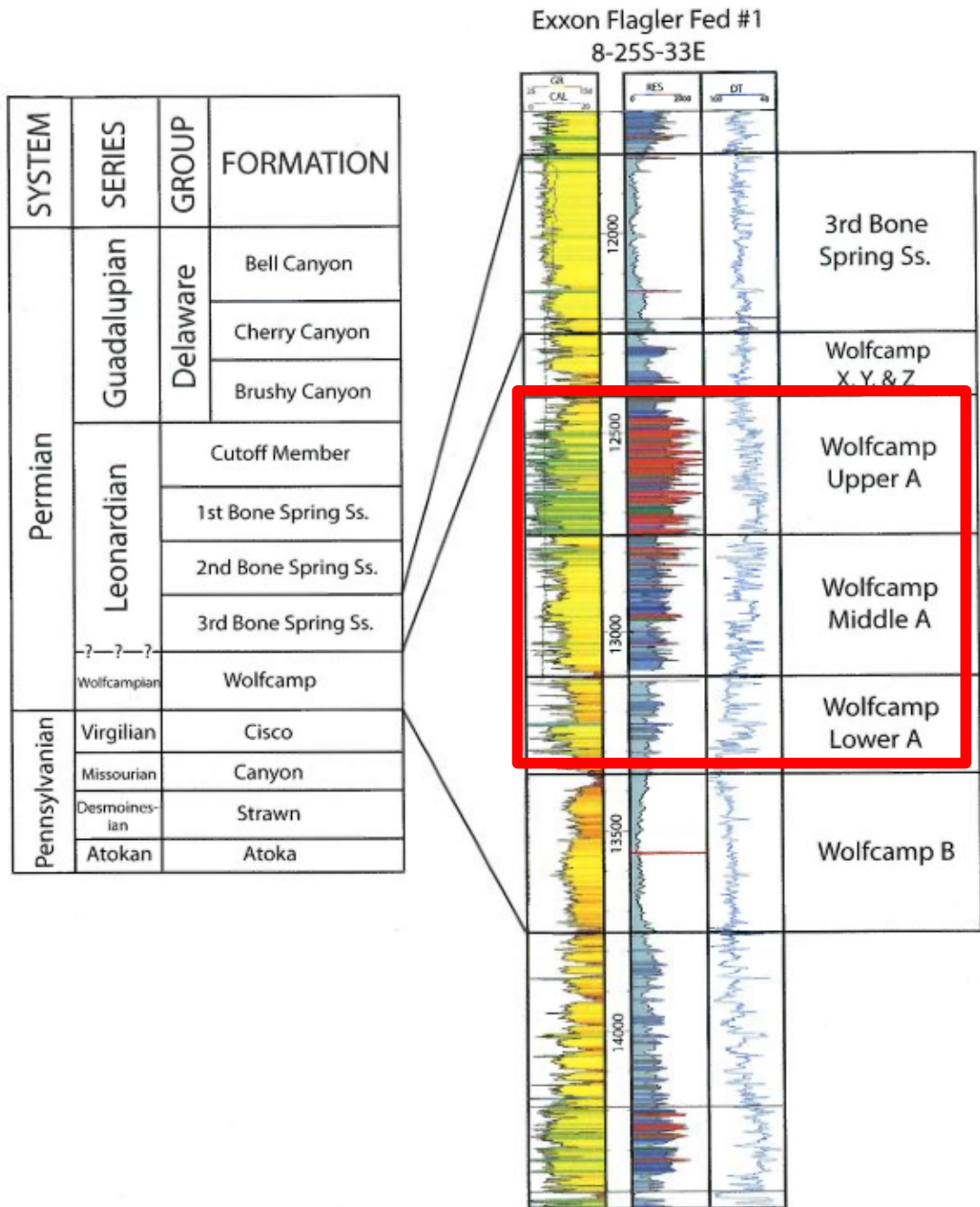
Figure 2: Stratigraphic nomenclature (operational) of the Lower Permian petroleum system showing the heterogeneous sandstones, carbonate rocks, and shale/mudstone lithologies in gamma-ray, resistivity, and delta T (transmission time). The red box identifies the Wolfcamp A in this study (Kvale et al., 2017).

2.5 Sediment Gravity Flows

Sediment gravity flows make up a significant volume of strata in slope and basinal settings and are thus a dominant strata type in deep-water sedimentary basins (Posamentier and Walker, 2006). Because of this, petroleum exploration efforts targeting these strata have recently focused on understanding the geometry, distribution, and depositional setting of these deposits. The two main gravity flow deposits observed in the cores of this study include: 1) debris flows and 2) turbidites. Mud dominated slumps, a type of sediment slide, are another less volumetrically significant gravity flow deposit observed in core. Table 1 summarizes important terminology and architectural attributes associated with sediment gravity flows in this study.

2.6 Debris Flows

Debris flows are cohesive laminar flows that originate from low relief (toe-of-slope and distal basin) and high relief (rimmed platform margins and upper slope) environments (Posamentier and Martinsen, 2011; Cook and Mullins, 1983). They are capable of traveling hundreds of kilometers across low depositional relief (<1 degree in slope declivity) (Cook and Mullins, 1983). The concentration of sediment volume down-slope creates lobate sheets or channel-like geometries (Asmus, 2012; Asmus and Grammer, 2013). Clasts within debris flows vary in size and composition, display massive, normal, or inverse grading, and protrude into overlying strata (Cook and Mullins, 1983; Mulder and Alexander, 2001). Figure 4 illustrates the characteristics associated with debris flow deposits of the Devonian foreslope strata in Alberta, Canada (Cook et al., 1972).
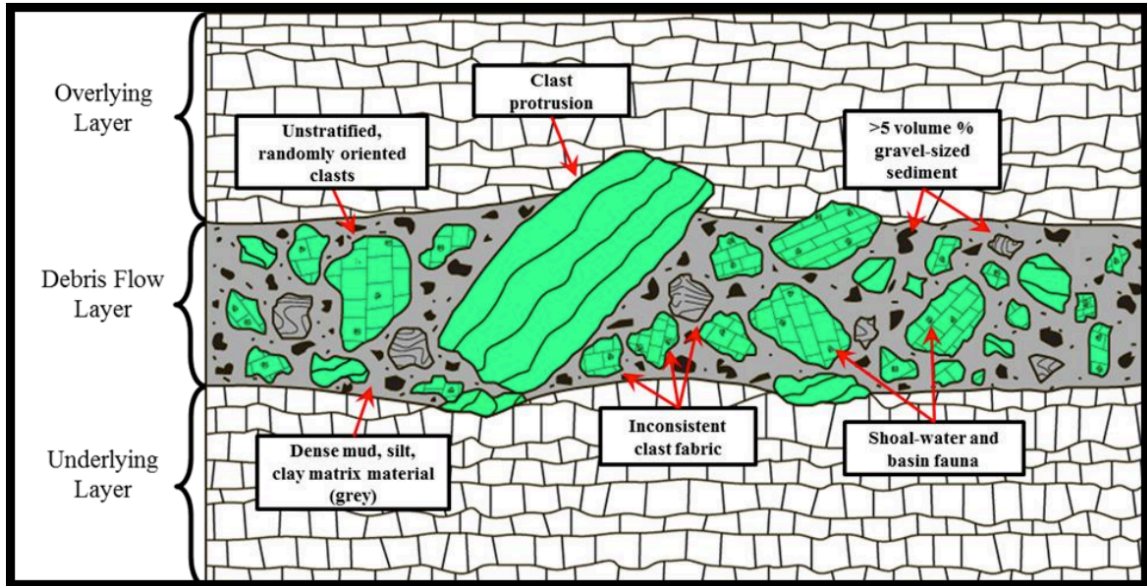
Figure 3: Schematic illustration of a carbonate debris flow layer typical of most carbonate debris flow deposits sourced from platform or slope settings (Modified from Cook and Mullins, 1984 by Asmus, 2012).

2.7 Turbidity Currents

Turbidity currents are a type of non-cohesive sediment gravity flow in which the sediment is supported by fluid turbulence within the flow body. Initial mobilization of turbidity currents can be triggered by storm events, hurricanes, tectonic activity, and highstand shedding in carbonate environments (Glaser and Droxler 1991; Eberli 1991; Grammer and Ginsburg 1992; Handford and Loucks 1993; Mullins et al. 1984; Playton and Kerans 2002; Schlager et al. 1994; and Shanmugam and Moiola 1984). Turbidites exhibit variable depositional geometry, spatial distribution, and distances over which the sediment is transported. Sediments associated with turbidites are variable in size which depends on flow origin and transport distance. Grain size in turbidites is an indicator of location within a deep water turbidite fan (Walker, 1978). Coarser grains indicate a deposition more proximal within the deep-water channel and upper fan, and finer grained deposits indicate a more distal position in the turbidite fan e.g. lower lobe fringe (Walker, 1978). Calcareous turbidites can be characterized using the Bouma sequence model in Bouma (1964). The following features are characteristic of turbidites: 1) thin to thick bedding

9

(millimeter to meter), 2) basal scour (flute) marks, 3) dewatering structures, 4) Bouma sequences

(Figure 5), 5) long travel distances (100's of kilometers), 6) cyclical stratigraphic occurrence

(Asmus, 2012). It is important to note that complete Bouma sequences are not always preserved

as a result of erosion, burial deformation, bioturbation, and successive sedimentation (Asmus,

2012).
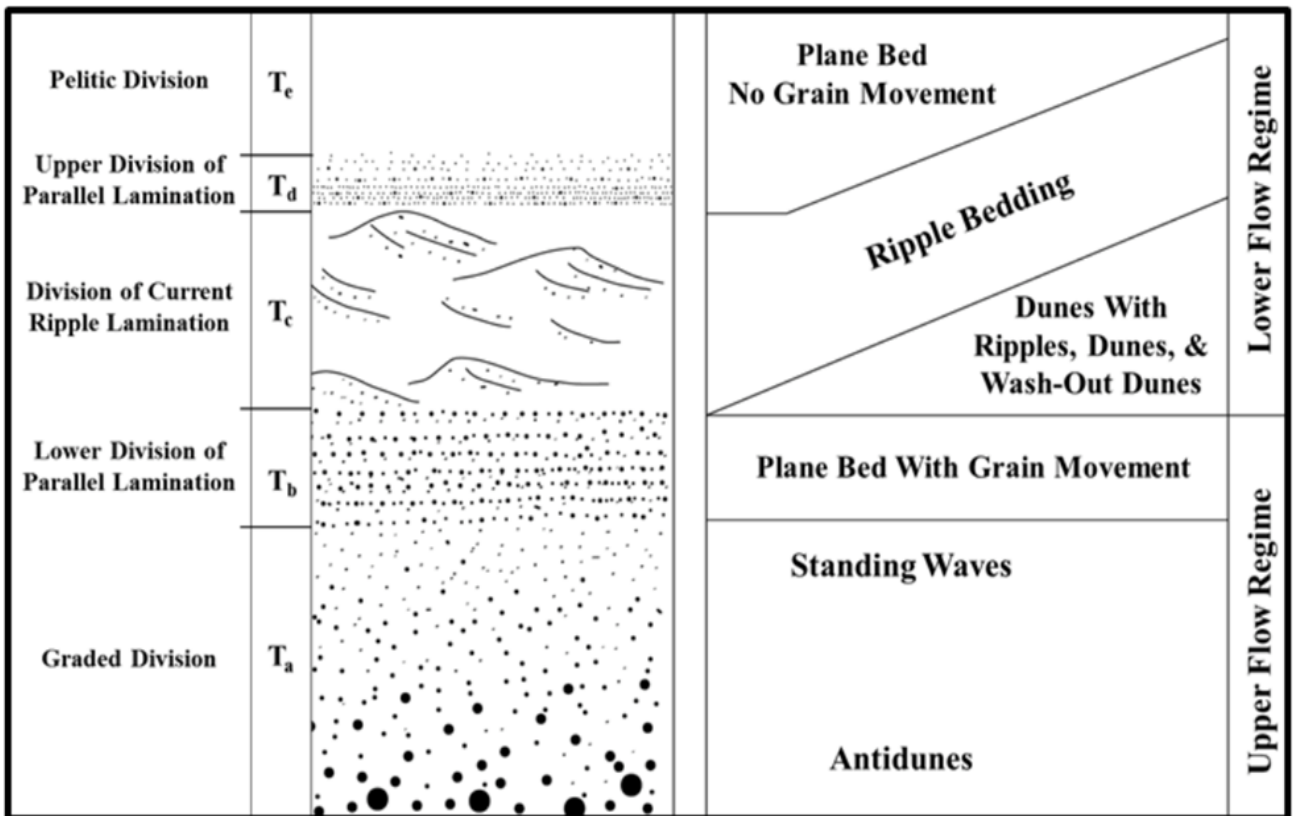
Figure 4: Bouma sequences (Ta-Te) illustrating the sedimentation of granule to clay-sized grains
transported by turbidity currents (Bouma 1964; Mutti et al., 1999; Asmus, 2012).

Flow Type		Flow Behavior	Flow Cohesion	Flow Character	Dominant Sediment Support Mechanism	Sediment Abundance (volume % of solid grains)	Architectural Elements
Source: Middleton and Hampton (1976); Lowe (1979, 1982); Nardin et al. (1979); Tripsanas et al. (2008)	Source: Mulder and Alexander (2001); Lowe (1979, 1982); Nardin et al. (1979)	Source: Lowe (1979, 1982); Nardin et al. (1979); Mulder and Alexander (2001)	Source: Lowe (1979, 1982); Nardin et al. (1979); Mulder and Alexander (2001)	Source: Lowe (1979, 1982); Nardin et al. (1979); Mulder and Alexander (2001)	Source: Lowe (1979, 1982); Nardin et al. (1979); Mulder and Alexander (2001)	Source: Mulder and Alexander (2001)	Source: Cook and Mullins (1983); Nardin et al (1979); Posamentier and Martinsen (2011); Lowe (1979, 1982); Tripsanas et al. (2008); Middleton and Hampton (1976); Mulder and Alexander (2001)
Turbidity Current	Low-Density Turbidity Current	Fluid	Non-Cohesive	Turbulent	Fluidal Turbulence	0-10 %	Variable bed thicknesses (millimeters-to-meters); basal scour marks; dewatering structures occurring at the base or top of individual depositional packages; partial-to-complete Bouma sequences; long travel distances (100's of kilometers); and cyclical stratigraphic occurrence (i.e. cyclical stacking of individual depositional packages)
Fluidized Flow	High Density Turbidity Current	Fluid	Non-Cohesive	Turbulent	Escaping Pore Fluids (completely support solid grains)	10-40 %	Dewatering structures occurring at the base or top of individual depositional packages; collapse structures; slight-to-moderate grading; and basal load structures.
Liquified Flow	Concentrated Density Flow	Fluid/ Plastic	Non-Cohesive	Turbulent/ Laminar	Escaping Pore Fluids (partially support solid grains)/ Dispersive Pressure (grain-to-grain collision)/ Buoyancy	10-40 %	Liquified flows exhibit greater runout distances compared to fluidized flows due to increased sediment concentrations of fine sand sized grains within the flow body
Grain Flow	Hyperconcentrated Density Flow	Plastic	Non-Cohesive	Laminar	Dispersive Pressure (grain-to-grain collision)/ Buoyancy	25-90 %	Massive bedding; sharp upper and lower bedding contacts; basal erosional features; local inverse grading; and sediment concentrations dominated by gravel-, sand-, and silt-sized grains
Debris Flow		Plastic	Cohesive	Laminar	Matrix Strength/ Buoyancy/ Pore Pressure	30-90 %	Massive bedding; clasts may exhibit random and chaotic fabrics with variations in size, roundness, and composition; clasts and matrix may contain shoal-water and basin fauna; internal deformational shearing; local inverse grading; and clast protrusion into underlying and/or overlying strata
Slides	Slump (rotational)	Elastic/ Plastic	na	na	na	na	Spoon-shaped external geometry; minimal internal deformation of bedding along central axis of flow body; significant internal deformation of bedding along basal surface and exterior margins of flow body; microfolding and microfaulting are common
	Glide (translational)	Elastic/ Plastic	na	na	na	na	Continuous bedding; planar basal surfaces; minimal internal deformation; local faulting (strike slip and listric) and folding may occur along the base and margins of the flow body

Table 1: Architectural attributes and terminology summarizing major components of turbidites, debris flows, and other gravity flow types to be used in this investigation. Data are collected from Middleton and Hampton (1976), Posamentier and Martinsen (2011), Tripsanas et al. (2008), and Mulder and Alexander (2001); created by Asmus (2012).

2.8 Trigger Mechanisms and Distribution of Sediment Gravity Flows

During Leonardian deposition, Northwest Shelf and Central Basin Platform slope angles varied due tectonic uplift. Declivities along the eastern side of the Northwest Shelf were greater (35°) compared to the western slope angles (3°) (Hunt and Fitchen, 1999, Kerans and Tinker, 1999, Janson et al., 2007). Furthermore, angles of repose in unconsolidated carbonate sediments vary from 3° to 45° and are dependent on several factors including grain size, sorting, and shape (Kenter, 1990). Sediment gravity flows are triggered by oversteepening of the slope, sea level fluctuation, storm events, and tectonic activity (Kenter, 1990; Glaser and Droxler, 1991; Grammer and Ginsburg, 1992; Normark and Piper, 1991; Playton and Kerans, 2002). All of these sediment gravity flow trigger mechanisms occurred both simultaneously and independently from one another during Leonardian deposition, resulting in heterogeneous sedimentation patterns that are observed in core. Further adding to the complexity of sedimentation and timing, gravity flows traveling down slope are capable of initiating other gravity flows and remobilizing sediment (e.g. debris flows triggering turbidites and vice versa; Normark and Piper, 1991; Houghton et al., 2003). There is also evidence of cogenetic or linked flow deposits where one type of gravity flow transforms into another type of flow depending on velocity, flow concentration, and grain types (Houghton et al., 2003). As a result, facies distribution both vertically and laterally are difficult to predict and are very heterogeneous.

The Wolfcampian to early Leonardian is a transitional period from Pennsylvanian Icehouse climate to Late Permian Greenhouse conditions. High amplitude (25-75 m) third-order sea level fluctuations during this period (Haq and Schutter, 2008) can drive cyclical sedimentation patterns and control carbonate production (Grammer and Ginsburg, 1992). Previous investigations have used the Great Bahama Bank (GBB) to illustrate the significant amount of carbonate sediment that is transported from the platform interior in the basinal

direction as a result of high stand shedding (Grammer and Ginsburg, 1992; Schlager et al., 1994; Jo et al., 2015). Grammer and Ginsburg (1992) documented the morphology and sedimentary characteristics of the foreslopes around the Tongue of the Ocean in the Bahamas in response to high amplitude, high frequency (5th order) fluctuations in sea level. The slope profile is characterized by a steep escarpment extending 50-60 m subsea that overlies a steeply-dipping (35-45º or greater) cemented slope. The base of the cemented slope is onlapped by a wedge of unconsolidated sediment with a 25-28º slope. This sediment wedge is analogous to upper Wolfcamp A slope angles along the Central Basin Platform found in this study because of the similar slope angles and sediment composition. Sediment gravity flows along the Tongue of the Ocean are driven by highstand shedding and are composed of fine grained skeletal and non-skeletal sands and carbonate mud derived from the platform interior (Grammer and Ginsburg, 1992). During sea level fall, deposits consisted of coarse skeletal sands, gravels, and boulders derived from fringing reefs. Schlager et al. (1994) later found that periods of sea level rise increase carbonate productivity and shed larger volumes of sediment off carbonate platforms in comparison to lowstands periods when rapid cementation stabilizes platform sediments.

Tectonic activity reached a maximum during the Wolfcampian and decreased in the early Leonardian (Adams, 1965; Silver and Todd, 1969; Hill, 1984; Schumaker, 1992). Because of this, seismic activity likely played a role in initiating sediment gravity flows into the basin. As demonstrated in Heezen and Ewing's study on the 1929 Grand Banks earthquake, the seismic initiation of turbidity currents, namely failure from seismically induced events does not take place in a single large event; rather in numerous slope failures with a duration of several hours (Heezen and Ewing, 1952; Normark and Piper 1991). A continuous transformation of debris flows to turbidity currents can occur during seismically induced gravity flow events which can maintain flow and slope failure over several hours (Normark and Piper, 1991). These initial debris flows likely result from reef collapse during seismic events due to horizontal acceleration or

overloading (Mullins, 1983; Normark and Piper 1991). Higher magnitude tectonic events are likely to shed more material compared to storm events and lower magnitude tectonic events (Normark and Piper, 1991). Examples of other turbidity currents and debris flows triggered by large earthquakes include deposits within the Southern Calabrian Ridge, Ioan Basin (Kastens, 1984), Holocene units in the Cascadia Channel (Griggs and Kulm, 1970), and the Contessa megabed in northern Italy (Ricci Lucchi and Valmori, 1980; Mutti et al., 1984). Carbonate sediment flows initiated by tectonic activity has also been reported on the Great Bahama Bank (Jo et al., 2014), Late Cretaceous deposits in the south central Pyreneese, Spain (Drzewiecki and Simo, 2002), and the Victorio Flexure area of the Sierra Diablo Mountains, West Texas (Playton and Kerans, 2006).

Slope failure may also be triggered by storm events such as hurricanes and seasonal cold fronts (Lee and Edwards, 1986; Normark and Piper, 1991), which can occur yearly to decadal (Hooke and Schlager, 1980; Mullins, 1983). Compared to tectonic activity, storm events are less likely to be a major source of turbidity currents (Normark and Piper, 1991).

In addition, antecedent topography of the basin floor and faulting, which can result in local bathymetric highs, can also contribute to sediment accumulation and development of large carbonate fan complexes (Goldstein et al., 2012). Jo et al. (2015) have recently illustrated the distribution, geometry, and morphology of margin failures and their associated carbonate mass transport complexes using multibeam bathymetry data and backscatter data. The platform edge along the southwestern GBB is continuous with the exception of four scalloped, convex margin segments (measuring 3-23 km in length along strike). Each convex margin segment is accompanied by downslope mass transport complexes on the lower slope and basin floor. Jo et al. (2015) concluded that margin collapse causes the platform edge to retreat and become steeper and shallower. In this case, margin collapse is most likely controlled by seismic shock, but other contributing factors are also possible including storm waves, over-steepening of the margin,

differential cementation, or the release of pore water pressure due to a fall in sea level. It should

be noted that these mechanisms are not well constrained (Jo et al., 2015). Collapse failures affect

the platform margin and uppermost slope while slides or slumps on the middle to lower slope (2-

8°) can transport sediment kilometers downslope (Figure 3) (Jo et al., 2015).
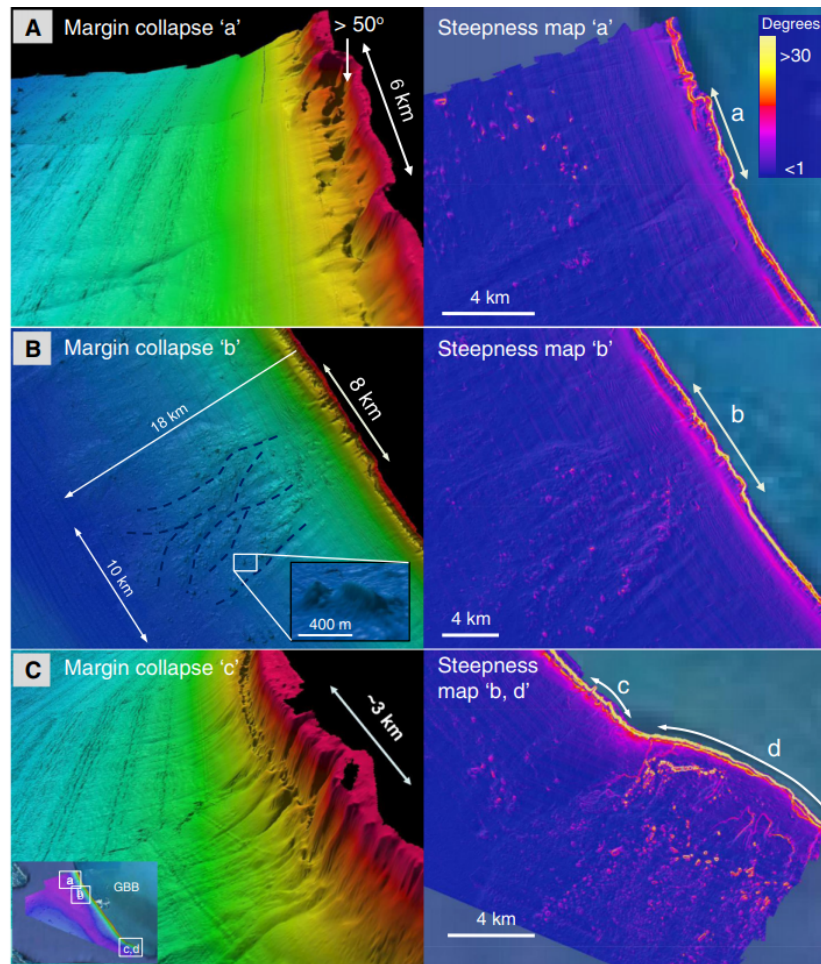
Figure 5: Images illustrating the margin collapse geometries, size, and distribution along the southwestern Great Bahama Bank margin. Left: Multibeam bathymetry of the margin collapse segments (a, b, c). Right: Shaded steepness maps derived from bathymetric map of the four margin collapse segments (a-d). A) 6 km length of margin scar; 50º upper slope angle; no lower slope failure. B) 6 km length of margin scar; 50º upper slope angle; no lower slope failure. C) 3 km length of margin scar; 30º upper slope angle; no lower slope failure. D: 23 km length of margin scar; >70º upper slope angle; lower slope failure (Jo et al., 2015). Upper slope angles range from 25-70º while middle to lower slope angles range from 2° to 8°, and decrease in the basinal direction. These lower upper slope to middle slope angles are similar to the late Wolfcampian to Leonardian slope angles of the Delaware Basin margin (~3-45°) (Hunt and Fitchen, 1999; Kerans and Tinker, 1999; Janson et al., 2007; Kenter, 1990).

2.9 Digital Image Analysis

Digital image analysis (DIA) is used to obtain quantitative parameters that define pore structure from both thin section and ion milled ESEM images for capturing the geometric character of pore structure (Weger et al., 2009). Pore parameters, such as perimeter over area (PoA) and dominant pore size (DOMsize), quantify the influence of pore types and structure on the petrophysical response in carbonate rocks (Weger et al., 2009). PoA is used as a proxy for pore complexity, and is the ratio of the sum of the perimeters of identified pores in an image over the sum of the areas of those pores. DOMsize is the pore size on the cumulative summation curve at 50% (Weger et al., 2009). Previous studies have analyzed the relationship between petrophysical properties and resistivity to pore size and structure in carbonate rocks with macroporosity (Eberli et al., 2003; Adams, 2005; Ahr et al., 2005; Weger et al., 2009). Norbisrath et al. (2015) found that samples with a tight pore network, defined by various small (small DOMsize) and complex pores (high PoA) with small pore throats, show better conductivity but lower permeability than samples with large pore network containing fewer large (large DOMsize) and simpler pores (low PoA) with large pore throats. Additional studies in carbonate mudrocks with predominantly micrometer to nanometer-scale pores have proven that petrophysical parameters are more complex when compared to conventional carbonate reservoirs (Norbisrath et al., 2015; Vanden Berg and Grammer, 2016; Bode et al., 2019) Therefore, this study, which is focused on "unconventional" types of mixed carbonate-siliciclastic reservoirs in the Permian Wolfcamp Formation, uses digital image analysis to quantify micropore and nanopore structure parameters, including PoA and DOMsize to evaluate if pore systems architecture can serve as a proxy for estimating petrophysical responses including porosity and permeability in these mudrock reservoirs.

CHAPTER III

METHODOLOGY

3.1 Data Set

This study utilized a multiscale approach to analyze facies types, gravity flow types and distributions, petrophysical responses, and pore systems architecture. Identification of facies, depositional features, and vertical stacking patterns on the sub-centimeter to meter bedding scale were digitized using EasyCore software. Both cores for this study cover the Wolfcamp A. Core 1 is located in Reeves County, Texas, and Core 2 is located in Ward County, Texas (Figure 6). Total lengths of these cores are 290 ft (88 meters) and 233 ft (71 meters), respectively. Forty-one thin sections in Core 1 and twenty-eight thin sections in Core 2 were included in the study (N-69). These thin sections were examined with optical microscopes under plane-polarized and cross-polarized light to bolster initial facies identification. Thin section examination allowed for the determination of rock texture, mineralogy, and grain size. Wireline log responses, including gamma-ray, deep resistivity, density porosity, neutron porosity, and sonic transit times from both vertical wells were tied to the core description and analyzed for stacking patterns in depositional facies, thickness, and porosity variations. Core measured porosity and permeability, X-Ray diffraction (XRD), and total organic carbon (TOC) weight percentage were measured by Weatherford and Core Laboratories to assess petrophysical properties and compositional differences in the identified facies. Additionally, seven 1.5-inch diameter core plugs from core 1

were utilized to sample thin slices (selected and created by Core Laboratories). These plugs were cut and polished at Oklahoma State University using a JEOL IB-19500CP cross section ion beam polisher to minimizes artifacts due to grain plucking often observed from manual polishing. The samples were then carbon coated in preparation for imaging. Micro- to nanoscale pores were imaged using a FEI Quanta 600F field emission environmental scanning electron microscope (ESEM). Ion-milled ESEM images were then uploaded into a digital image analysis software (LAS Application Suite with Image Analysis Module) to identify pore type and quantify the geometrical parameters of the pore system. These data were later tied to facies to examine the relationship between pore systems architecture and facies types.
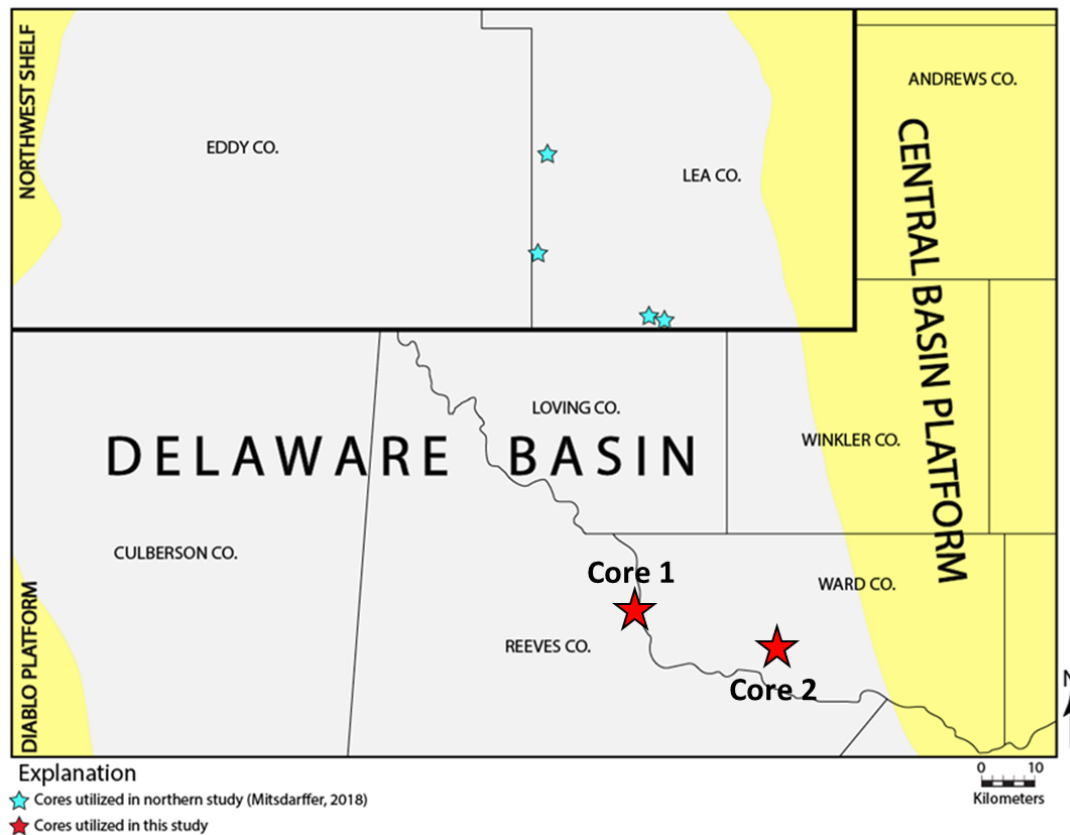
Figure 6: Base map of Core 1 (Reeves county) and Core 2 (Ward county) locations in the Delaware Basin depicted by the red stars. The Northwest Shelf and the Central Basin Platform are the major bounding features of the Delaware Basin.

3.2 Optical Microscopy and Facies Analysis

Standard (30 μm thick) thin sections were used in this study, all of which were impregnated with blue epoxy to indicate pore space and stained with Alizarin Red S to differentiate calcite from dolomite. Thin sections were prepared by Weatherford and Core Laboratories. A Leica DM 2700P optical microscope was used for petrographic analysis at Oklahoma State University. The carbonate facies were described using the Dunham (1962) classification scheme, and the siliciclastic facies were classified based on grain size and sedimentary structures. Thin section analysis combined with detailed core description were used to identify facies, bedding, textures, mineralogy, and gravity flow types.

3.3 Mineralogy

To understand the mineralogical composition of facies, XRD analysis was performed by Weatherford and Core Laboratories on selected intervals using a Siemens D-5000 diffractometer. Weatherford and Core Laboratories used JADE and TOPAS software for semiquantitative phase analysis. Ternary diagrams were created in this study plotting relative percentages of carbonate (calcite + dolomite), clay (illite, smectite, chlorite), and other (quartz and feldspar) content.

3.4 Wireline Log Analysis

Wireline logs (LAS files) from both wells were analyzed using IHS Petra Software. Scales were selected to appropriately represent log responses. Wolfcamp A formation tops in both wells were selected by tying core description depth to log depth with an estimated 2 ft depth correction based on log responses and recorded lithologies in the core description.

3.5 Environmental Scanning Electron Microscopy

Pore system architecture was analyzed on seven samples from Core 1 at Oklahoma State University. The samples were first polished with a broad-ion-beam (BIB) mill using the JEOL

IB-19500CP Cross Section Polisher argon ion mill. Milling time averaged 10 hours at 6.0kV. A high vacuum carbon coating was then applied to samples to prevent surface charging. A FEI Quanta 600F field emission scanning electron microscope was used for ESEM imaging. ESEM images were taken across a range of magnifications (from 2,000x to 100,000x) for each sample to capture the variation in pore type, geometry, and size on the micro- to nanopore scale. An accelerating voltage of 10-16 kV, a spot size of 5, and a working distance of approximately 10 mm were used to acquire most secondary electron images. Varying mineralogy was identified using backscattered secondary electron microscopy (BESEM) as well as energy-dispersive X-ray spectroscopy (EDS).

3.6 Pore Classification

Classification of microporosity was performed on the ESEM images and varied from micropores (62.5 µm to 1 µm) to nanopores (<1 µm) (Loucks et al. 2012). Choquette and Pray (1970) porosity classification and Vanden Berg and Grammer (2016) modification on pore classification in carbonate mudrocks were used as references to identify pore type. Terminology for pore type in this study mirrored the classification used by Vanden Berg and Grammer (2016) and Bode et al. (2019) (Figure 7). Pores between quartz-silt and clay dominated matrices were classified as interparticle, and pores between crystalline quartz and calcite cements were classified as intercrystalline. Dominant pore types were visually estimated as pore types yielding greater than 50% of the visible porosity in a sample (Weger et al., 2009).

Pore Size Classification
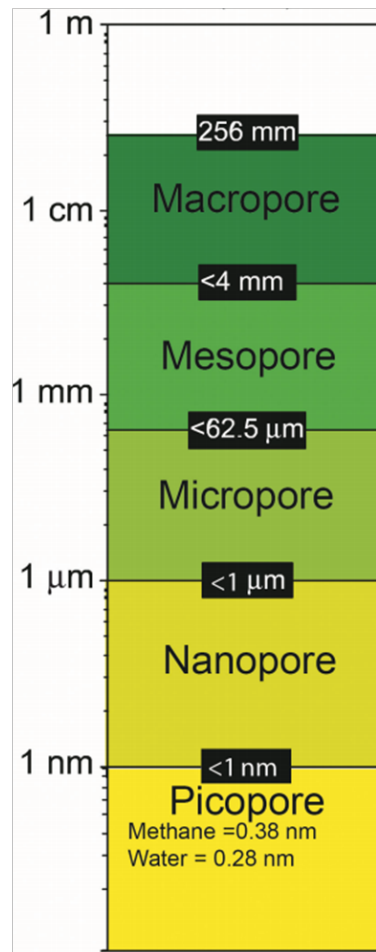
Figure 7: The pore size classification scheme used in this study as defined by Loucks et al. (2012) (Modified from Loucks et al., 2012, by Vanden Berg and Grammer, 2016).

3.7 Digital Image Analysis

ESEM images were uploaded into the Leica Application Suite with Image Analysis Module for digital image analysis. The software distinguishes pore space from surrounding rock using automated thresholding algorithms (Ehrlich et al., 1991; Anselmetti et al., 1998). Next, the software fills in pore space with color and calculates various pore size and shape parameters that are then exported into an Excel worksheet. Parameters selected in this study include pore shape, perimeter/area (PoA), dominant pore size (DOMsize), pore length, and pore count. Pore shape vs. PoA, PoA vs. pore length, and pore length vs. pore count were plotted in Excel to observe pore

size distribution across facies. Dominant pore size (DOMsize) was plotted against PoA to observe

the relation between pore size and pore complexity.

CHAPTER IV

RESULTS

4.1 Lithofacies

As illustrated in core and thin section, siliciclastic and carbonate rocks are the most pervasive lithologies in the study area (Figure 8). Core 1 is comprised of 67% carbonate lithologies and 33% siliciclastic lithologies (Figures 8 and 9). Core 2, in contrast, is mostly made up of siliciclastic lithologies (74%) and 26% carbonate lithologies (Figures 8 and 9). Thin section observations of both cores show grain size variation in siliciclastic facies ranging from clay to silt, and carbonate facies variation from carbonate mudstone, wackestone, mud-dominated packstone, and grain-dominated packstone. Subrounded to rounded detrital quartz, clays, feldspars are identified in core and thin section. Common biogenic skeletal grains averaging less than 1 mm to 2 cm in length include sponge spicules, radiolarians, silicified calcispheres, crinoids, fusulinids/forams, brachiopods, bryozoan, bivalves, and *Tubiphytes*. Intraclasts ranging from less than 1 mm to 10 cm in length (siliceous mudstone, shale, carbonate mudstone, wackestone, microbial/sponge, and mud dominated wackestone) are also identifiable in thin section and core. An additional component commonly found in both cores and thin sections are siliceous and calcareous cements. Lithofacies in this study include siliceous mudstone to detrital and biogenic siltstone (lithofacies 1 [L1]), argillaceous siliceous mudstone (lithofacies 2 [L2]), carbonate mudstone to wackestone (lithofacies 3 [L3]), and mud to grain dominated packstone (lithofacies 4 [L4]).
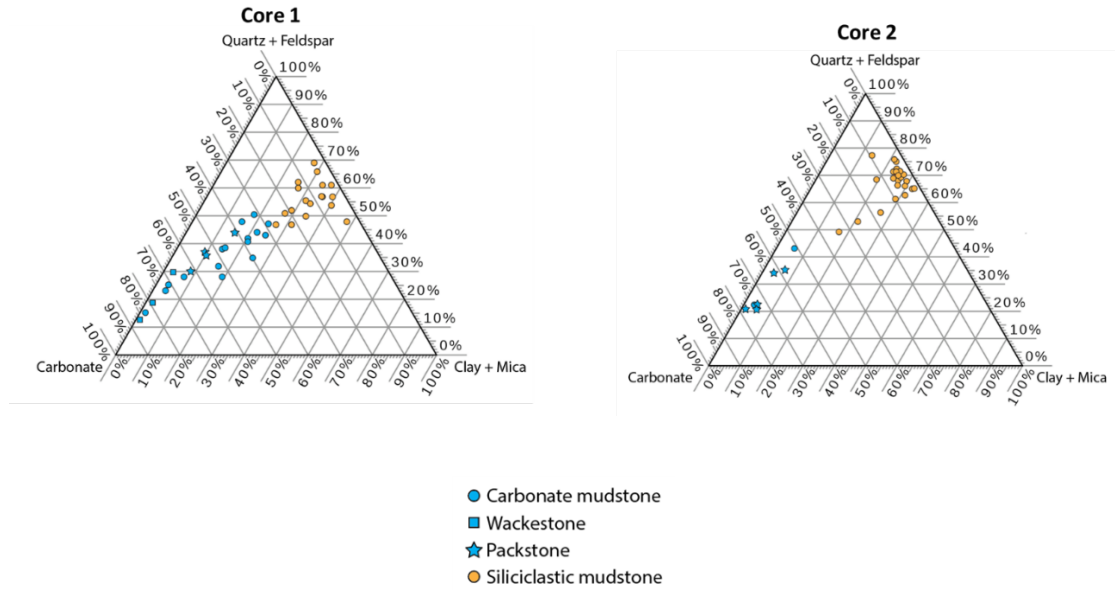
Figure 8: Ternary diagrams from Core 1 and Core 2 of mineralogy from XRD data. Carbonate percentages included calcite and dolomite. Clay percentages are plotted from total clay and mica. Quartz, potassium feldspar, and plagioclase were summed together for the third end member. Both cores contain mostly siliciclastic and carbonate mineralogy with <50% total clay.
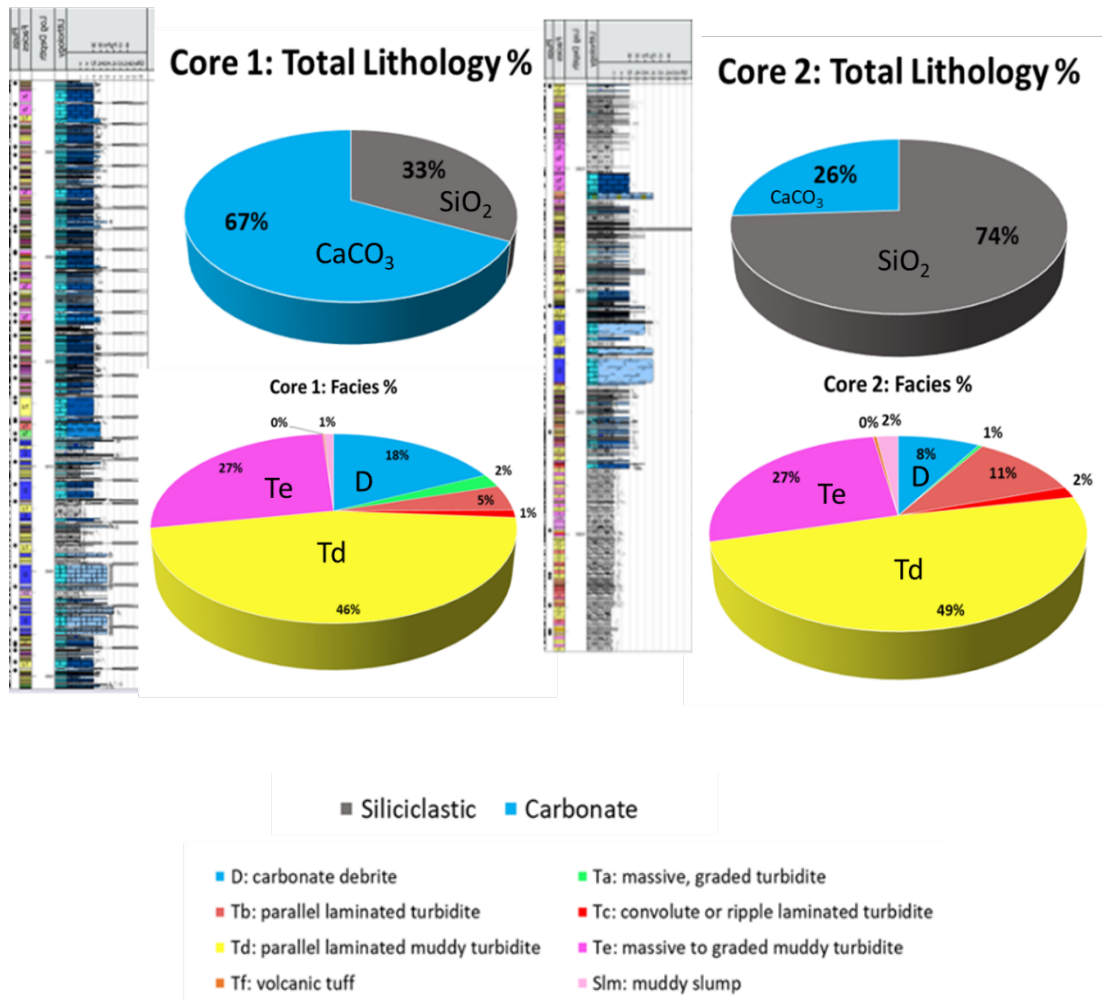
Figure 9: Core description overview, lithology percentages of siliciclastic vs carbonate rocks, and facies percentages from Core 1 and Core 2.

4.1.1 Siliceous Mudstone to Detrital and Biogenic Siltstone (Lithofacies 1, L1)

Quartz grains make up 35-75% of grains in L1. Relative volumes of grains for all lithofacies are based on XRD data and supported by thin section and core analysis. Detrital subrounded to angular silt-sized quartz grains are abundant along with siliceous sponge spicules, radiolaria, and silicified calcispheres (Figure 10). Amorphous siliceous cements are also present between the grains of L1 (Ulmer-Scholle et al., 2014). Detrital and authigenic clay content varies

between 20-30%. Illite is the most abundant clay type in L1. Calcite volumes make up 0-20% of

the rock. Small amounts of feldspars (5-10% plagioclase, 0-2% potassium feldspar) and pyrite (1-

7%) are also present. The average TOC weight percentage is 2.5.
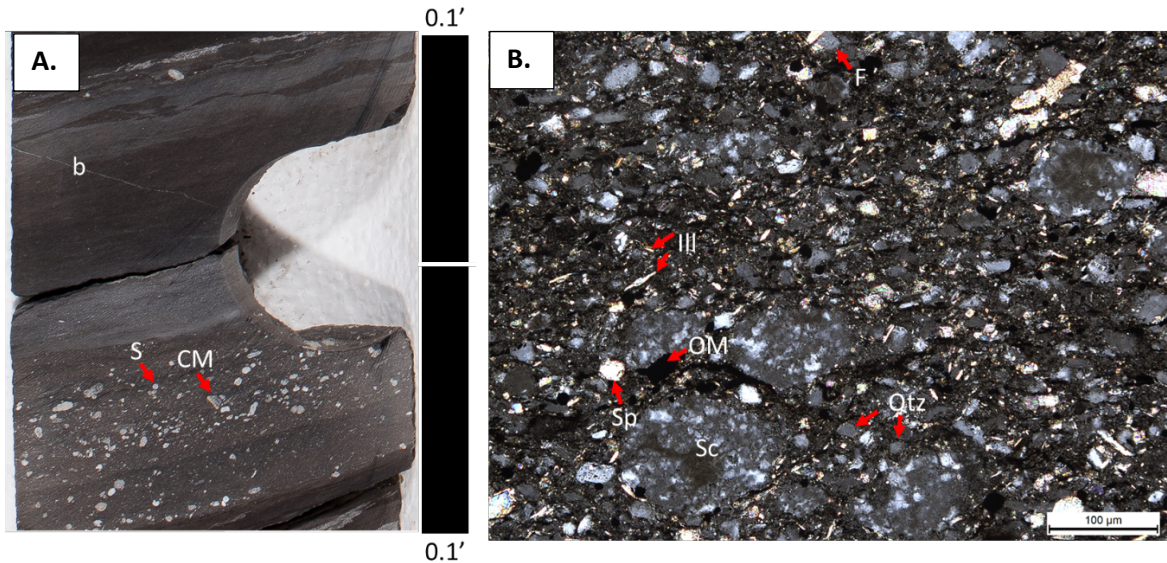
Figure 10: Core photo (A) of Lithofacies L1, siliceous mudstone to detrital and biogenic quartz siltstone. The core photograph displays an overall fining upwards from a siltstone to bioturbated (b) mudstone. carbonate mud intraclasts (CM) and siliceous intraclasts (S) are visible at the base of the core image (A). Image B shows the associated thin section photomicrograph in cross-polarized light taken from the core plug. Lithofacies L1 is dominated by biogenic and detrital quartz (Qtz), siliceous sponge spicules (Sp), and siliceous cements (Sc). Clays (predominantly illite (Ill)), feldspars (F), and dark organic material (OM) are present between grains.

4.1.2 Argillaceous Siliceous Mudstone (Lithofacies 2, L2)

Lithofacies L2 contains more clay minerals compared to L1. Detrital and authigenic clays

make up 20-50% of the minerals in L2 with illite and mica (20-40% bulk clays) being the most

abundant, followed by illite/smectite (4-10% bulk clays), and trace amounts of chlorite (1-2%

bulk clays). Quartz content in L2 is abundant and ranges from 36-56%. Detrital, subrounded to

angular silt-sized quartz grains are present and siliceous cements are present between grains

(Figure 11). Small amounts of pyrite (1-6%) and feldspars (5-10% plagioclase, 0-3% potassium

feldspar) are also present. Calcite is less abundant (0-15%) in L2 compared to L1. L2 contains the highest average TOC weight percentage of 2.7 compared to the other lithofacies.
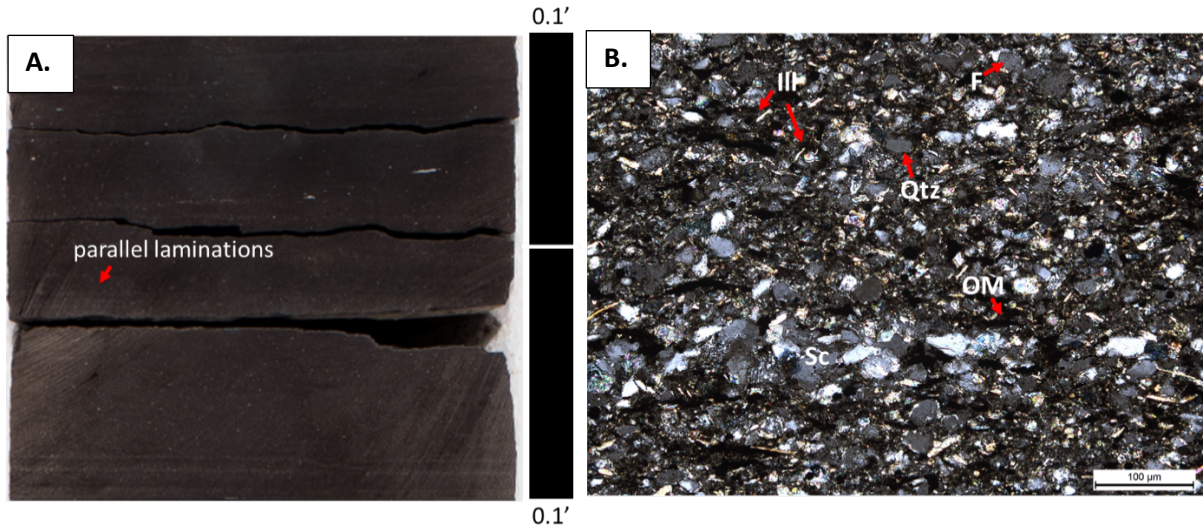
Figure 11: Core photo (A) of lithofacies L2, argillaceous siliceous mudstone. Parallel laminations are a common sedimentary structure found in L2. Image B is a thin section photomicrograph in cross-polarized light taken from a core plug. Lithofacies L2 is an argillaceous siliceous mudstone dominated by clays (predominantly illite (Ill)), detrital quartz (Qtz), and siliceous cements (Sc). Abundant illite and organic material (OM) are present between grains. Feldspars (F) are also present in L2, but in smaller amounts.

4.1.3 Carbonate Mudstone-Wackestone (Lithofacies 3, L3)

This lithofacies consist of calcite content of 20-82% and dolomite content of 1-14% dolomite. Calcite cements are abundant and fill in space between the grains (Figure 12). Fragments of fusulinids/forams, phylloid algae, crinoids, sponges, brachiopods, and bryozoan are the most common skeletal grains. Subrounded to angular carbonate intraclasts (mudstone, wackestone, microbial/sponge, and mud dominated packstone) and siliceous intraclasts ranging from less than 1mm to 6cm are also observed in core and thin section. Quartz content in the form of detrital and biogenic silica ranges from 10-42%. Illite and mica (1-18%) are the most abundant clay types in Lithofacies L3 with a total of 1-25% total clays. Minor amounts of feldspars (1-7%

plagioclase, 0-1% potassium feldspar) are found in L3 along with 1-3% pyrite. Average TOC values (1.2 weight %) are the lowest of all four lithofacies.
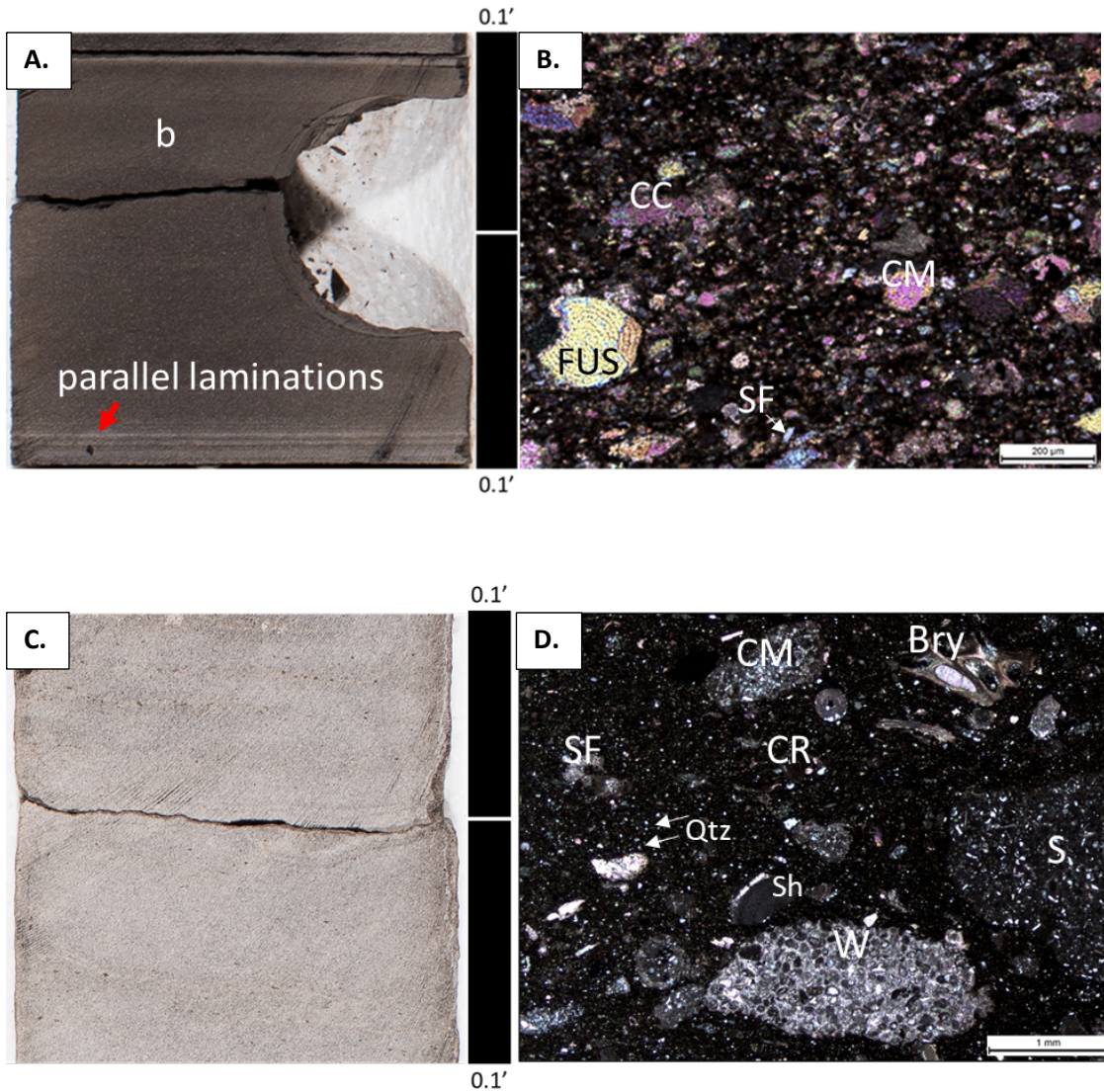
Figure 12: Core photos (A, C) and thin section photomicrographs in cross polarized light (B, D) of Lithofacies L3; carbonate mudstones to wackestones. Calcite is stained with Alizarin Red S. A) Core photograph of bioturbated carbonate mudstone with planar laminations and bioturbation. B) Micrograph of carbonate mudstone intraclasts (CM), calcite cement (CC), skeletal fragments (SF), and fusulinids (FUS) taken from core plug. C) Core photograph of massive intraclastic skeletal wackestone. D) Micrograph showing wackestone intraclasts (W), carbonate mudstone intraclasts (CM), siliceous intraclasts (S), shale intraclasts (Sh), skeletal fragments (SF), bryozoan (Bry), crinoids (Cr), and rounded detrital quartz clasts (Qtz) taken from core plug. Carbonate grains display high birefringence.

4.1.4 Mud to Grain Dominated Carbonate Packstone (Lithofacies 4, L4)

Carbonate packstones are dominated by 20-80% calcite and 2-14% dolomite. Grains are poorly sorted skeletal fragments (less than 1 to 10 cm in size) and subrounded to angular intraclasts (less than 1 mm to 10 cm in size) in varying compositions (mudstone, wackestone, microbial/sponge, mud dominated packstone, siliceous, and shale) (Figure 13). The majority of skeletal fragments include fusulinids/forams, phylloid algae, crinoids, *Tubiphytes*, sponges, brachiopods, bivalves, bryozoan. Sparite fills in spaces between the grains. Quartz and clay content range from 15-42% and 1-24%, respectively. Trace amounts of feldspars (1-3%) are found in L3 along with 1-3% pyrite. TOC values are low and average 2.3 weight percentage.
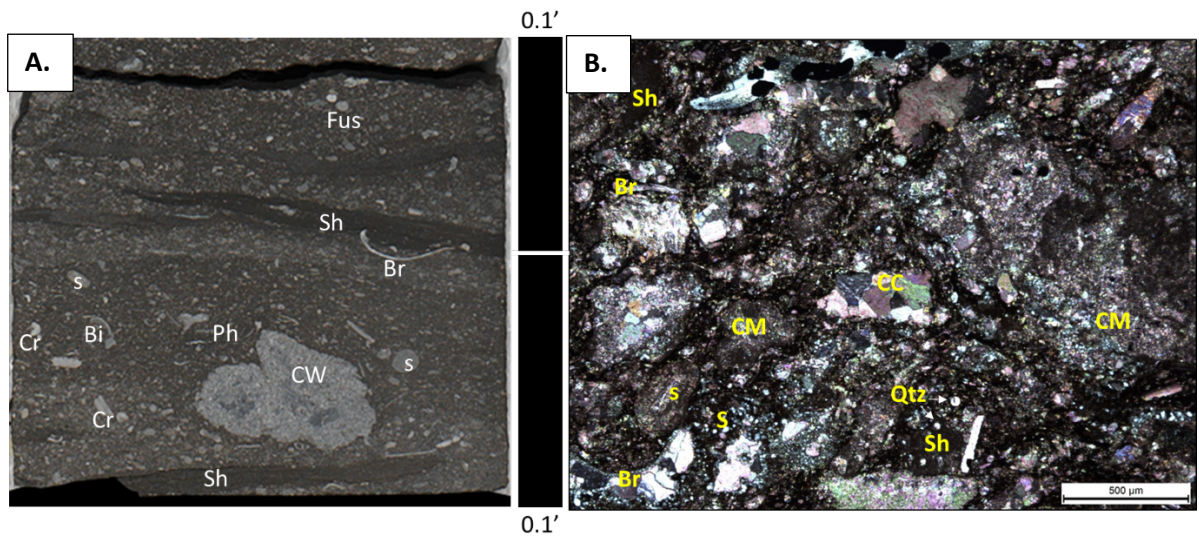
Figure 13: Core photo (A) and thin section photomicrograph in cross-polarized light (B) taken from core plug representing lithofacies L4. Calcite is stained with Alizarin Red S. Lithofacies L4 includes mud to grain dominated packstones. A) core photograph of a mud dominated intraclastic, skeletal packstone with massive, chaotic bedding. B). Photomicrograph of carbonate mudstone intraclasts (CM), carbonate wackestone intraclasts (CW), siliceous intraclasts (S), and argillaceous intraclasts (Sh). Abundant skeletal fragments including fusulinids (Fus), phylloid algae (Ph), crinoids (Cr), sponges (s), brachiopods (Br), and bivalves (Bi) are found within the matrix as well as calcite cement (CC), and rounded detrital quartz clasts (Qtz). Carbonate grains display high birefringence.

4.2 Depositional Facies

Seven depositional facies differing in composition, textures, and sedimentary structures were identified in both cores (Table 2). The depositional facies identified in this study are carbonate debrite (facies 1 [F1]) (Figure 14), (Ta) massive, graded turbidite (facies 2 [F2]) (Figure 14 and 15), (Tb) parallel laminated turbidite (facies 3 [F3]) (Figure 14 and 16), (Tc) convolute or ripple laminated turbidite (facies 4 [F4]) (Figure 14 and 17), parallel laminated muddy turbidite (facies 5 [F5]) (Figure 14 and 18), massive to graded muddy turbidite (facies 6 [F6]) (Figures 14 and 19), and mud-dominated slump (facies 7 [F7]) (Figure 20). Grain size across all facies ranges from clay-sized particles to up to 10 cm-long skeletal fragments and intraclasts. Massive and graded beds are common with minor localized ripple cross-laminations and convolute bedding. Coarser siltstone to packstone lithofacies generally display sharp erosive bases and overall fining upwards patterns (Figure 14). Bioturbation is locally preserved throughout all facies. In both cores, facies F5 is the most volumetrically significant and makes up 46% of Core 1 and 49% of Core 2 (Figures 14 and 16). F6 is the next most abundant facies, makes up 27% of all facies in both cores (Figures 14 and 16). Amounts of carbonate debrite facies found in both cores varies. Core 1 contains 18% F1 facies compared to 8% F1 facies observed in Core 2. Facies F2, F3, F4, and F7 are found in lesser amounts across Cores 1 and 2 (Figure 9).

4.2.1 Carbonate Debrite (Facies 1)

Carbonate debrite facies is dominated by mud to grain dominated packstones (L4) and is made up of mostly carbonate intraclasts, skeletal grains, and cements with argillaceous and siliceous mudstone to siltstone intraclasts (Figure 14). Common sedimentary structures within the facies include sharp upper and lower bedding contacts, protruding intraclasts of varying lithology

and shape, dewatering, shearing, and massive to deformed/chaotic bedding (Figure 14). Bedding

thickness observed in Facies 1 ranges from 0.1 (.03 m) to 12 ft (3.7 m).
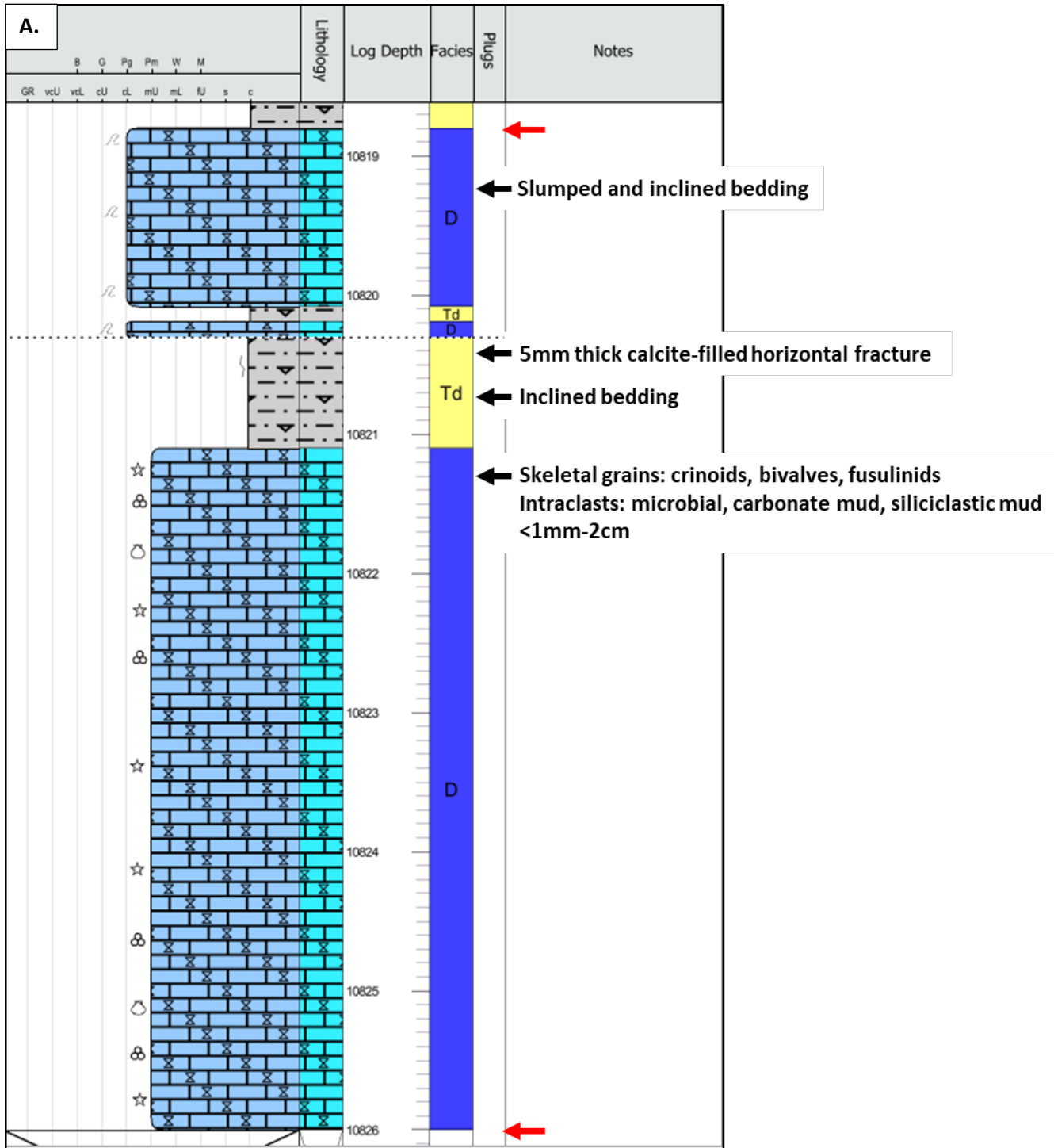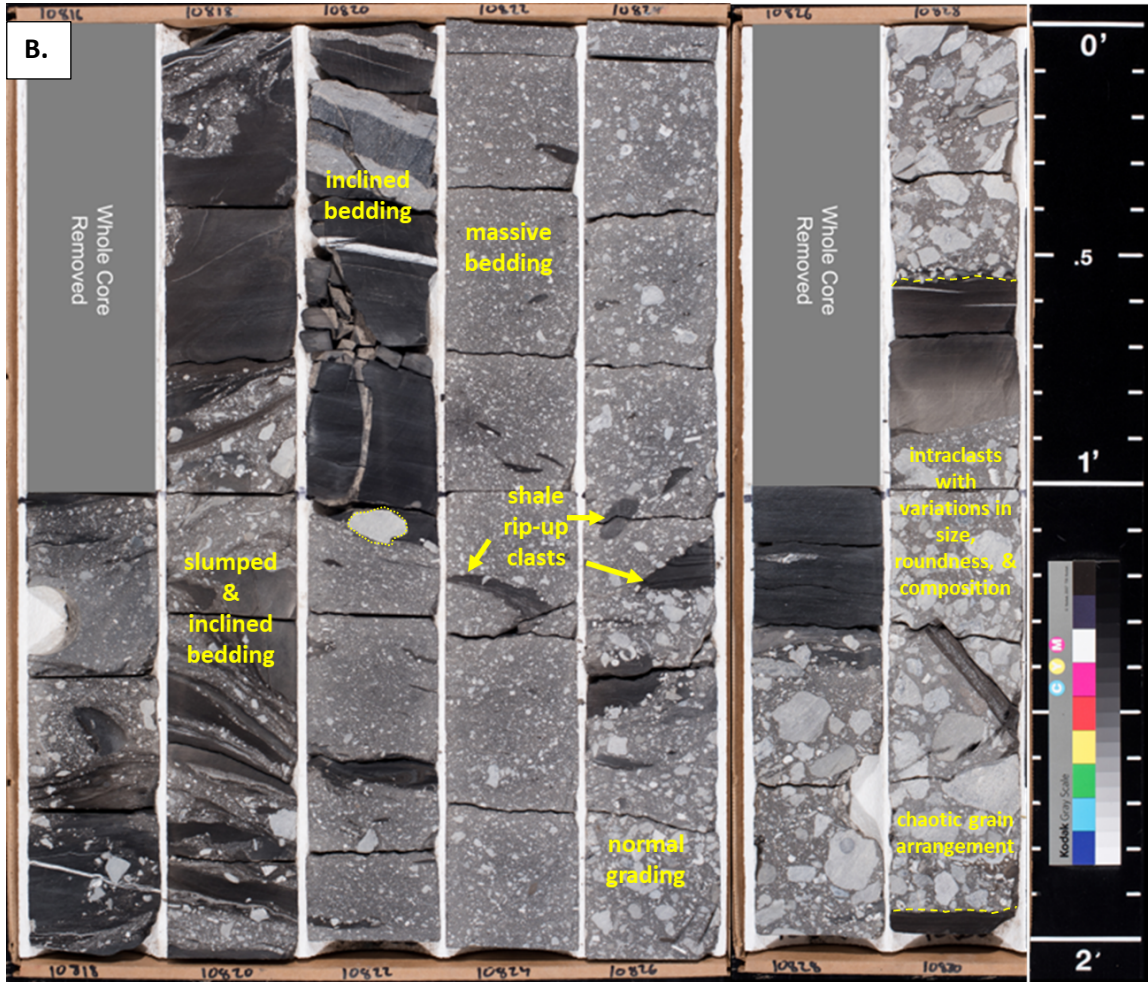
Figure 14: A) Core description of a carbonate debrite, facies F1 showing dominant carbonate lithology and minor siliciclastic lithology. Variations in bedding, skeletal grains, and intraclast size, shape, composition, and roundness are recorded on the cm scale. (B) Core box photo of facies F1 across a 14 ft interval. Core photograph shows inclined, normal, and massive grading within debris flow units. Grains within the debris flow units have chaotic fabrics and protruding intraclasts of varying lithology, size, and roundness. Sharp, erosive upper and basal contacts are also outlined in dashed lines.

4.2.2 (Ta-Te) Turbidite Facies (Facies 2-6)

Depositional facies 2-6 are all components of the Bouma sequence (Ta, Tb, Tc, Td, and Te). The full Bouma sequence is rarely preserved in core. Instead, partial sequences are repeatedly stacked on top of one another. Lithologies of these depositional facies include carbonate, siliciclastic, and argillaceous minerals (Figure 15). Bioturbation is preserved across all F2-F6 facies.
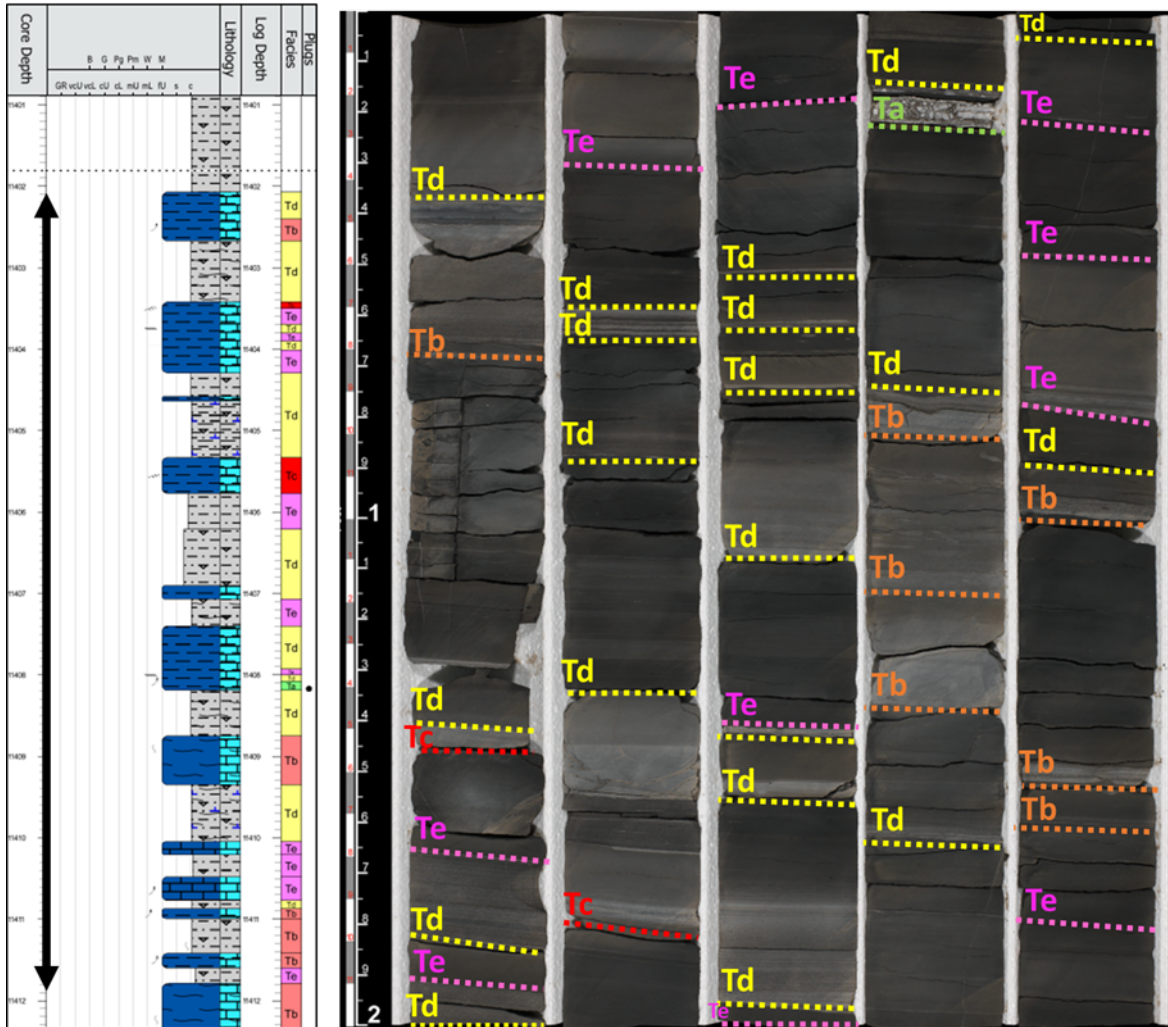
Figure 15: Core box photo and core description of stacked, incomplete, siliciclastic and carbonate turbidites (facies F2-F6) across a 10 ft interval. The bottoms of the turbidite facies are labeled Ta-Te and marked by the dashed lines. Abrupt facies changes are observed on the centimeter scale. Common bedding includes planar laminations in Tb and Td facies, ripple cross laminations in Tc facies, and Ta and Te facies are both massive graded.

Facies 2 (Ta) massive, graded turbidite contains detrital and biogenic quartz siltstones and wackestones to intraclastic, mud to grain dominated packstones (L1-L4). Common sedimentary structures observed in facies 2 include massive to slightly graded silt to gravel-sized loads, and deformed bedding (Figure 16).
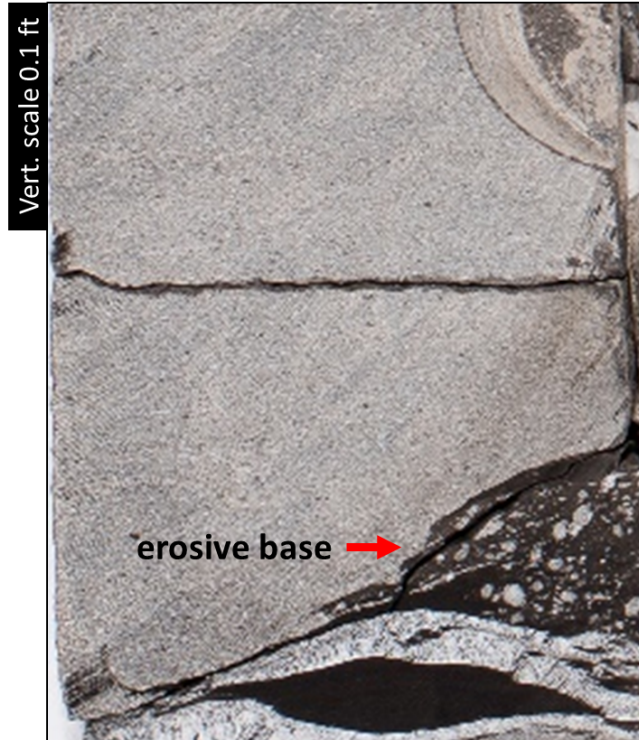
Figure 16: Close up core photograph of facies F2; massive, graded turbidite in a grain dominated intraclastic packstone. The erosive base of this facies is seen here by a sharp, sudden change in lithologies. Grains in this photograph display massive grading.

Facies 3 (Tb) parallel laminated turbidite contains the same lithologies as facies 2 (L1-L4) and is distinguished by planar laminations from upper flow regime conditions associated with higher energy (Bouma, 1964) (Figure 17). Deformed bedding is also observed in the facies.

Figure 17: Close up core photograph of facies F3; parallel laminated turbidite in a grain dominated intraclastic packstone. Sub-centimeter (<1 cm) planar bedding in this facies is a deposited under upper flow regime conditions with high enough energy to maintain the suspension of coarse grains (Bouma, 1964).

Facies 4 (Tc) convolute or ripple laminated turbidite is recognizable by ripple cross laminations. Lithologies range from argillaceous siliceous mudstone-detrital and biogenic quartz siltstone and wackestone (L1-L3) (Figure 18). Facies 2-4 are found in lesser volumes compared to the other facies (Figure 9).
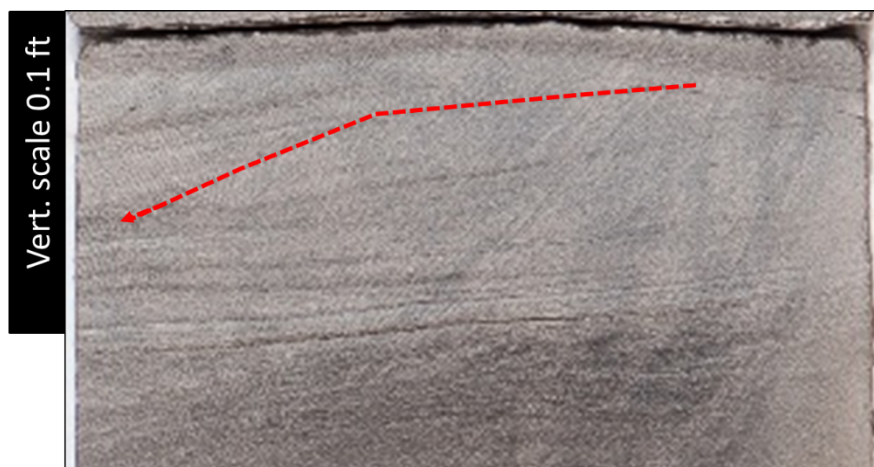
Figure 18: Close up core photograph of facies F4; ripple cross laminated turbidite in a carbonate mudstone to siltstone. Cross laminations are preserved on the <1 cm scale. The red dashed line shows the truncation of a foreset onto a lower erosive boundary.

Facies 5 (Td) parallel laminated muddy turbidite is the most common facies type in both cores (Figure 9). Lithologies include argillaceous siliceous mudstone-detrital and biogenic quartz siltstone; carbonate mudstone-wackestone (L1- L3). Facies 5 differs from facies 3 because F5 is dominated by mud to silt sized grains deposited by suspension settling (Figure 19) (Bouma, 1964).
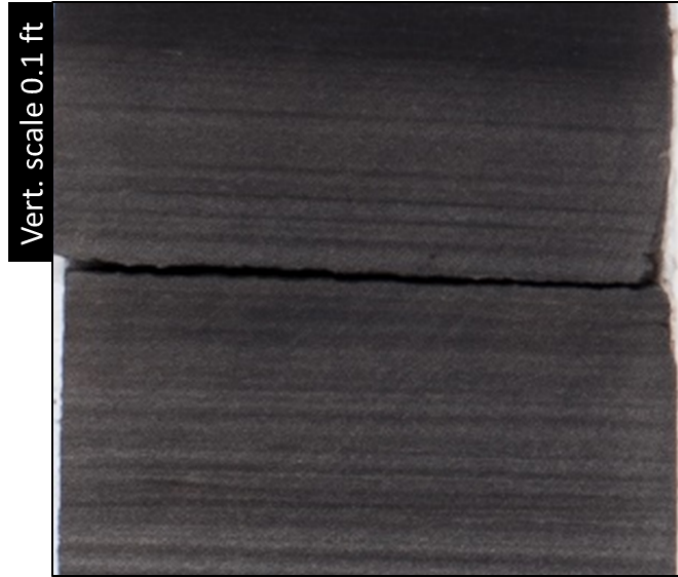
Figure 19: Close up core photograph of facies F5; parallel laminated muddy turbidite in a carbonate mudstone. The planar laminations in Facies F5 are formed from lower energy suspension settling of fine grains (mud to silt-sized grains) compared to the higher energy deposition and formation of planar laminations in facies F3 (Bouma, 1964).

Facies 6 (Te) massive to graded muddy turbidite is the second most abundant facies in both cores (Figure 9). Lithofacies L1-L3 are present across F6. It is dominated by mud-sized grains deposited by suspension settling (Bouma, 1964). F6 is very similar to F5 in lithology, but displays massive bedding rather than planar laminations (Figure 20).

Figure 20: Close up core photograph of facies F6; massive muddy turbidite in an argillaceous mudstone.

4.2.3 Muddy Slump (Facies 7)

Muddy slump facies are the least common facies found within both cores. This facies makes up 1% of facies found in Core 1 and 2% of facies in Core 2. Lithologies within facies 7 range from siliceous mudstones (L1), argillaceous mudstones (L2), and carbonate mudstones (L3). Upon closer examination, plastic deformation and convoluted bedding are visible within the dark mudstones (Figure 21).
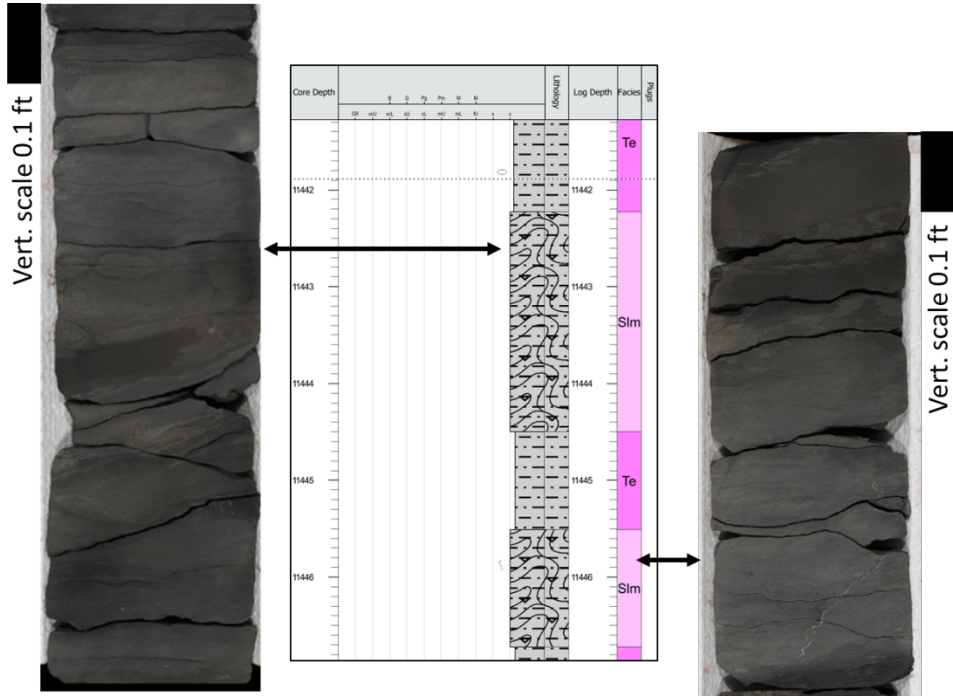
Figure 21: Core box photos and core description showing dark argillaceous and siliceous mudstone lithologies and plastic deformation within muddy slump facies 7 (SLM).

Facies Associations (Primary & Secondary Sedimentation Processes)	Lithofacies (Dunham (1962) classification)	Sedimentary Structures
Facies 1: Carbonate debrite	(**L4**): Mud dominated - grain dominated packstone	Sharp upper and lower bedding contacts, protruding intraclasts of varying lithology and shape, deformed bedding
Facies 2: (Ta) Massive, graded turbidite	(**L1-L4**): Detrital and biogenic quartz siltstone; Skeletal wackestone - grain dominated packstone	Massive to slightly graded, silt to gravel-sized basal loads, deformed bedding, shearing, dewatering
Facies 3: (Tb) Parallel laminated turbidite	(**L1, L4**): Detrital and biogenic quartz siltstone; skeletal wackestone - intraclastic, mud to grain dominated packstone	Parallel laminations, deformed bedding
Facies 4: (Tc) Convolute or ripple laminated turbidite	(**L1-L3**): Argillaceous siliceous mudstone - detrital and biogenic quartz siltstone; wackestone	Ripple cross laminations, deformed bedding
Facies 5: (Td) Parallel laminated muddy turbidite	(**L1-L3**): Argillaceous siliceous mudstone - detrital and biogenic quartz siltstone; Carbonate mudstone - wackestone	Parallel laminations, deformed bedding
Facies 6: (Te) Massive to graded muddy turbidite	(**L1-L3**): Argillaceous siliceous mudstone; Carbonate mudstone	Massive to slightly graded, mud to silt-sized basal loads
Facies 7: Muddy slump	(**L1-L3**): Argillaceous siliceous mudstone; carbonate mudstone	Deformed bedding, cm scale folds, plastic deformation

Table 2: Significant facies, lithofacies, and sedimentary structures found in Core 1 and Core 2.

4.3 Core to Well-Log Responses

Mineralogical volumes in the rocks affect well log responses. Several depositional facies in this study have overlapping mineralogy, which makes it difficult to distinguish in well log response. Additionally, centimeter-scale facies stacking patterns that are observed in core are too

high resolution for the logging tools to pick up, which typically have a maximum vertical resolution of no less than 0.5 feet (15 centimeters). Therefore, integrating detailed facies distribution in core to well log response is necessary to identify reservoir facies as well as facies that compartmentalize reservoirs.

Carbonate debrite facies (F1) are much easier to recognize in the well logs compared to the turbidite and slump facies. Bedding thicknesses of facies F1 varies from 0.1 ft (.03 m) to 12 ft (3.7 m). The higher calcite content within the mud to grain dominated packstone lithologies (L4) results in relatively lower gamma-ray values of 25-72 API units in Well 1 (Table 3) and 32-69 API units in Well 2 (Table 4) compared to the other turbidite and slump facies. Resistivity values in the carbonate debrites are relatively high compared to the other facies and have an average range of 20-50 Ωm in Well 1 (Table 3) and 45-200 Ωm in Well 2 (Table 4). Neutron porosity and density porosity nearly overlap indicating a limestone lithology, but there is still a slight separation that is due to the mixed lithologies of siliceous and argillaceous intraclasts in the calcite-rich rock (Figures 22 and 23). The average TOC weight percentage in the skeletal-rich carbonate debrite facies (F1) is 1-2 %. The relative spikes in TOC weight percentage can be correlated to several carbonate debrite deposits shown in Figures 22 and 23. Between the two wells, carbonate debrite facies have a lower average transit time (DT) (76 µs/f in Well 1 and 70 µs/f in Well 2) compared to the other facies, reflecting a more rigid carbonate lithology. Correlating well log data to core description is crucial in identifying carbonate debrites because of the variation in mineralogy in these deposits; specifically, the different siliceous, argillaceous, and carbonate intraclasts.

Facies 2, massive to graded turbidite (Ta), is similar to the carbonate debrites because it contains various carbonate, siliceous, and argillaceous intraclasts, but is less common (makes up 2% of facies in Well 1 and 1% of facies in Well2; Figure 9) and has a smaller average bedding thickness (<1cm to 1.5 m) (Figures 22 and 23). Only one bed containing facies F2 is thick enough

to register in the log signatures. This 1.5 m meter bed is located in Well 1 and is characterized by a low gamma ray response (25 API units), high resistivity (114 Ωm), overlapping average neutron and density porosity values of .02, and low average DT values (55 µs/f) (Table 3 and Figure 22). These log characteristics are also indicative of carbonate lithologies and could be misinterpreted as facies 1 without the use of core description.

Similar to facies 2, facies 3, parallel laminated turbidite (Tb) is not as abundant in both wells (makes up 5% of facies in Well 1 and 11% of facies in Well 2; Figure 9). One 10 ft-thick bed from Well 1 is recognizable in well log response (Figure 23). Average gamma ray values are moderate (76 API units) in comparison to the other facies, indicating a mixture of carbonate, siliciclastic, and argillaceous lithologies (Table 4). Average resistivity values in this facies are low (17 Ωm) and is likely due to the abundance of clay minerals (Table 4), which is also indicated by the separation between neutron and density porosity (Table 4, Figure 23). Higher neutron porosity responses can be attributed to higher volumes of clay-bound water and higher hydrogen index, which is what the neutron log records (Archie, 1942). Higher clay content in facies 3 is the driver for relatively high average DT values (82 µs/f) (Table 4).

Facies 4, ripple laminated turbidite (Tc), is very uncommon in both wells (makes up 1% of total facies in Well 1 and 2% of total facies in Well 2; Figure 9) and has an average bedding thickness of 0.03 m (0.1 ft). Thus, facies 4 is not recognizable in well log signatures.

Facies 5, parallel laminated muddy turbidite (Td), is the most abundant facies in both wells (makes up 46% of facies in Well 1 and 49% of facies in Well 2; Figure 9). This facies has a wide range in bedding thickness (<1 cm to 3 m). It is recognizable in well log curves by moderate to high average gamma-ray responses (80 API units in Well 1 and 100 API units in Well 2), low average resistivity (25 Ωm in Well 1 and 21 Ωm in Well 2), separation between the neutron and density porosity curves, and the highest average DT values (83 µs/f in Well 1 and 87 µs/f in Well

2) across all facies. Average TOC weight percentage of siliceous mudstones (L1) and argillaceous mudstones (L2) that dominate upper turbidite facies F5 and F6 is 2-3% (Figure 23).

The second most volumetrically abundant facies in both wells is facies 6, massive to graded muddy turbidite (Te) (makes up 27% of facies in Well 1 and Well2; Figure 9). Similar to facies 5, facies 6 also shows a wide range in bedding thickness (<1 cm to 1.5 m), but can amalgamate vertically up to 3 m in thickness as seen at the top of Well 2 (Figure 23). This facies has similar log responses as facies 5 because of the similarity in lithologies, being predominantly siliceous and argillaceous mudstones to siltstones with occasional carbonate mudstones to wackestones (Tables 2, 3 and 4). Average gamma ray values in facies 6 is also similar with facies 5, but can be slightly higher (85 API units in Well 1 and 110 API units in Well 2; Tables 3 and 4). Compared to facies 5, resistivity values in facies 6 are slightly higher (34 Ωm in Well 1 and 44 Ωm in Well 2), neutron and density porosity have the same magnitude of separation, and average DT is 76 µs/ft in Well 1 and 82 µs/ft in Well 2.

Facies 7, the slump facies, is also rarely observed in core (makes up 1% of facies in Well 1 and 2% of facies in Well 2). Average bedding thickness of facies 7 is 0.3-1.2 m (Figures 22 and 23). Gamma ray values are moderate to high (54 API units in Well 1 and 80 API units in Well 2), average resistivity in this facies is relatively low (17 Ωm in Well 1 and 27 Ωm in Well 2) compared to the other facies, and neutron and density porosity have the same magnitude of separation as facies 5 and 6, and average DT values are 71 µs/ft in Well 1 and 86 µs/ft in Well 2 (Tables 3 and 4).

4.4 Well-Log Facies Trends

The vertical heterogeneity that is observed from integrating core description and well log responses indicates a possibility for multiple stacked reservoirs. The presence of low porosity and permeability carbonate debrite intervals that can extend up to 3.7 meters in thickness contribute to

compartmentalization within the reservoir. Because of the overlapping log response among several facies types and the presence of relatively thin layers that are beneath the resolution of log data, an integrated approach that includes well logs and core analysis is crucial in identifying areas of stacked pay. Vertical facies stacking patterns are recognized in the well log responses. In Figures 22 and 23, red lines represent parasequence boundaries between significant facies changes that are recognized in the log responses. Each parasequence is labeled, starting at the base, as 1 to 5 in Well 1 and 1 to 3 in Well 2 (Figures 22 and 23).

Beginning at the bottom of Well 1, parasequence 1 is dominated by facies 5, parallel laminated muddy turbidite (Td) and composed of mixed siliceous, argillaceous, and carbonate mudstones. There is an overall increase in gamma ray moving upwards through the parasequence and an overall low resistivity which indicate a dominance of clay minerals and fining upwards depositional pattern. Parasequence 2 is marked by a relative low gamma ray response (25 API units) and high resistivity (80 Ωm). Gamma-ray signatures increase upwards, indicating a fining upwards parasequence. This parasequence is marked by four areas of carbonate debrite (facies 1) and lithologically mud dominate packstone facies. Between the carbonate debrites are facies 5, parallel laminated turbidites (Td), and facies 7, slump deposits that contain siliceous and argillaceous mudstone lithologies. The base of parasequence 3 is recognized by an abrupt increase in resistivity (175 Ωm) and low gamma ray 25 API units). Gamma ray response shows an overall increasing upward trend, and core analysis confirms an overall fining upwards in lithologies. This parasequence is dominated by turbidite (facies 2-6) deposition containing carbonate mudstones to wackestones at the base with less common interbedded siliceous and argillaceous mudstones towards the top of the parasequence. The centimeter-scale facies changes do not appear in the log responses, but there is an overall transition of facies 2, facies 3, facies 5, and facies 6 moving upwards through parasequence 3 that are recorded in the log signatures (Figure 22). Parasequence 4 is recognized as having an abrupt increase in resistivity (75 Ωm).

Facies 5, parallel laminated turbidites (Td) with predominantly carbonate mud lithologies, makes up the majority of this interval, but interbedded layers of siliceous and argillaceous mudstones are observed throughout the entire interval. Gamma ray and resistivity responses mirror the interbedded nature of the facies as the signatures lack a clear response and have an irregular trend (Figure 22). The uppermost parasequence in Well 1, parasequence 5, is recognized by its abrupt increase in resistivity (100 Ωm). This parasequence is dominated by facies 6, massive to graded muddy turbidite, containing mostly carbonate mudstones with the addition of siliceous and argillaceous interbedded mudstones. In the gamma ray response, an overall fining upwards trend is recorded (Figure 22).

Well 2 has three intervals with distinctive facies stacking patterns and depositional processes. Parasequence 1, located at the bottom of Well 2, is dominated by facies 5, parallel laminated muddy turbidites (Td). There is also one localized Tb and slump deposit within this interval. Lithologies are siliceous and argillaceous mudstones at the base with an increased amount of interbedded carbonate mudstones at the top of the interval. The gamma-ray curve has an irregular trend and lacks a clear response across the interbedded mudstones. Parasequence 2 can be recognized by a low gamma ray (32 API units) and high resistivity (100 Ωm). The base of this interval contains mostly facies 1, carbonate debrites, and there is an upwards transition to predominantly facies 5, parallel laminated muddy turbidites (Td), deposition. This facies shift and fining upwards in lithology is recorded in the gamma ray curve (32 API units to 100 API units). Parasequence 3 is recognizable by a localized decrease in gamma ray response (35 API units) and an increase in resistivity (90 Ωm). The bottom half is dominated by facies 6, and the upper half of parasequence 3 contains mostly facies 5. Lithologies transition from carbonate mudstone to siliceous and argillaceous mudstones at the top. This lithological transition is recorded in the gamma-ray curve (35 API units to 120 API units).
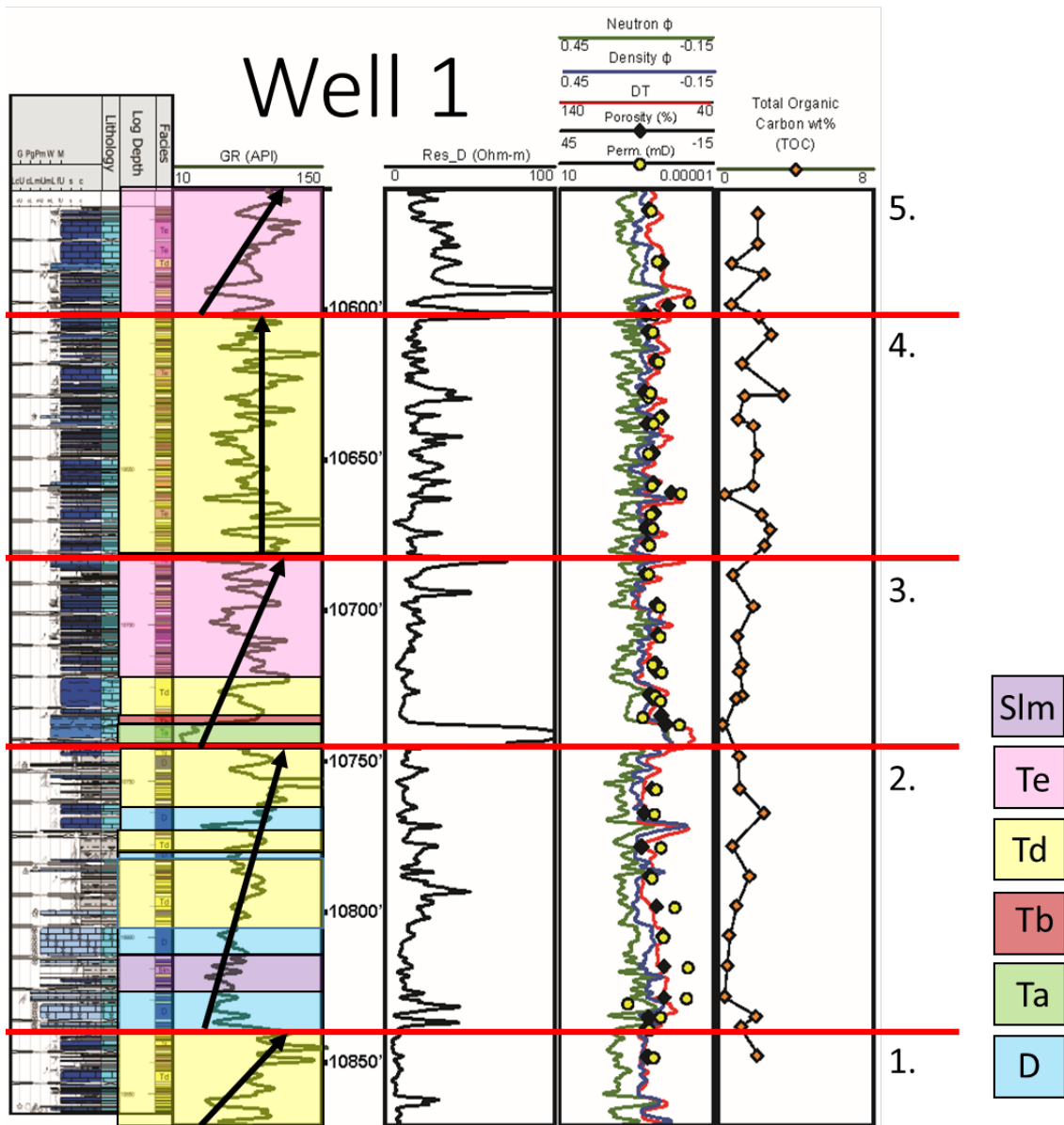
Figure 22: Gamma-ray, deep resistivity, neutron porosity, density porosity, transit time, and TOC weight % curves from Well 1 with plotted core measured porosity and permeability. Carbonate lithologies are blue and siliciclastic lithologies are grey in the core description. Major facies recognizable in log responses are highlighted and labeled. Three fining upwards parasequences and one aggradational parasequence (labeled 1-5) are observed in Well 1 and are divided by the red horizontal lines. Carbonate debrites (F1) are identifiable in well log as having relatively low average gamma-ray values of 25-72 API units, relatively high resistivity (20-50 Ωm), and less separation between the neutron and density porosity logs compared to facies dominated by siliceous and argillaceous lithologies.

Well 1 Facies	GR (API units)	RES (Ωm)	N ϕ	D ϕ	DT (μs/f)
F1: Debrite	25-72	20-50	.15	.08	76
F2: Ta	25	114	.02	.02	55
F3: Tb	-	-	-	-	-
F4: Tc	-	-	-	-	-
F5: Td	80	25	.19	.13	83
F6: Te	85	34	.17	.11	76
F7: Slm	54	17	.14	.08	71

Table 3: Average gamma ray, deep resistivity, neutron porosity, density porosity, and DT values calculated from each facies in Well 1. The vertical resolution of Tb and Tc facies is too small to identify in well logs.
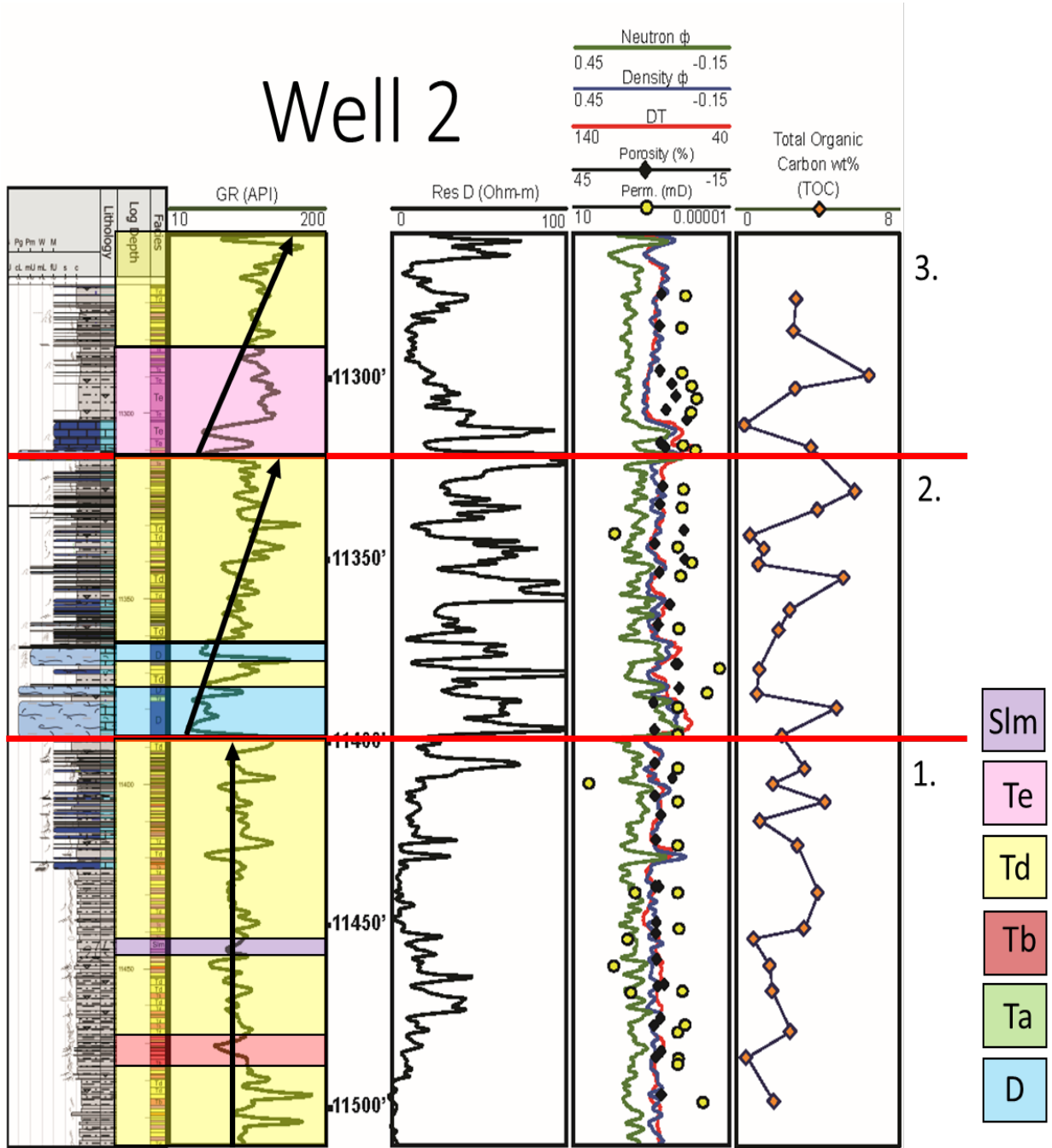
Figure 23: Gamma-ray, deep resistivity, neutron porosity, density porosity, transit time, and TOC weight % curves from Well 2 with plotted core measured porosity and permeability. Carbonate lithologies are blue and siliciclastic lithologies are grey in the core description. Major facies recognizable in log responses are highlighted and labeled. two fining upwards parasequences and one aggradational parasequence (labeled 1-3) are observed in Well 2 and are divided by the red horizontal lines. Carbonate debrites (F1) are identifiable in well log as having relatively low average gamma-ray values of 32-69 API units, relatively high resistivity (45-200 Ωm), and less separation between the neutron and density porosity logs compared to facies dominated by siliceous and argillaceous lithologies.

Well 2 Facies	GR (API units)	RES (Ωm)	N ϕ	D ϕ	DT (µs/f)
F1: Debrite	32-69	45-200	.09	.06	70
F2: Ta	-	-	-	-	-
F3: Tb	76	17	.19	.13	82
F4: Tc	-	-	-	-	-
F5: Td	100	21	.22	.13	87
F6: Te	110	44	.20	.14	82
F7: Slm	80	27	.22	.15	86

Table 4: Average gamma ray, deep resistivity, neutron porosity, density porosity, and DT values calculated from each facies in Well 2. The vertical resolution of Ta and Tc facies is too small to identify in well logs.

4.5 Pore Classification

Seven core plug samples from Well 1 were cut, milled, and prepared for ESEM imagery to classify the micro- to nanometer sized pores in the rock. Due to data limitation, samples were taken from facies 1, facies 5, and facies 6. Sample names are listed in Table 3. Observed pores in both cores were classified as micro- to nanopores due to their dominant sizes being in the micron to nanometer range. No open pores were identifiable in thin section. Pore types observed in this study include interparticle, intercrystalline, intraparticle, matrix, microfracture, and shrinkage (Figure 24). Each sample contains multiple pore types, and dominant pore types from each sampled facies were recorded. Some pores show clays, cements, and organic matter occluding pore throats.
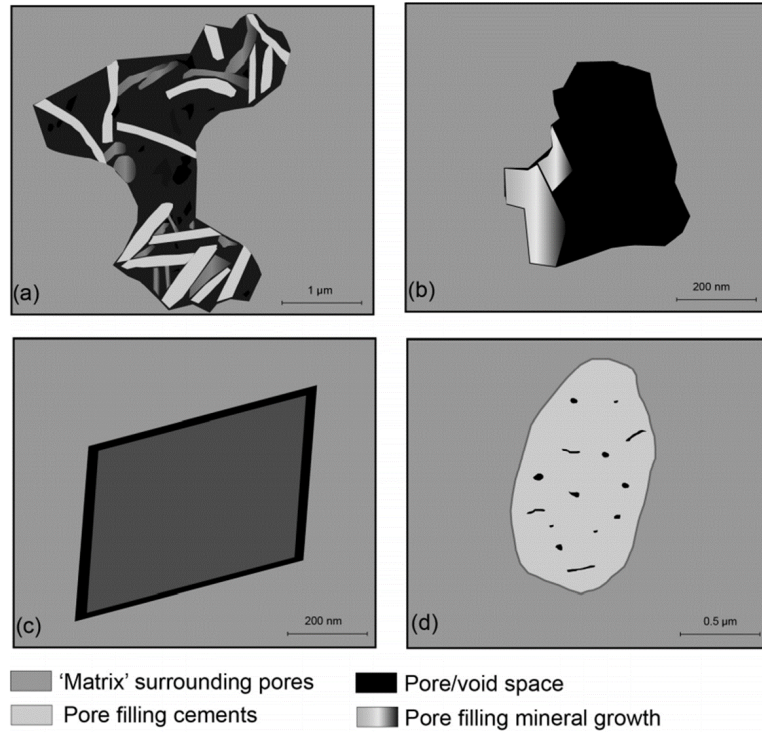
Figure 24: Pore type classification used in this study from Vanden Berg and Grammer (2016). Pore types include A) intercrystalline/interparticle, B) matrix/moldic, C) shrinkage, and D) intraparticle.

Figures 25 and 26 show an example from facies 1 (lithologically L4) comprised of intraclastic, skeletal mud dominated packstone. Pores in carbonate debrite facies (F1) are predominantly interparticle pores. The majority of interparticle pores exist in a muddy matrix, organic matter, clay cleavage-sheets, and skeletal fragments (Figure 25). Isolated intraparticle carbonate matrix pores are also found in F1 in minor amounts (Figure 26).

A.

Intraparticle clay cleavage-sheet pores

Interparticle clay-sheet pores

Interparticle pores occluded by micrite cements

Intercrystalline pores lined with cement

mag □	HV	spot	WD	det	HFW	2 µm
40 000 x	20.00 kV	3.0	10.0 mm	ETD	6.40 µm	

Figure 25: Interparticle porosity between clay-size intraclasts and matrix, interparticle and intraparticle clay-sheet pores, intercrystalline pores occluded and lined with carbonate cement in A. Image B shows interparticle and intraparticle organic matter (OM) pores, nanometer interparticle pores surrounding intraclasts, skeletal interparticle and intraparticle pores surrounding a fusulinid grain, and intercrystalline pores. ESEM images are taken within the carbonate debrite facies 1/lithofacies L4 intraclastic skeletal, mud dominated packstone (Sample Name: R 10807.65).

Figure 26: Isolated matrix pores and angular intercrystalline pores between calcite cement in a carbonate debrite (F1/L4). Intraclastic skeletal, mud dominated packstone (Sample name: R 10807.65)

The next four samples (R10728.6, R10583.8, R10672.35, R10627.6) were taken across facies 5, parallel laminated muddy turbidite. Interparticle pores are the dominant pore type in facies 5. Samples taken from the parallel laminated muddy turbidite facies had a mix of L1 to L3 lithologies. Similar to facies 1, interparticle pores exist between mud- to silt-sized matrices, organic matter, clay cleavage-sheets, and other skeletal fragments (Figures 27-31). Within L1-L2 samples, porosity is commonly preserved between amorphous silica cements (Figures 27, 29, 30,

31). Nanoscale cleavage sheet interparticle and intraparticle pores, and isolated intraparticle matrix pores are also commonly observed (Figures 27-29).
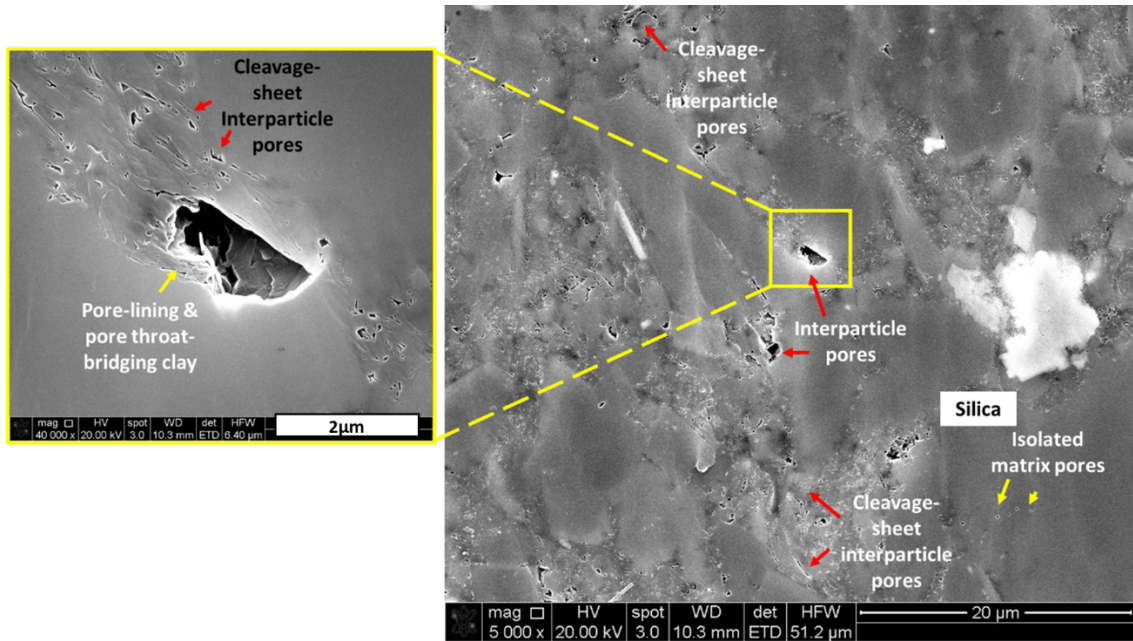
Figure 27: Cleavage-sheet interparticle pores in facies 5: (Td) parallel laminated muddy turbidite. This sample belongs to lithofacies 1, fining upwards siliceous mudstone with calcareous grains (Sample name: R 10728.6).
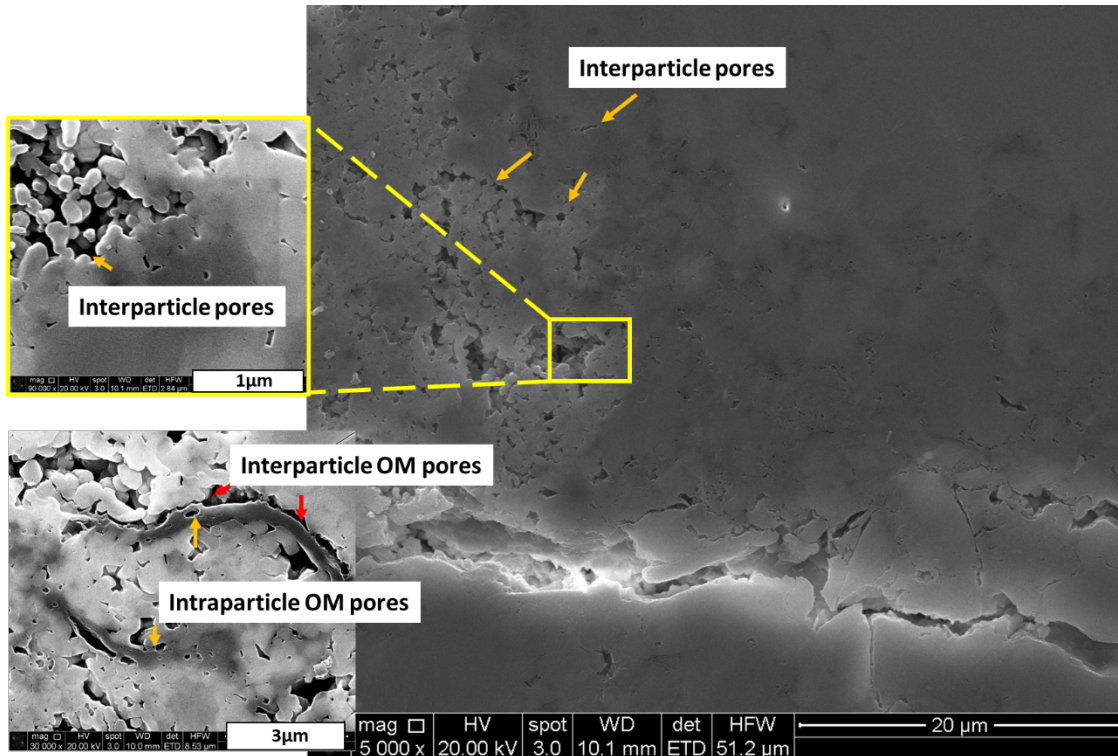
Figure 28: Interparticle, intraparticle, organic matter pores in facies 5: (Td) parallel laminated muddy turbidite. This sample lithologically belongs to L3: planar laminated, carbonate mudstone. The bottom left zoomed-in image displays interparticle OM pores and intraparticle OM taken from outside of the larger image (Sample Name: R 10583.8).
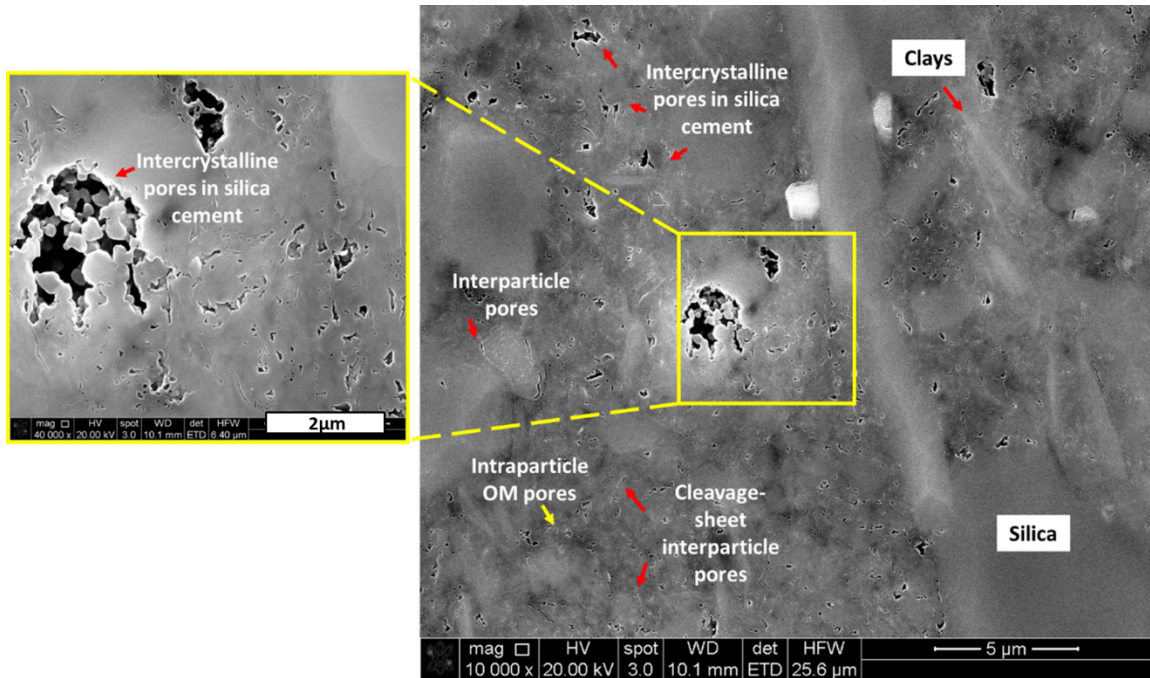
Figure 29: Interparticle/intercrystalline pores between silica cement, cleavage-sheets, and mud-sized grains. Facies 5: (Td) parallel laminated muddy turbidite. L2 bioturbated, fining upwards argillaceous siliceous mudstone. (Sample name: R 10672.35)

Lastly, two samples were collected from facies 6, massive to graded muddy turbidite. Samples from facies 6 (Lithologically L1 and L2) are dominated by interparticle/intercrystalline pore types (Figures 30 and 31). Pore space between amorphous silica cements (identified in thin section), clay cleavage-sheets, and organic material is prevalent. Intraparticle organic pores, microfracture pores, and isolated matrix pores are less commonly observed (Figures 30 and 31).
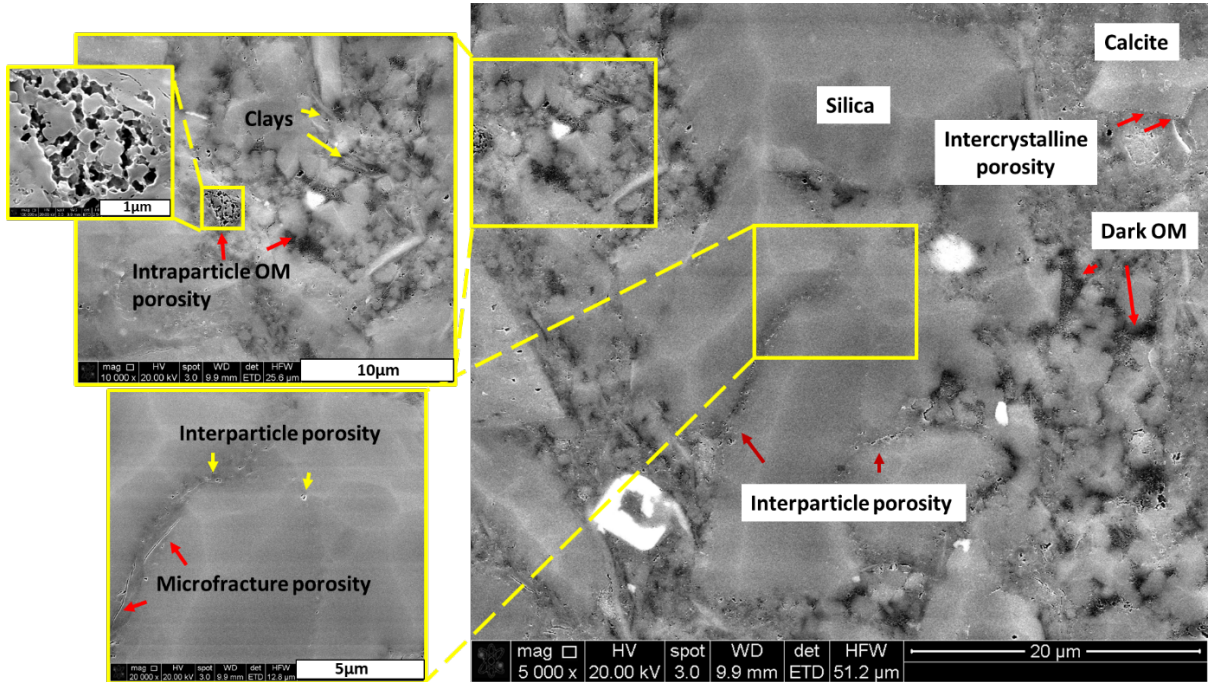
Figure 30: Interparticle/intercrystalline, microfracture, intraparticle OM pores. Facies 6: (Te) Massive to graded muddy turbidite. L2 planar laminated argillaceous siliceous mudstone with carbonate grains (Sample Name: R 10627.6)
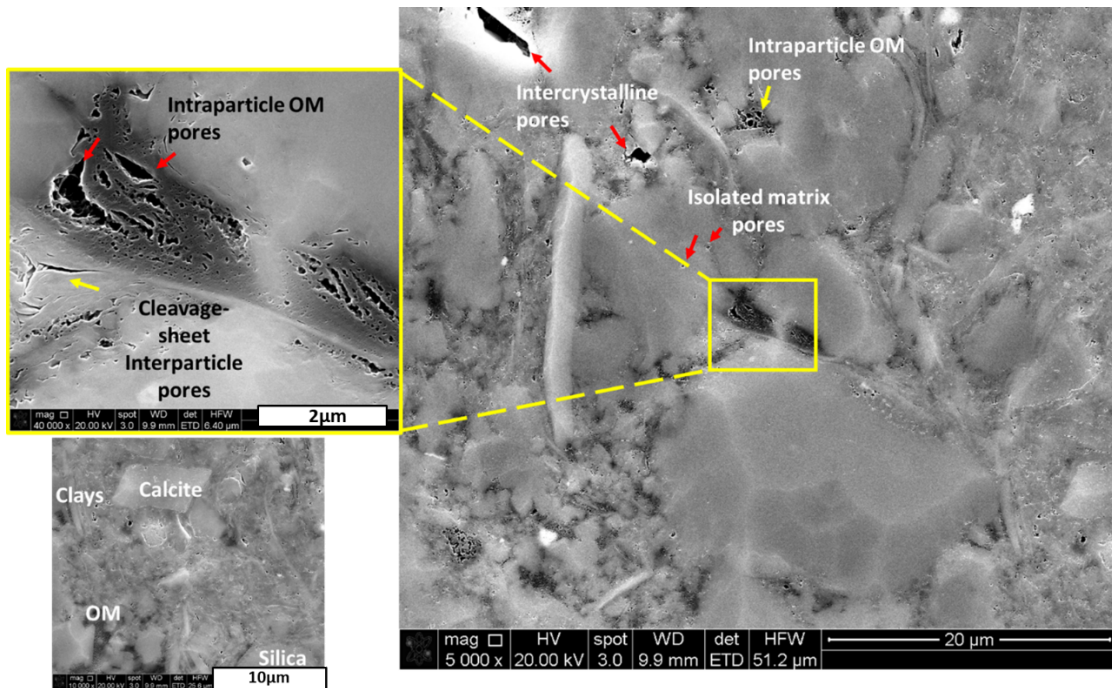
Figure 31: Intraparticle OM pores, cleavage-sheet interparticle pores, intercrystalline pores, isolated matrix pores. Facies 6: (Te) Massive to graded muddy turbidite. L2 planar laminated argillaceous siliceous mudstone with carbonate grains (Sample Name: R 10627.6)

4.6 Digital Image Analysis

The goal of digital image analysis is to quantify pore geometries to recognize any trends or relationships between pore architecture and permeability. Selected pores in thin section and ESEM are recognized by the digital image analysis software via color segmentation of dark and light gray hues. Pore perimeter, pore area, pore length, and pore count are measured by the software. By cross-plotting these attributes and comparing them to petrophysical properties such as permeability for different pore types and facies, pore architecture can be related to permeability. Carbonate debrite facies 1 had the lowest DOMsize (.22 µm) compared to F5 and F6. DOMsize in facies 5 and 6 were similar and range from .26-.32 µm. Samples with lower DOMsize have low measured porosity values (table 5).

Average PoA in facies 1 was 23.18 µm^{-1}. PoA ranged from 9.80-25.28 in facies 5 µm^{-1}, and .28-.30 in facies 6 µm^{-1}. Generally, lithofacies with the highest carbonate content (L3, L4) had the highest PoA values, indicating complex pore structure. Lowest overall PoA values were consistently recorded in lithofacies L1 and L2 (table 5).

Sample ID	Texture/Lithofacies (Dunham (1962))	Facies Associations (Primary & Secondary)	XRD (%) Clays	Carb.	Other	Porosity, Volume %	Permeability, millidarcies	Dominant Pore Type, SEM	DOM Size (µm)	PoA (µm⁻¹)
R10807.65	Intraclastic, skeletal, mud dominated packstone	Facies 1: Carbonate debrite	9	53	38	4.5	0.00083	Interparticle pores, OM interparticle pores	0.22	23.18
R10583.80	Planar laminated, carbonate mudstone	Facies 5: (Td) Parallel laminated muddy turbidite	7	65	28	5.0	0.00138	Interparticle pores	0.31	9.80
R10635.75	Planar laminated carbonate mudstone-siltstone	Facies 5: (Td) Parallel laminated muddy turbidite	4	73	23	5.0	0.00127	Interparticle pores	0.26	25.28
R10672.35	Bioturbated, fining upwards argillaceous siliceous mudstone	Facies 5: (Te) Parallel laminated muddy turbidite	48	4	48	11.0	0.00209	Interparticle pores, cleavage-sheet interparticle pores	0.32	18.68
R10728.60	Bioturbated detrital and biogenic quartz siltstone/carbonate mudstone	Facies 5: (Td) Parallel laminated muddy turbidite	26	27	47	8.4	0.0012	Interparticle pores	0.27	18.56
R10601.60	Fining upwards siliceous mudstone with calcareous grains	Facies 6: (Te) Massive to graded muddy turbidite	29	19	52	11.0	0.00174	Intercrystalline/interparticle pores	0.30	19.17
R10627.60	Planar laminated argillaceous siliceous mudstone/carbonate mudstone	Facies 6: (Te) Massive to graded muddy turbidite	27	22	51	11.5	0.00252	Intercrystalline/interparticle pores	0.28	15.73

Table 5: Summary of ion-milled DIA from core plugs. Lithofacies, depositional facies, XRD mineralogy percentages, lab measured porosity and permeability, dominant pore type, DOMsize, and PoA values.

CHAPTER V

DISCUSSION

5.1 Deposition and Architecture of Sediment Gravity Flows

The complex deposition and heterogeneity of gravity flow distribution and lithology make it difficult to predict reservoir geometries in the subsurface. Understanding the timing and deposition of gravity flow deposits gives insight on predicting where reservoir facies are located and how reservoirs are compartmentalized. Amalgamation of turbidites, carbonate debris flows, and slump facies in core along with rapid facies changes on the sub-centimeter scale are evidence that multiple gravity flows are responsible for the sedimentation of the Wolfcamp A formation (Asmus and Grammer 2013). Compensational stacking patterns of facies, formed by the tendency of gravity flow sediments to fill in topographic lows, observed in core, suggest that rather than a single slope failure event, multiple gravitational slope failures and bottom-water currents that retriggered unstable slope sediments were continuously deposited and amalgamated across the slope to Basin environments. These continuous processes result in the amalgamation of reservoir facies. Abrupt changes in facies and erosive bases observed in core, especially at the base of debrite and lower turbidite facies, are evidence of erosion associated with deposition and channelization of gravity flows. Sediment focusing and multiple margin reentrants that cross-cut and intermingle one another contribute to the lateral heterogeneous nature of facies distribution in this study. Figure 32 schematically illustrates various geometries associated with gravity flow deposition across the platform top, margin, slope, and basinal environments. These include

channelized fans, basin floor fans, localized margin collapses, strike extensive aprons, and drift

contourites (Walker, 1978; Janson et al., 2012; Playton et al., 2012). Further adding to

depositional complexity, sudden vertical facies changes traced in core also suggests gravity flows

traveling down slope initiated other gravity flows and remobilizing sediment (Eberli 1991;

Mullins et al. 1984; Shanmugam and Moiola 1984; Handford and Loucks 1993; Schlager et al.

1994; Playton and Kerans, 2002; and Houghton et al., 2003). All of these depositional factors

make it difficult to predict reservoir geometries in the subsurface.
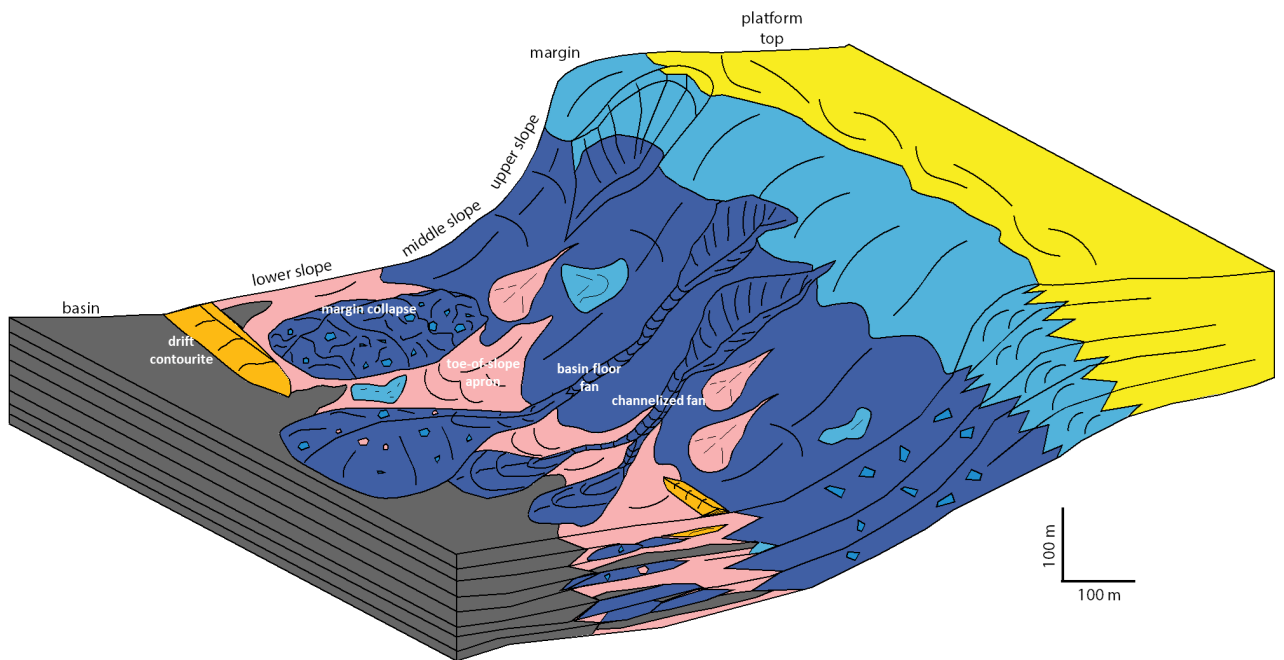
Figure 32: Schematic block diagram illustrating the multiple gravity flow geometries across the platform top, margin, slope, and basin. Margin collapse, basin floor fans, channelized fans, toe of slope aprons, and drift contourites are all shown to have different architects and distributions. Strike-extensive aprons, isolated debris beds related to local slope failure, and basinal channel-lobe complexes carry mud, grain, and debris down slope. Modified from Janson et al. (2012).

Texture, grain size, sedimentary structures, and bedding help to distinguish spatial

architecture and location within a gravity flow deposit (Walker, 1978; Janson et al., 2012; Playton

et al., 2012). Identifying reservoir facies and understanding the spatial architecture of the

associated gravity flow responsible for deposition can refine reservoir modeling and optimize

recovery. Facies 1 contains mud to grain dominated packstones which indicate gravity flow

60

architecture is likely distributed in the form of individual debris flows, grain dominated strike-extensive lower slope aprons, or proximal positions in a basinal grain-dominated channel-fan complexes (Figure 33). The low porosity and permeability of these carbonate debrites act as hydrocarbon flow barriers and compartmentalize the reservoir. Throughout most of the cores, mud to silt-sized grains and wackestone textures dominate deposition (L1-L3). Clay to silt-sized grains dominate deposition in distal portions of basinal channel lobes (Walker, 1978). The presence of L1-L3 lithologies may indicated periods of sedimentation occurring in distal portions of basin channel lobes. The clay to silt-sized grains (L1-L3) in combination with localized burrowing, planar laminations, and cross laminations may also suggest a strike-extensive lower slope apron depositional architecture (Playton et al., 2012 and Janson et al., 2012). These amalgamated turbidite deposits, specifically facies 5, parallel laminated muddy turbidite (Td), and facies 6, massive to graded muddy turbidite (Te), with L1 and L2 lithologies, provide the best reservoir rock (highest porosity, highest permeability, bedding thickness up to 3m) for hydrocarbon recovery. Integrating core analysis to well log analysis and lab measured petrophysical data is necessary to identify these stacked reservoir facies, which ultimately leads to increased hydrocarbon recovery.

Characteristics	Debris Deposits	Grain Dominated Deposits	Mud Dominated Deposits
Texture & Grain Size	megabreccia & blocks; cobbles & boulders	packstone, grainstone, & rudstone; sand & pebbles	mudstone, siltstone, & wackestone; clay & silt
Structures & Bedding	unorganized; thick lenticular beds	graded & stratified; medium tabular beds	burrowed or rippled & finely laminated; thin bedded
Spatial Architecture			
Source CO3 Factory	lithified marginal or upper slope	high energy platform-top & margin	low energy platform interior or water column
Resedimentation Process	brittle failure & gravitational collapse	offbank shedding from currents	offbank shedding from currents or pelagic fallout

Spatial Architecture diagram labels (left to right, top to bottom): platform top; lithified margin; foreslope; toe-of-slope; basin; isolated embayments; multiple reentrants; numerous scallops/scars; current & sediment focusing; strike extensive aprons; foreslope megabreccia horizon; debris-dominated slope apron; grain-dominated slope apron; gullied (bypass) upper slope & lower slope apron; isolated basinal megabreccia; basinal grain-dominated channel-fan complexes.

Legend:
- debris deposits
- grain-dominated deposits
- mud dominated deposits

Figure 33: Characteristics and architecture of debris, mud, and grain deposits. Modified from Playton et al. (2012) and Janson et al. (2012).

5.2 Facies and Lithologies Tied to Sediment Distribution

Facies and lithology variability between the two cores have critical implications on sediment distribution. Core 1 and Core 2 contain the same facies types, but the volume of carbonate and siliciclastic materials varies. Although Core 2 is more proximal to the Central Basin Platform (carbonate factory), it contains 26% carbonate material compared to 67%

carbonate material in Well 1. Therefore, it is possible that Well 1 is located more proximal to a reentrant channel than Well 2. Topographic lows that exist in antecedent topography or preexisting faults located in the dip direction of the platform margin can also funnel sediments downslope in the form of large carbonate fan complexes (Goldstein et al., 2012). Localized faulting near Well 1 and Well 2 likely funneled sediments around upthrown fault blocks (Kvale et al., 2019). This is likely another reason why greater amounts of carbonate material are located in Well 1 than Well 2. Areas located proximally to carbonate channel fans are likely to have rocks with poor reservoir quality (low porosity and permeability) and greater reservoir compartmentalization.

The large volumes of sand, silt, and clay were transported from the ancestral Rockies and neighboring uplifts (from present day northeast) and deposited into the Delaware Basin (Fischer, A. G., and Sarnthein, M., 1988). During time of deposition, the area was located in the trade-wind belt, which explains the volumetrically significant amount of siliciclastic input interspersed with carbonate materials (Figure 34). Siliciclastic input dominated periods of lowstand sea level (Fischer, A. G., and Sarnthein, M., 1988). The abundance of siliceous and argillaceous muddy turbidite facies 5 and 6 (parasequence 1, top of parasequence 3, parasequence 4 and parasequence 5 in Well 1 and parasequences 1 and 3 in Well 2) in both wells represents deposition in distal portions of basin channel lobes, which in this study creates the best reservoir rock. A lack of carbonate debrites compared to turbidite facies, despite proximity to the carbonate factory in Well 2, is likely due to carbonate sediment funneling and accumulating in larger concentrations near but not central to the two cored intervals in this study.
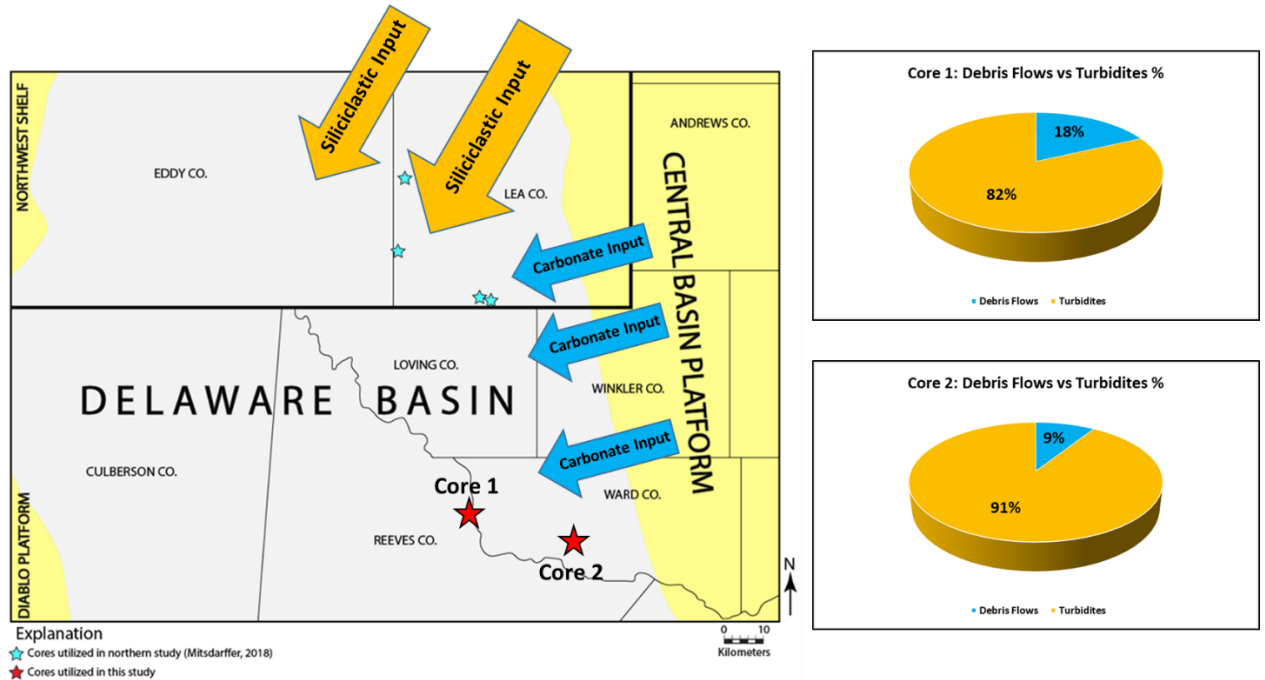
Figure 34: Base map showing cored wells 1 and 2 indicated by the red stars. Siliciclastic input was sourced from the northeast in the same direction as paleo trade winds. Large volumes of eolian sands-muds were deposited into the basin. Carbonate input is shed off of the Central Basin Platform, which was dominated by fusulinids, phylloid algae, *Tubiphytes*, ooids, peloids, calcisponges, and other skeletal grains (Simo et al., 2000; Wahlman, 2002, Wahlman and Tasker, 2013). Percent turbidite and debris flow facies from Core 1 and Core 2 is show in the pie charts.

5.3 Mineralogical Relationship between Porosity and Permeability

Siliceous mudstone to detrital and biogenic quartz siltstone and argillaceous siliceous mudstone lithofacies (L1 & L2) have similar porosity and permeability values. These two lithofacies also have the highest average porosity, 11.2% (in both L1 and L2) and permeability, 0.0013 µd in L1 and 0.0015 µd in L2 compared to the other two carbonate lithofacies, L3 and L4 (Table 6). Therefore, rocks containing L1 and L2 lithologies make up the best reservoir rock. In contrast, mud to grain dominated packstones, L4 have the lowest average porosity, 4.9% and lowest average permeability, 0.43 nd. These lithologies are associated with carbonate debrites and grain-rich turbidity current deposition (Ta), and therefore, likely compartmentalize hydrocarbon reservoirs. Carbonate mudstone-wackestones L3 have slightly higher average porosity, 7.5% and permeability, 0.97 nd values than the other carbonate dominated lithofacies, L4 (table 6).

64

Lithofacies	Porosity (%)	Permeability (μd)
L1: Siliceous mudstone-detrital and biogenic quartz siltstone	11.2	0.0013
L2: Argillaceous siliceous mudstone	11.2	0.0015
L3: Carbonate mudstone-wackestone	7.5	0.00097
L4: Mud to grain dominated packstone	4.9	0.00043

Table 6: Lithofacies L1-L4 with corresponding average porosity, % and permeability, μm from measure core. L1 and L2 lithofacies have the highest porosity and permeability values while L3 and L4 have the lowest petrophysical values.

At a whole well scale, porosity ranges from 1% to 13% across both wells, but permeability values remain exceptionally low. Diagenesis and the formation of carbonate and siliceous cements following deposition has a tremendous impact on the range in permeability across all facies. Well 1 permeability ranges from 83 nd to 5.0 μd (A 20), and well 2 permeability ranges from 22.0 nd to 3.32 md (A 21). Mineralogy appears to control porosity and permeability within the rocks. When the percentage of calcite, quartz, and clays are plotted against porosity, calcite content exhibits a negative relationship to porosity (Figure 35). Low porosity can be attributed to calcite cements that were observed in thin section and ESEM that occlude pore space (Figures 25 and 26). On average, carbonate mudstone to packstone lithologies (L3 and L4) have lower porosity and permeability compared to siliceous and argillaceous mudstone and siltstones (L1 and L2) (Table 6, Figures 35 and 37). Carbonate debrite facies F1 consistently demonstrate low porosity and permeability (Figure 38).

The volume of silica and clay content control porosity, permeability, and reservoir quality in the area of this study of the Wolfcamp A. Since the finer turbidite facies (F3-F6) share overlapping lithologies with each other, porosity and permeability relationships had similar responses (Figures 37 and 38). Upon closer observation, porosity demonstrates a positive relationship to quartz and clay content (Figure 35). Lithologies with dominantly quartz and clays

have higher porosity and permeability values (Figure 37). High amounts of silica cements

observed in thin section and ESEM analysis likely contributed to porosity preservation during

syndepositional and early burial diagenesis. Sources of silica cementation were likely detrital and

biogenic silica from sponges and radiolarians that were pervasively recorded in thin section

analysis (Figures 10B, 11B, 36). Initial micro to nano porosity and permeability within the clay

and quartz-rich mudstones to siltstones, although lower than initial porosity of carbonate

lithologies, was likely preserved through the formation of silica cements along pore space by

protecting initial pores from compacting. Microporosity is represented by blue epoxy in thin

section micrographs (Figure 36). Pores are often lined with calcite cement, which is recognized

by high birefringence in cross polarized light. Low porosity and permeability in the calcite-rich

lithofacies is likely due to the precipitation of calcite cement in two forms. Firstly, early marine

cementation along the slope likely contributed to reduced porosity and permeability in the

carbonate mudstone to packstone lithofacies L3 and L4 (Grammer et al., 1993). Additionally,

basinal fluids likely flowed through higher initial porosity of carbonate rocks, allowing for the

precipitation of calcite cements, leading to decreased porosity in coarser grained packstones to

wackestones and carbonate mudstones.
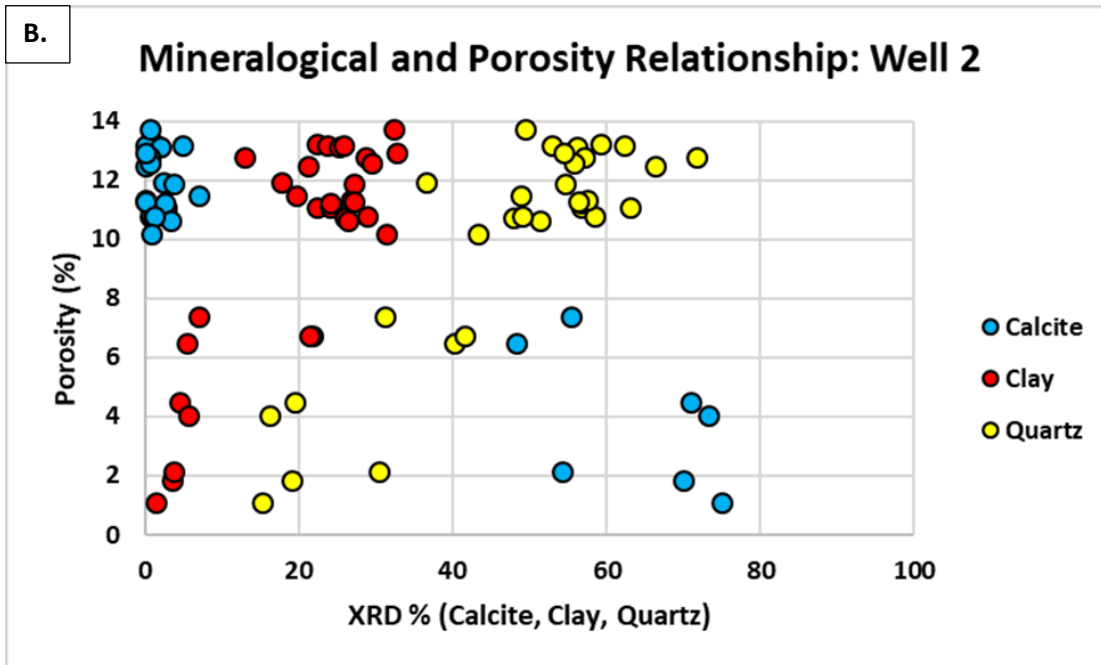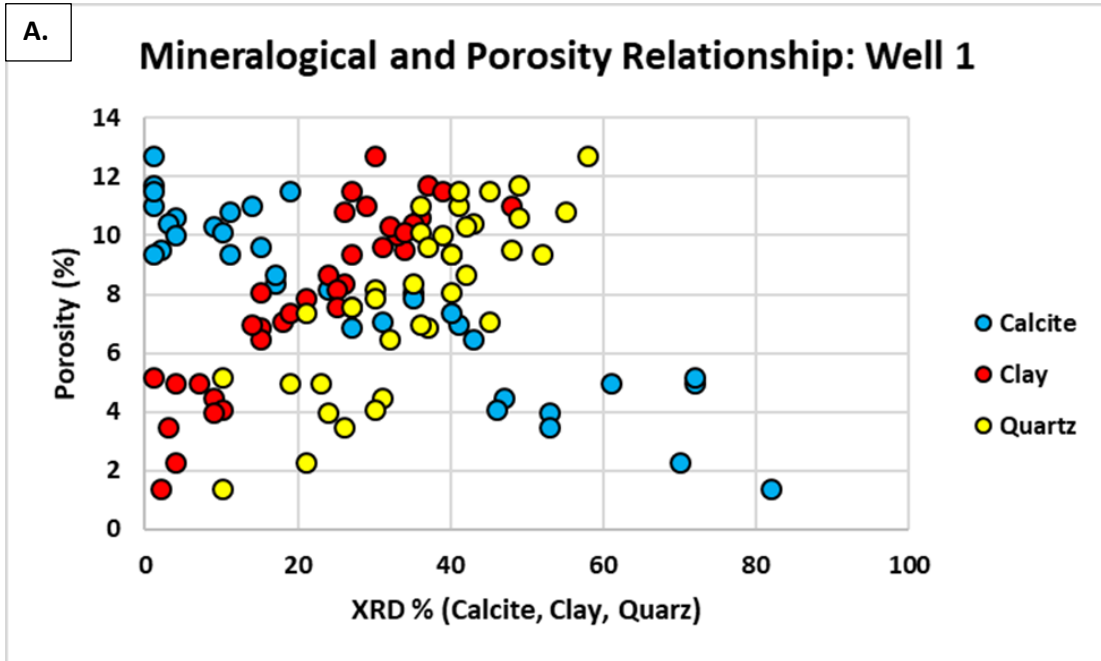
Figure 35: XRD mineralogical and core measured porosity relationship from Core 1 (A) and Core 2 (B). Both graphs display a clear negative relationship between calcite content and porosity. Clay and quartz content show a positive relationship with increased mineralogy content and porosity.
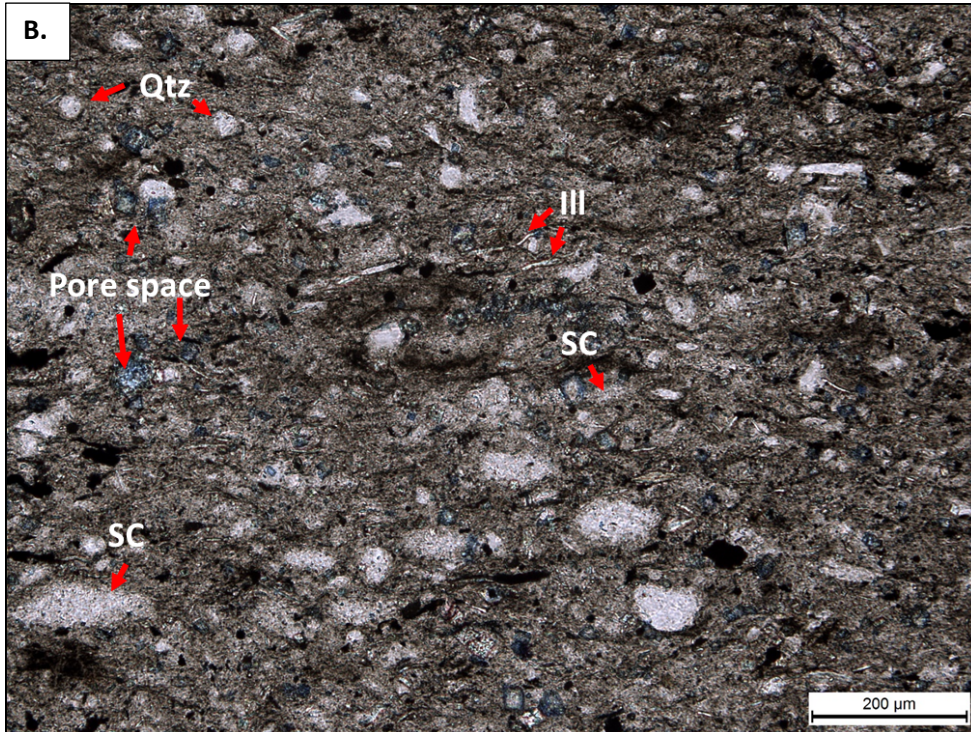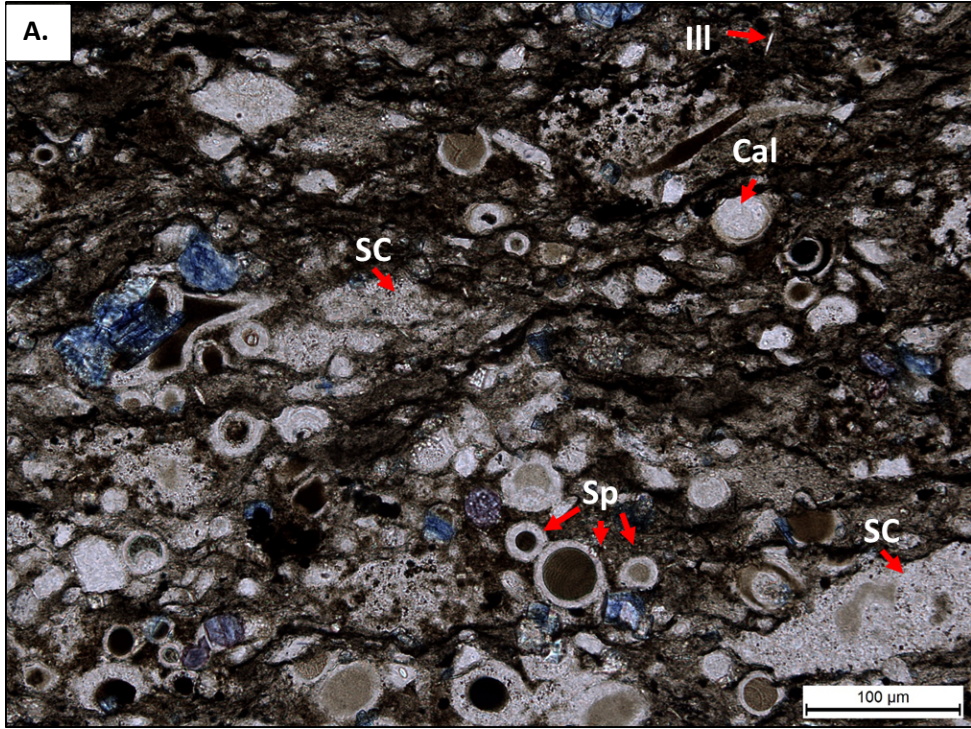
Figure 36: Thin section photomicrographs in plane-polarized light taken from Core 1 showing silica cement (SC), biogenic quartz from radiolarians (R), silicified calcispheres (Cal), siliceous sponge spicules (Sp), and illite clay (Ill) (A). Image B shows significant silica cement (SC), detrital quartz (Qtz), and illite clay (Ill). Blue epoxy represents pore space.

Thus, mineralogy and diagenesis play an essential role in porosity preservation. Lithofacies 1 and 2 demonstrate similar high porosity and permeability. Lithofacies 4 shows the lowest porosity and permeability values. Lithofacies 3 on average has higher porosity and permeability compared to lithofacies 4, but less than lithofacies 1 and 2 (Table 6). The majority of siliceous and argillaceous mudstones-siltstones are deposited in the upper portions of the Bouma sequence; Te and Td. This corresponds to the lower energy suspension settling facies 6 and 7, which have sub centimeter bedding and mineralogy changes impacting reservoir quality.
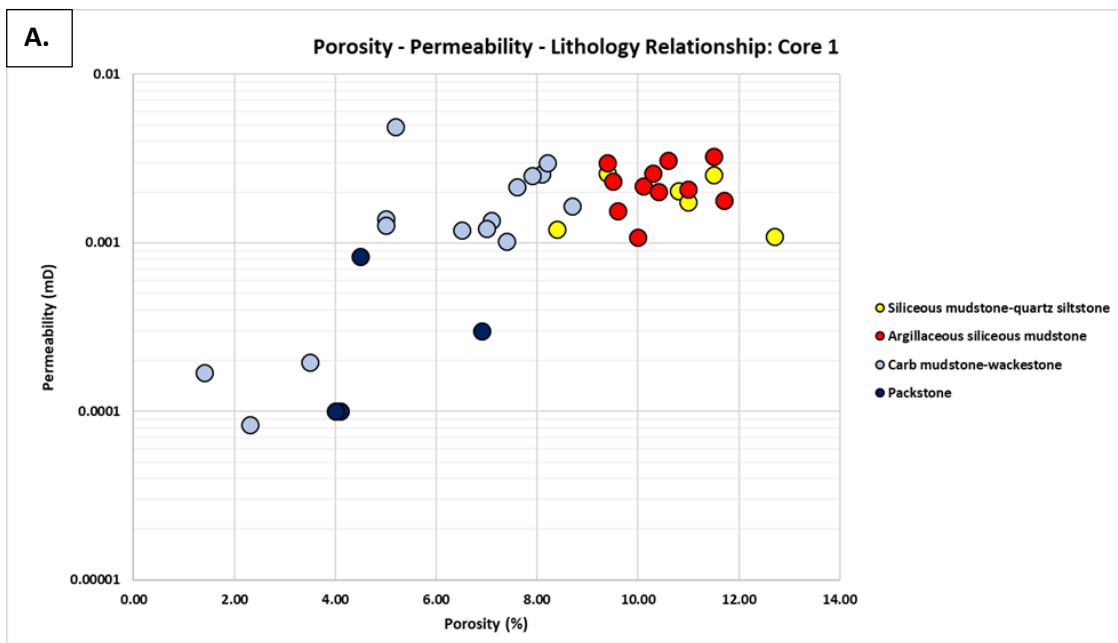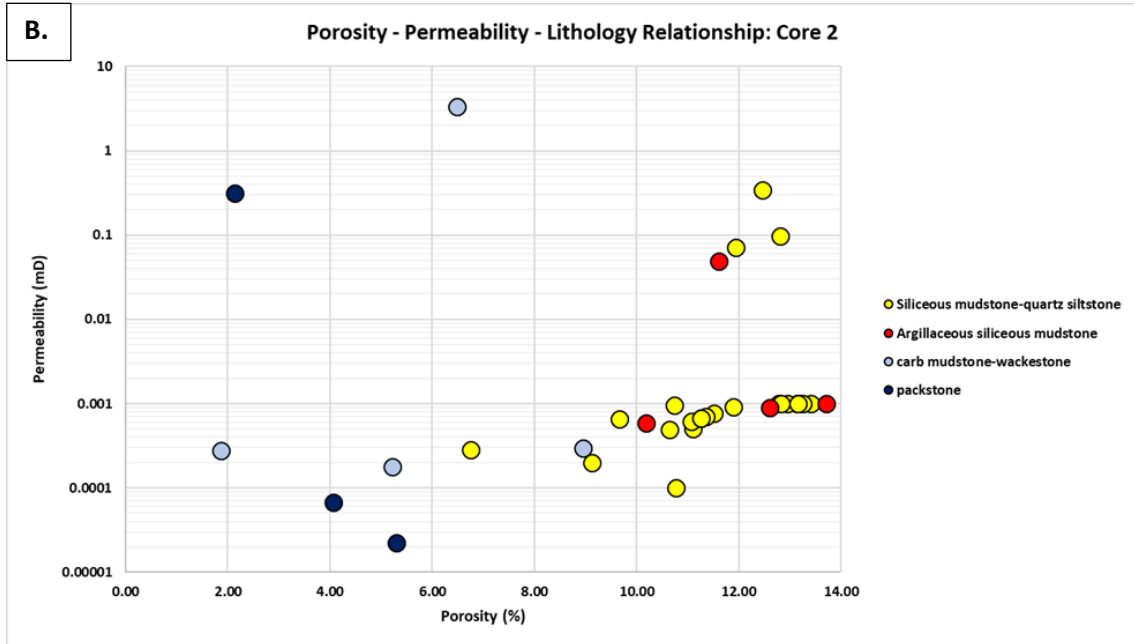
Figure 37: Core measured porosity, permeability, and lithofacies relationship from Core 1 (A) and Core 2 (B). Siliceous and argillaceous mudstones to siltstones display consistently higher porosity and permeability values. Lithofacies 1 and 2 have identical petrophysical responses whereas lithofacies 3 and 4 have overall lower porosity and permeability values. This is due to carbonate cementation occluding pore space.
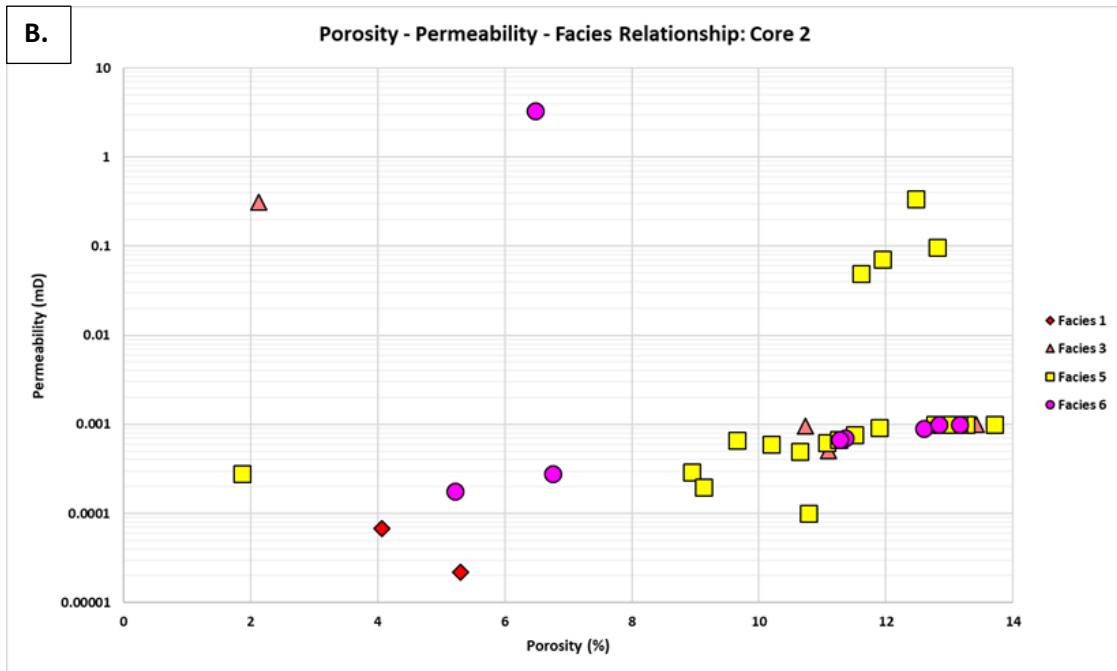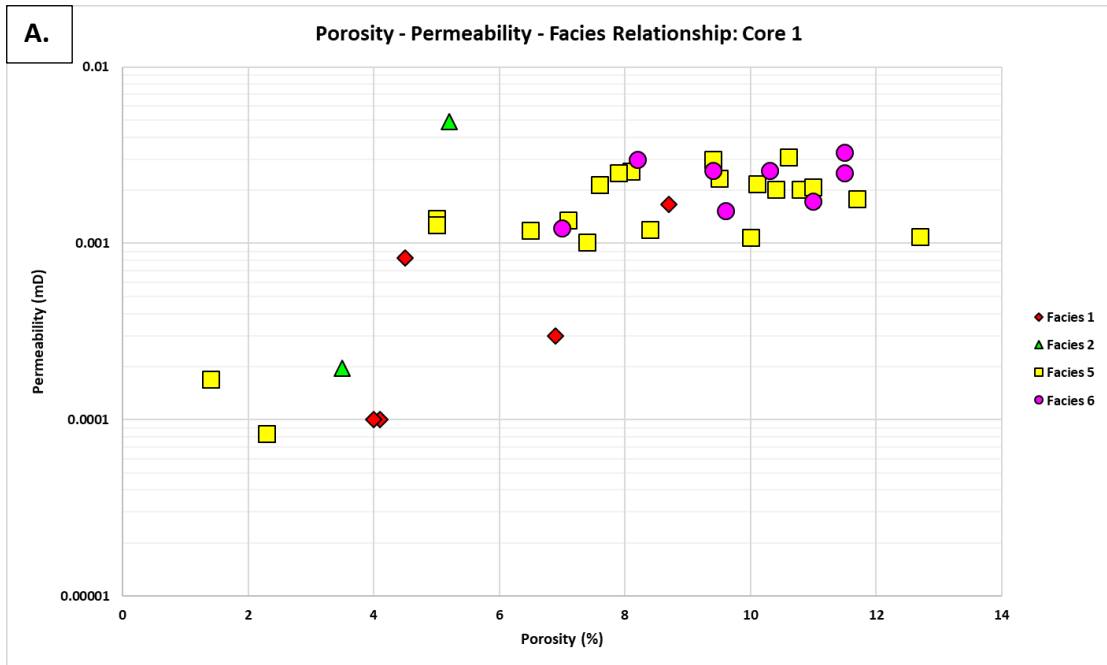
Figure 38: Core measured porosity, permeability, and facies relationship from Core 1 (A) and Core 2 (B). Facies 5 and 6 have identical petrophysical responses due to siliceous and argillaceous mud content. In Figure B, facies 3 partially mimics facies 5 and 6 responses. Coarser grained and carbonate bearing facies F2 and F1 have generally lower porosity and permeability compared to facies 5 and 6.

5.4 Relationship between Pore Type, Pore Architecture, and Permeability

Variations in sediment deposition and diagenesis have a direct relationship in porosity preservation and destruction. Compaction, cementation and mineralization along pore throats reduce porosity and disrupt pore connectivity. Ion-milled ESEM analysis to evaluate pores on the micron to nanometer scale provides evidence of how matrix composition, compaction, mineralization along pore throats, and cementation directly affect core measured porosity and permeability. This relationship can then be translated to regional scale wireline log responses. Thus, analysis of pore geometries and pore architecture on the nanopore to micropore scale can be used as a proxy to predict petrophysical log responses (Eberli et al., 2003; Adams, 2005; Ahr et al., 2005; Weger et al., 2009; Norbisrath et al., 2015; Vanden Berg and Grammer, 2016; Bode et al., 2019).

Perimeter over area (PoA) and dominant pore size (DOMsize) plots are a proxy for relating pore size to pore complexity (Weger et al., 2009). PoA is the ratio between total perimeter that encloses the pore space and the total pore space area (Weger et al., 2009). Small PoA values indicate a simple pore geometry, and large PoA values reflect an intricate pore system. Dominant pore size (DOMsize) is defined as the upper boundary of pore sizes with which 50% of the porosity in an image is composed. It is used as an indicator of effective pore size in each sample (Weger et al. 2009). PoA and DOMsize show that smaller pores have more complex structures and contribute less to permeability (Figures 38 and 39), which is supported by Weger et al. (2009) by the low porosity and permeability measured from core. The majority of pore contribution within carbonate facies is from interparticle pores between cemented clay-sized intraclastic grains, skeletal fragments, and cleavage-sheets associated with clays. Diagenetic calcite cements and clays occluding pore throats, segment and isolate pore area (Figures 25 and 26), thus causing low permeability.

Pore length vs pore count (Figure 39 A-C) shows pore size distribution across facies F1, F5, and F6. Each bar is representative of the number of pores identified in the size ranges (0.10, 1, 10 µm). Facies 1 has the smallest pore sizes compared to facies F5 and F6 (Figure 39). Facies 5 and 6 have a larger distribution and larger pore sizes compared to the carbonate debrite facies. Carbonate debrite facies also have the highest average PoA values (23.2) and lowest DOMsize (0.22), suggesting smaller pores (low DOMsize) and a complex pore structure (high PoA) that contribute less to permeability. This trend is proven in core measured porosity and permeability, where carbonate debrite facies show the lowest measured porosity (4.9%) and permeability (0.00043 µd). Parallel laminated muddy turbidites (F5) and massive muddy turbidites (F6) have similar DOMsize and PoA values. Average DOMsize in facies 5 and 6 were both 0.28, which is higher compared to carbonate debrite facies. PoA values across both facies F5 and F6 were 18.3, and 20.2, respectively. This trend in greater pore space is also reflected in higher core measured porosity and permeability values. Overall, siliceous and argillaceous mudstones that make up facies 5 and 6 have larger pores (larger DOMsize) and simpler pore structures (smaller PoA) that contribute more to permeability when compared to calcite-rich mudstones to packstones that dominate carbonate debrites F1 and lower portions of the Bouma sequence in turbidite facies (Ta, Tb; F2, F3) (Figures 35, 37, and 38; table 6).

Perimeter over Area (PoA) plotted against pore length also provides a first-hand glance at pore size distribution. Facies 5 and 6 have a unimodal distribution, and facies 1 has a weaker overall negative relationship between PoA and pore length (Figure 39, D-F). Facies 1 has the least number of pores, and facies 5 has the highest pore count and greater number of pores with higher PoA values.
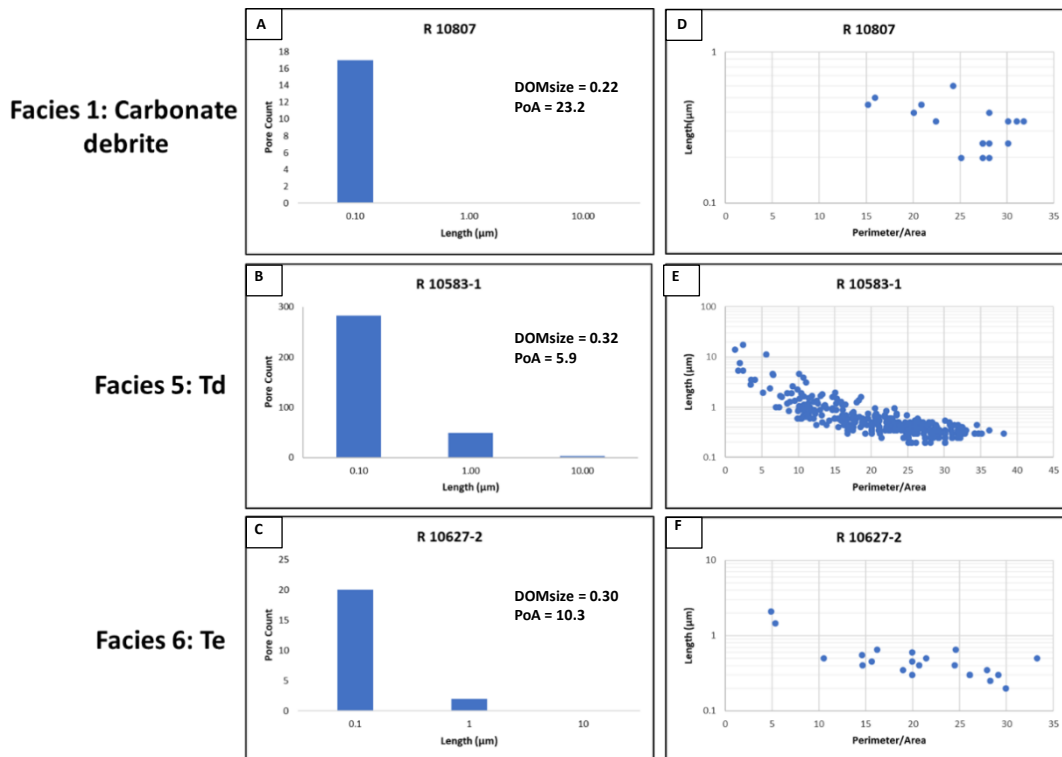
Figure 39: Pore size distribution graphs showing pore length by pore count (A-C), and PoA by pore length (D-F) of representative samples across samples facies F1, F5, and F6. Facies 5 has the most pores and has more pores with higher perimeter/area compared to the other two facies.

PoA and DOMsize values in siliceous and argillaceous mud to siltstones, L1 and L2 within facies F5 and F6 show that larger pores have simpler structures and have a higher contribution to permeability. Rocks containing L1 and L2 lithologies within facies 5 and 6 show greater preservation of primary porosity compared to L3 and L4 rocks that are abundant in carbonate debrite facies F1. Greater porosity preservation in L1 and L2 is likely contributed to early formation of siliceous cements. Although pore space in these facies is frequently occluded by pore bridging clays (Figure 27), significant microporosity between siliceous cements, clays, and organic materials (Figures 28-30) contribute to higher porosity and permeability than carbonate-rich mudstones and packstones that is confirmed in core plug measurements (Tables 5 and 6).
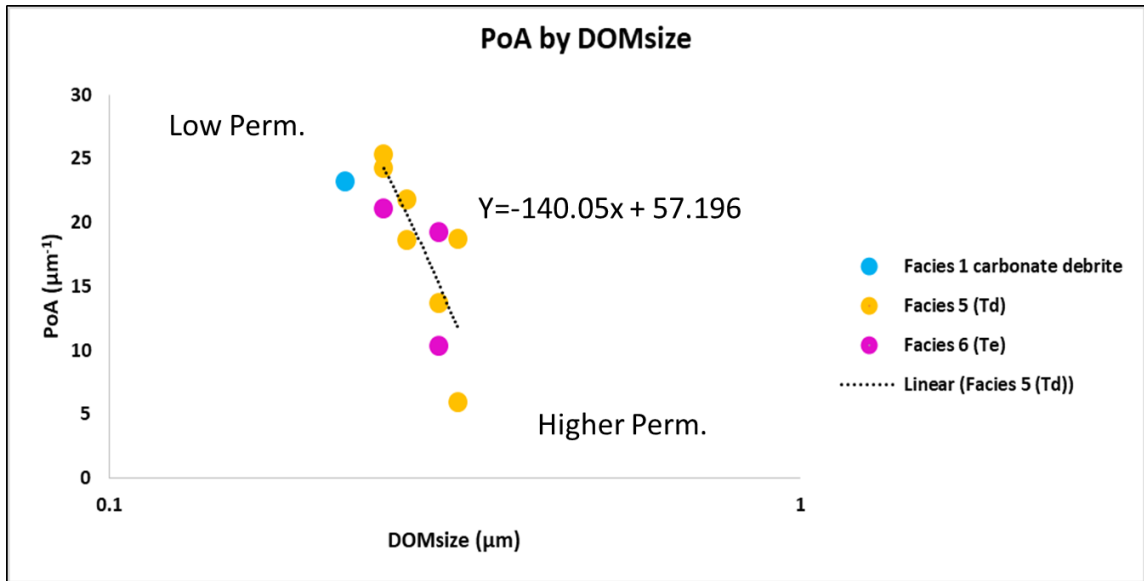
Figure 40: DOMsize vs PoA graph plotted from all images analyzed using digital image analysis across facies F1, F5, and F6. Samples with smaller pore sizes have higher PoA, indicating more complicated pore structure.

CHAPTER V

CONCLUSIONS

This study concludes that sediment gravity flow type controls facies distribution within the study area. In both cores, mixed siliciclastic and carbonate amalgamated turbidites dominated sedimentation. Debris flow deposits, primarily carbonate in composition, were observed in both cores. These deposits have low porosity and permeability and compartmentalize hydrocarbon reservoirs. Muddy slumps were the least common type of gravity flow deposits preserved in core. Since lithologies in Core 1 and Core 2 are dominated by siliceous, argillaceous, and carbonate mudstones to siltstones, gravity flow deposits preserved in vertical succession likely were located in distal portions of basinal channel-fan complexes, or lower slope strike-extensive muddy aprons. Facies 5 and 6 with L1 and L2 lithologies have the best porosity and permeability due to the early formation of siliceous cements, and represent deposition in distal, fringe portions of channel fan complexes. These two facies with L1 and L2 lithologies are the best reservoir rocks. Vertical stacking patterns of facies indicate that gravity flow deposits are compensationally stacked, filling in topographic lows, and preserve multiple slope failure events.

There are several pore types within the Wolfcamp A. Common pores observed in ESEM imaging are controlled by mineralogy and diagenetic alterations. While facies share similar pore types, differences in pore size, distribution, and shape on the nanopore to micropore scale contribute significantly to core porosity, permeability, and overall reservoir quality.

Analysis of geometric pore parameters including PoA and DOMsize indicate that smaller pores within cemented carbonate mudstones, wackestones, and packstones are more complex and contribute less to permeability. On the other hand, PoA and DOM size values from siliceous mudstones, detrital and biogenic quartz siltstones, and argillaceous mudstones found in the planar laminated and massive muddy turbidite facies (F5-F6) show that larger pores within silica cements and clays are simpler and contribute more to permeability. Biogenic silica cement formation in siliceous to argillaceous mudstones protects the pores in the rock from burial compaction, resulting in higher porosity and permeability. This knowledge facilitates in predicting where to encounter reservoirs with the highest porosity and permeability.

Overall, deposition and diagenesis control pore system architecture and petrophysical response. Primary lithology, carbonate and silica cementation, and compaction are the main factors controlling heterogeneity and reservoir quality within the Wolfcamp A formation in this study area.

REFERENCES

Adams, J. E., 1965, Stratigraphic-Tectonic Development of Delaware Basin: AAPG
    Bulletin, v. 49, p. 2140-2148, doi: 10.1306/a6633888-16c0-11d7-
    8645000102c1865d.

Adams, A.J., 2005, Relationships Between Observed Pore and Pore-Throat Geometries,
    Measured Porosity and Permeability, and Indirect Measures of Pore Volume by
    Nuclear Magnetic Resonance [unpublished PhD dissertation]: Texas A&M
    University, College Station, 277 p.

Ahr, W.M., Allen, D., Boyd, A., Bachman, H.N., Smithson, T., Clarke, E.A., Gzara,
    K.B.M., Hassall, J.K., Murty. C.R.K., Zubari, H. Ramamoorthy, R., 2005,
    Confronting the Carbonate Conundrum, Oilfield Review, v. 17(1), p. 18-29.

Anselmetti, F. S., G. A. von Salis, K. J. Cunningham, and G. P. Eberli, 1997, Acoustic
    properties of Neogene carbonates and siliciclastics from the subsurface of the
    Florida Keys: Implications for seismic reflectivity: Marine Geology, v. 144, p. 9-
    31.

Asmus, J. A. and G. M. Grammer, 2013. Characterization of deep-water carbonate
    turbidites and mass-transport deposits utilizing high-resolution electrical borehole
    image logs: Upper Leonardian (lower Permian) Upper Bone Springs Limestone,
    Delaware Basin, Southeast New Mexico and West Texas: Gulf Coast Association
    of Geological Societies Transactions, v. 63, p. 27-65.

Asmus, J. J., 2012, Characterizing the Internal Architecture of Upper Bone Spring
    Limestone Turbidites and Mass Transport Deposits (MTDs) Utilizing High
    Resolution Image Log Technology, Master's Thesis, Western Michigan
    University, Kalamazoo, Michigan, 95 p.

Archie, G.E., 1942 The Electrical Resistivity Log as an Aid in Determining Some
    Reservoir Characteristics, v. 146, p. 54-62.

Baumgardner, R. W., W. A. DiMichele, N. de Siqueira Vieira, 2016. An early Permian
    coastal flora dominated by Germaropteris martinsii from basinal sediments in the
    Midland Basin, West Texas: Palaeogeography, Palaeoclimatology,
    Palaeoecology, v. 456, p. 409-422.

Bernet, K. H., Eberli, G. P., and Gilli, A., 2000, Turbidite Frequency and Composition in the Distal Part of the Bahama Transect, in: Swart, P. K., Eberli, G. P., Malone, M. J., and Sarg, J. F., (eds.), Proceedings of the Ocean Drilling Program, Scientific Results, v. 166, p. 45-60.

Betzler, C., Reijmer, J. J. G., Bernet, K., Eberli, G.P., and Anselmetti, F.S., 1999, Sedimentary Patterns and Geometry of Bahamian Outer Carbonate Ramp (Miocene-Lower Pliocene, Great Bahama Bank), Journal of Sedimentology, v. 46, p. 1127-1143.

Bode, I.Y., Zhang, C., Vanden Berg, B., Grammer, G.M., 2019, Multiscale Imaging and Nuclear Magnetic Resonance Pore Characterization in Unconventional Carbonate Mudrocks of the Southern Midcontinent (USA): Mississippian Lime Play, Society for Sedimentary Geology v. 112 p. 196-219.

Bouma, A. H., 1964, Turbidites, Developments in Sedimentology, v. 3, p. 247-256.

Choquette, P.W., Pray, L.C., 1970, Geologic Nomenclature and Classification of Porosity in Sedimentary Carbonates, American Association of Petroleum Geologists Bulletin v. 54 p. 207-250.

Cook, H. E., McDaniel, P. N., Mountjoy, E. W., and Pray, L. C., 1972, Allochthonous Carbonate Debris Flows at Devonian Bank ("reef") Margins, Alberta, Canada, Bulletin of Canadian Petroleum Geology, v. 20, p. 439-486.

Cook, H. E. and H. T. Mullins, 1983, Basin margin environment, in P. A. Scholle, D. G. Bebout, and C. H. Moore, eds., Carbonate depositional environments: American Association of Petroleum Geologists Memoir 33, Tulsa, Oklahoma, p. 449-617.

Dunham, R.J., 1962, Classification of Carbonate Rocks According to Depositional Texture, In Ham WE (Editor), Classification of Carbonate Rocks-A symposium, Memoir 1: American Association of Petroleum Geologists, Tulsa, Oklahoma p. 108-121.

Drzewiecki, P.A., Simo, J.A., 2002, Depositional Processes, Triggering Mechanisms and Sediment Composition of Carbonate Gravity Flow Deposits: Examples from the Late Cretaceous of the South-Central Pyrenees, Spain, Sedimentary Geology, v. 146, p. 155-189

Eberli, G. P., 1991, Growth and Demise of Isolated Carbonate Platforms: Bahamian Controversies, Controversies in Modern Geology, p. 231-248.

Eberli, G. P., F. S. Anselmetti, and M. L. Incze, 2003, Factors controlling elastic properties in carbonate sediments and rocks: The Leading Edge, v. 22, p. 654-660.

Fischer, A. G. and Sarnthein, M., 1988, Airborne Silts and Dune-Derived Sands in the Permian of the Delaware Basin, Journal of Sedimentary Petrology, v. 58, p. 637-643.

Ginsburg, R. N., ed., 2001, Subsurface geology of a prograding carbonate platform margin, Great Bahama Bank: Results of the Bahamas Drilling Project: SEPM Special Publication 70, 265 p.

Glaser, K. S. and Droxler, A. W., 1991, High Production and Highstand Shedding from Deeply Submerged Carbonate Banks, Northern Nicaragua Rise, Journal of Sedimentary Petrology, v. 61, p. 128-142.

Goldstein, R.H., E.K. Franseen, R. A Dvoretsky, and R.J. Sweeney, 2012, Controls on Focused-Flow and Dispersed-Flow Deepwater Carbonates: Micocene Agua Amarga Basin, Spain: Journal Sedimentary Research, V. 82, P. 499-520.

Grammer, G.M. and Ginsburg, R.N., 1992, Highstand Versus Lowstand Deposition on Carbonate Platform Margins: Insight from Quaternary Foreslopes in the Bahamas, Marine Geology, 103: 125-136.

Grammer, G.M., Ginsburg, R.N, Swart, P.K., McNeill, D.F., Jull, A.T., and Prezbindowski, D.R., 1993, Rapid Growth Rates of Syndepositional Marine Aragonite Cements in Steep Marginal Slope Deposits, Bahamas and Belize, Journal of Sedimentology, v. 63, p. 983-989.

Grammer, G. M., Harris, P. M., and Eberli, G. P., 2004, Integration of Outcrop and Modern Analogs in Reservoir Modeling: Overview with Examples from the Bahamas, in: Grammer, G. M., Harris, P. M., and Eberli, G. P., (eds.), Integration of Outcrop and Modern Analogs in Reservoir Modeling, AAPG Memoir 80, p. 1-22.

Griggs, G. B. and Kulm, L. D., 1970, Sedimentation in Cascadia deep-sea channel: Geological Society of America Bulletin, v. 81, p. 1361-1384.

Handford, C. R. and R. G. Loucks, 1993, Carbonate Depositional Sequences and Systems Tracts-responses of carbonate platforms to relative sea-level changes, in R. G.

Heezen, B.C. and Ewing, M., 1952, Turbidity currents and submarine slumps, and the 1929 Grand Banks earthquake: American Journal of Science, v. 250 p. 849-873.

Hunt, D. and Fitchen W.M., 1999, Compaction and the Dynamics of Carbonate – Platform Development: Insights from the Permian Delaware and Midland Basins, Southeast New Mexico and West Texas, U.S.A., SEPM Special Publication No. 61, p. 75-106.

Jo, A., Eberli, G. P., Grasmueck, M., 2014, Margin Collapse and Slope Failure Along Southwestern Great Bahama Bank, Sedimentary Geology, v. 317, p. 43-52, doi: 10.1016/j.sedgeo.2014.09.004

Loucks and J. F. Sarg, eds., Carbonate Sequence Stratigraphy: Recent Developments and Applications: American Association of Petroleum Geologists Memoir 57, p. 3-41.

Haq, B.U., Schutter, S.R., 2008, A Chronology of Paleozoic Sea-Level Changes, Science, v. 322, p. 64-68

Hooke, R.L., Schlager, W., 1980, Geomorphic Evolution of the Tongue of the Ocean and the Providence Channels, Bahamas, Marine Geology, v. 35, p. 343-366

Houghton, P., Barker, S., Mccafrey, W., 2003, 'Linked' debrites in sand-rich turbidite systems – origin and significance: Journal of Sedimentology, v. 50, p. 459-482.

Haughton, P., C. Davis, W. McCaffrey, S. Barker, 2009, Hybrid sediment gravity flow deposits-classification, origin and significance: Marine and Petroleum Geology, v. 26, p. 1900-1918.

Hill, C. A., 1996, Geology of the Delaware Basin Guadalupe, Apache, and Glass Mountains New Mexico and West Texas, Permian Basin Section-SEPM Publication No. 96-39, 480 p.

Hills, J. M., 1984, Sedimentation, tectonism, and Hydrocarbon Generation in Delaware Basin, West Texas and Southeastern New Mexico, AAPG Bulletin, v. 68, p. 250-267.

Janson, X., Kerans, C., Bellian, J. A., Fitchen, W., 2007, Three-dimensional Geologic and Synthetic Seismic Model of Early Permian Redeposited Basinal Carbonate Deposits, Victorio Canyon, west Texas, AAPG Bulletin, v. 91, p. 1405-1436.

Janson, X., Kerans, C., Playton T., Clayton, J., Winefeld, P., Burgess, P., 2012, Stratigraphic Models and Exploration Plays of Slope and Basin-Floor Carbonates, American Association of Petroleum Geologists Annual Convention and Exhibition, 22-25 April 2012, Long Beach, California.

Jo, A., Eberli, G. P., Grasmueck, M., 2015, Margin Collapse and Slope Failure Along Southwestern Great Bahama Bank, Sedimentary Geology, v. 317, p. 43-52.

Kenter, J. A. M., 1990, Carbonate Platfrom Flanks: Slope Angle and Sediment Fabric, Sedimentology, v. 37, p. 777-794.

Kerans, C. and Tinker, S.W., 1999, Extrinsic Stratigraphic Controls on Development of the Capitan Reef Complex, SEPM Special Publication No. 65, p.15-36.

Kustatscher, E., K. Bauer, R. Butzmann, T. C. Fischer, B. Meller, J. H. Van Konijnenburg-Ban Cittert and H. Kerp, 2014, Sphenophytes, pteridosperms and possible cycads from the Wuchiapingian (Lopingian, Permian) of Bletterbach (Dolomite, northern Italy): Review of Palaeobotany and Palynology, v. 208, p. 65-82.

Kvale, E. P., C. Flenthrope, and C. Mace, 2017, Carbonate-Dominated Hybrid Sediment Gravity Flows Within the Upper Wolfcamp, Delaware Basin, USA: Vectors for Transmitting Terrestrial Organics into a Deep Marine Basin: Abstract, AAPG 2017 Annual Convention and Exhibition.

Kvale, E. P., Bowie, C. M., Flenthrope, C., Mace, C., Pritchard, J. M., Price, B., Anderson, S., DiMichele, W. A., 2019, Mixed carbonate-siliciclastic hybrid event beds in unconventional hydrocarbon reservoirs Delaware Basin, southeast New Mexico and west Texas, USA, AAPG Bulletin, 47 p.

Loucks, R.G. Reed, R.M., Ruppel, S.C., Hammes, U., 2012, Spectrum of Pore Types and Networks in Mudrocks and a Descriptive Classification for Matrix-Related Mudrock Pores, American Association of Petroleum Geologists Bulletin v. 96, p. 1071-1098.

Middleton, G. V., and Hampton, M. A., 1973, Sediment Gravity Flows: Mechanics of Flow and Deposition, in: Middleton, G. V., and Bouma, A. H., (eds.), Turbidites and Deep-Water Sedimentation, SEPM Pacific Section, Los Angeles, California, p. 1-38.

Montañez, I. P., N. J. Tabor, D. Niemeier, W. A. DiMichele, T. D. Frank, C. R. Fielding, J. L. Isbell, L. P. Birgenheier, and M. C. Rygel, 2007, CO2-forced climate and vegetation instability during Late Paleozoic deglaciation: Science, v. 315, p. 87-91.

Mulder, T., and J. Alexander, 2001, The physical character of subaqueous sedimentary density flows and their deposits: Journal of Sedimentology, v. 48, p. 269-299.

Mullins, H.T., 1983, Modern Carbonate Slopes and Basins of the Bahamas, in Cook, H.E., Hine, A.C., and Mullins, H.T., (eds.), Platform Margin and Deep-Water Carbonates, SEPM short course Notes No. 12, p. 4-1 to 4-138.

Mullins, H. T. Heath, K. C., Van Buren, H. M., and Newton, C. R., 1984, Anatomy of a modern open-ocean carbonate slope: northern Little Bahama Bank: Sedimentology, v. 31, p. 141-168.

Mutti, E., Tinterri, R., Remacha, E., Mavilla, N., Angella, S., and Fava, L., 1999, An Introduction to the Analysis of Ancient Turbidite Basins from an Outcrop perspective, AAPG Continuing Education Course Note Series 39, p. 96.

Mutti, E., Ricci Lucchi, F., Seguret, M., and Zanzucchi, G., 1984, Seismoturbidites: A new group of resedimented deposits: Marine Geology, v. 55 p. 103-116.

Norbisrath, J.H., Eberli, G.P., Laurich, B., Desbois, G., Weger, R.J., Urai, J.L., 2015, Electrical and Fluid Flow Properties of Carbonate Microporosity Types from Multiscale Digital Image Analysis and Mercury Injection, American Association of Petroleum Geologists Bulletin, v. 99, p. 2077-2098.

Normark, W.R. and Piper, D.J.W., 1991, Initiation Processes and Flow Evolution of Turbidity Currents: Implications for the Depositional Record, SEPM Special Publication 46, p. 207-230.

Ortega, M., 2017, Permian Basin ends 2017 by beating decades-old record, October 30, 2018, https://www.bizjournals.com/albuquerque/news/2017/12/28/permian-basin-ends-2017-by-beating-decades-old.html.

Playton, T. E. and C. Kerans, 2002, Slope and toe-of-slope deposits shed from a late Wolfcampian tectonically active carbonate ramp margin: Gulf Coast Association of Geological Societies, v. 52, p. 811-820.

Playton, T.E., Kerans, C., 2006, Latest Wolfcampian Tectonism as a Control on Early Leonardian Carbonate Slope Channel Complexes: Models for Wolfcampian Slope Exploration, West Texas Geological Society Annual Symposium, No. 06-117, p. 88-103

Posamentier, H. W., and Martinsen, O. J., 2011, The Character and Genesis of Submarine Mass-Transport Deposits: Insights from Outcrop and 3D Seismic Data, in: Shipp, C. R., Weimer, Paul, and Posamentier, H. W. (eds.), Mass-Transport Deposits in Deepwater Settings: SEPM Special Publication 96, p. 11-42.

Posamentier, H. W., and Walker, R. G., 2006, Deep-Water Turbidites and Submarine Fans, SEPM Special Publication 84, p. 399-520.

Read, J. F., 1985, Carbonate platform facies models: AAPG Bulletin, v. 69, p. 1-21.

Reijmer, J.J.G., Ten Kate, W.G.H., Sprenger, A., and Schlager, W., 1991, Calciturbidite Composition Related to Exposure and Flooding of a Carbonate Platform (Triassic, Eastern Alps.): Sedimentology, v. 38, p. 1059-1074.

Ricci Lucchi, F., and Valmori, E., 1980, Basin-wide turbidites in a Miocene, "over-supplied" deep-sea plain: A geometrical analysis: Sedimentology, v. 27, p. 241-270.

Rygel, M. C., C. R. Fielding, T. D. Frank, L. P. Birgenheier, 2008, The magnitude of Late Paleozoic glacioeustatic fluctuations: a synthesis: Journal Sedimentary Research, v. 78, p. 500-511.

Saller, A. H., J. W. Barton, and R. E. Barton, 1989, Slope sedimentation associated with a vertically building shelf, Bone Spring Formation, Mescalero Escarpe Field, Southeastern New Mexico, in P. D. Crevello, J. L. Wilson, F. Sarg, and J. F. Read, eds., Controls on carbonate platform and basin development: Society of Economic Paleontologists and Mineralogists (Society for Sedimentary Geology) Special Publication 44, Tulsa, Oklahoma, p. 275-288.

Schlager, W., Reijmer, J. G., and Droxler, A., 1994, Highstand Shedding of Carbonate Platforms, Journal of Sedimentary Research, v. B64, p. 270-281.

Schumaker, R. C., 1992, Paleozoic Structure of the Central Basin Uplift and Adjacent Delaware Basin, West Texas, AAPG Bulletin, v. 76, p. 1804-1824.

Shanmugam, G. and Moiola, R. J., 1984, Eustatic control of calciclastic turbidites, Geology, v. 56, p. 273-278.

Silver, B.A. and Todd, R.G.,1969, Permian Cyclic Strata, Northern Midland and Delaware Basins, West Texas and Southeast New Mexico, AAPG Bulletin, v.53, P.2223-2251

Simo, J.A., Wahlman, G.P., Stoklosa, M.L., Beall, J.L., 2000, Permian Platforms and Reefs in the Guadalupe and Hueco Mountains, SEPM Field Trip Guide, p. 5-46

Tripsansas, E. K., Piper, D. J. W., Jenner, K. A., and Bryant, W. R., 2008, Submarine Mass-Transport Facies: New Perspectives on Flow Processes from Cores on the Eastern North American Margin: Journal of Sedimentology, v. 55, p. 97-136.

Ulmer-Scholle, D.S., Scholle, P.A, Schieber, J., and Raine R.J., 2014, A Color Guide to the Petrography of Sandstones, Siltstones, Shales and Associated Rocks, Mudrocks: Siltstones, Mudstones, Claystones & Shales, AAPG Memoir 109, p. 198-199.

Vanden Berg, B., and Grammer, G. M., 2016, Pore Architecture Characterization of Carbonate Mudrock Reservoir: Insights from the Mid-Continent "Mississippi Lime", in T. Olson, ed, Imaging Unconventional Reservoir Pore Systems: AAPG Memoir 112, p. 185-231.

Vanden Berg, B., and Grammer, G. M., 2018, A Comparison of the Relationship Between Measured Acoustic Response and Porosity in Carbonates Across Different Geologic Periods, Depositional Basins, and with Variable Mineral Composition: Interpretation, v. 6(2), p. T245-T256.

Wahlman, G.P., 2002, Upper Carboniferous - Lower Permian (Bashkirian – Kungurian) Mounds and Reefs, SEPM Special Publication No. 72, p. 271-338

Wahlman, G. P., and D. R. Tasker, 2013, Lower Permian (Wolfcampian) Carbonate Shelf-Margin and Slope Facies, Central Basin Platform and Hueco Mountains, Permian Basin, West Texas, USA: Deposits, Architecture, and Controls of Carbonate Margin, Slope and Basinal Settings, SEPM Special Publication, v. 105, p. 305–333, doi:10.2110/sepmsp.105.09.

Walker R.G., 1978, Deep-Water Sandstone Facies and Ancient Submarine Fans: Models for Exploration for Stratigraphic Traps, American Association of Petroleum Geologists Bulletin, v 62. p. 932-966.

Weger, R.J., Eberli, G.P., Baechle, G.T., Massaferro, J.L., Sun, Y.F., 2009, Quantification of Pore Structure and its Effect on Sonic Velocity and Permeability in Carbonates: American Association of Petroleum Geologists Bulletin, v. 93, p. 1297-1317.
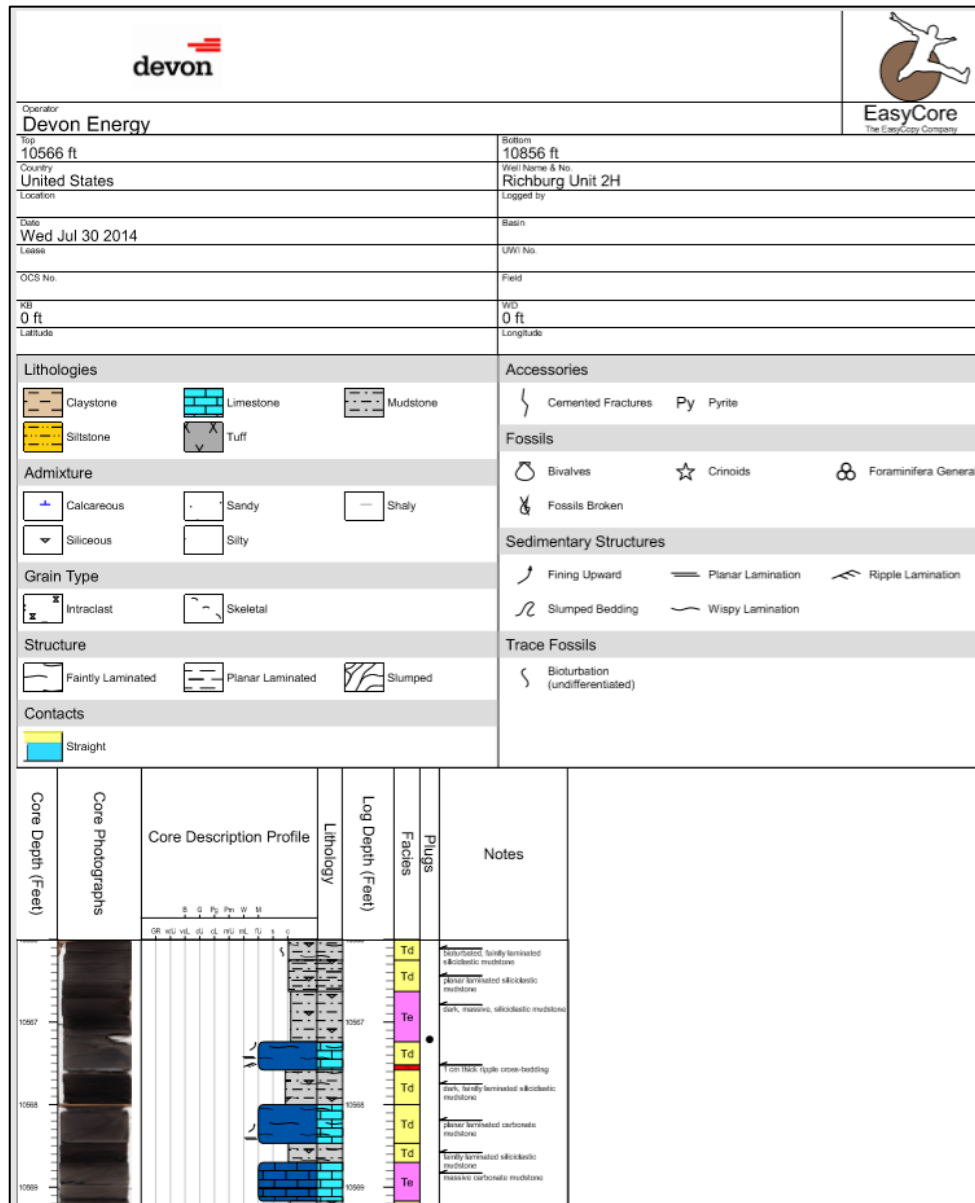
Figure 41: Well 1 core description with lithology, facies and corresponding core photos. Well 1 contains 290 ft of core. Full core description is attached in CD.

Figure 42: Well 2 core description with lithology, facies and corresponding core photos. Well 2 contains 233 ft of core. Full core description is attached in CD.
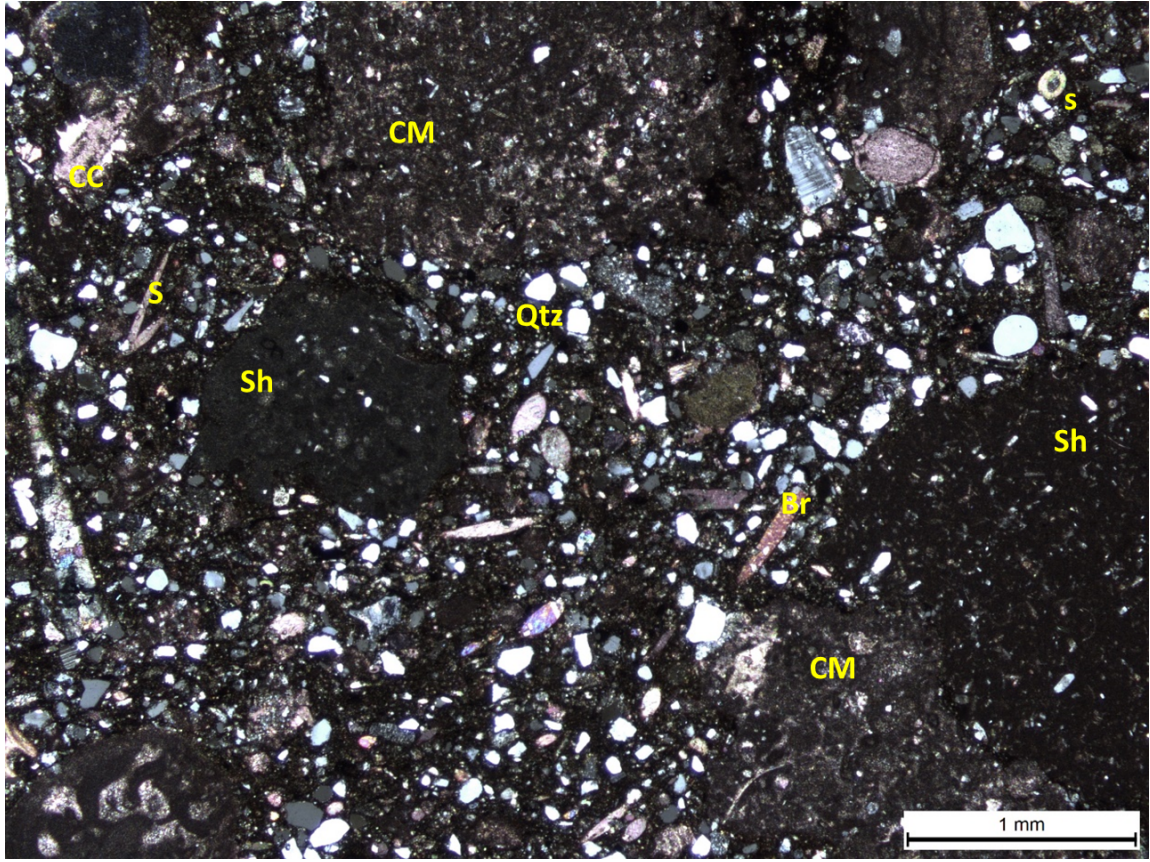
Figure 43: Thin section photomicrograph of F1/L4: carbonate debrite; grain dominated packstone in cross-polarized light. XRD mineralogy of the sample is 73% calcite, 16% quartz, 6% clay. Carbonate mudstone intraclasts (CM), shale intraclasts (Sh), quartz grains (Qtz), calcified sponge spicules (s), and brachiopod fragment (Br) are labeled and abundant.
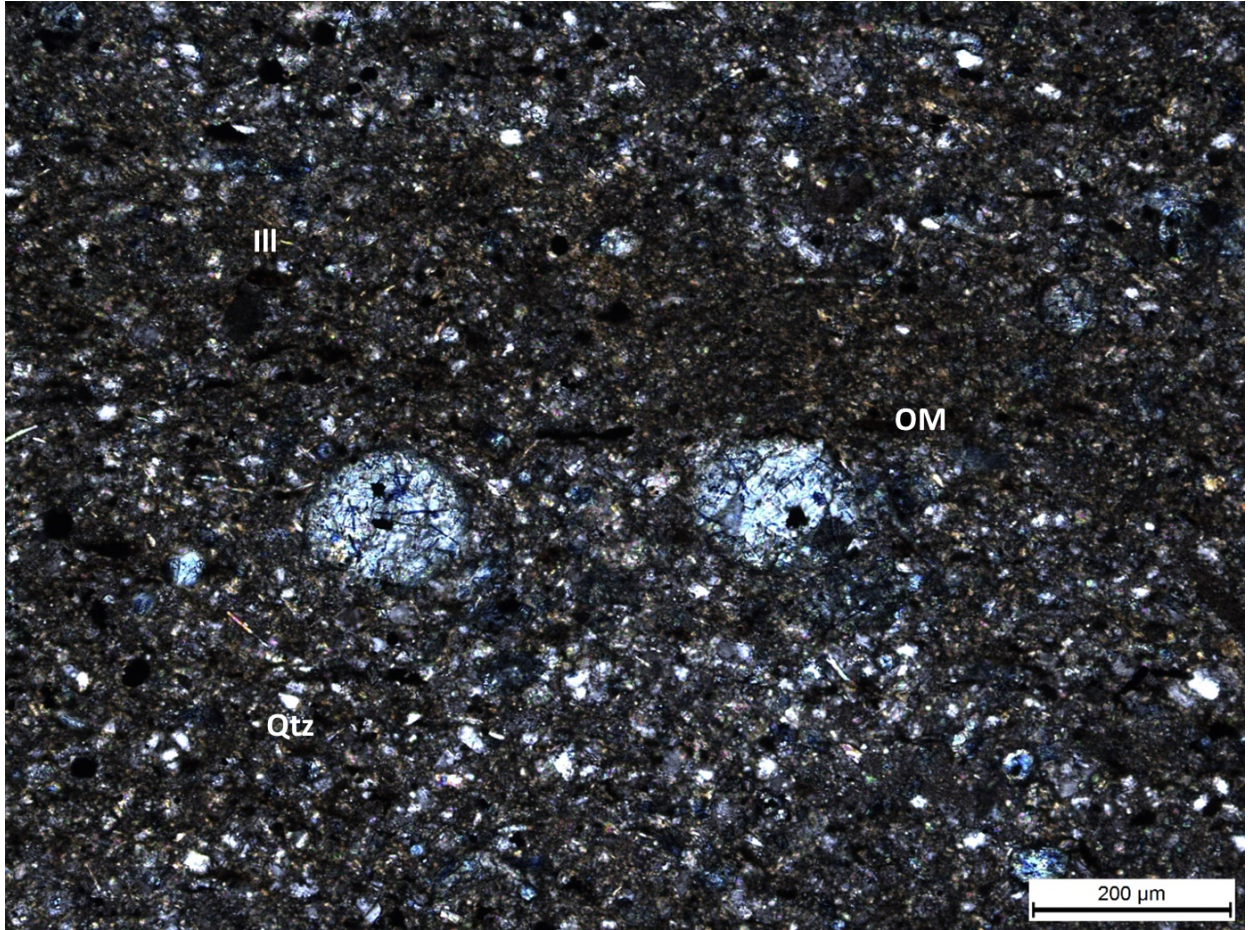
Figure 44: Thin section photomicrograph in cross-polarized light of F3/L1: parallel laminated turbidite (Tb); siliceous mudstone to detrital and biogenic quartz siltstone. This sample is dominated by quartz grains (Qtz), dark organic matter (OM), and illite clays (Ill).
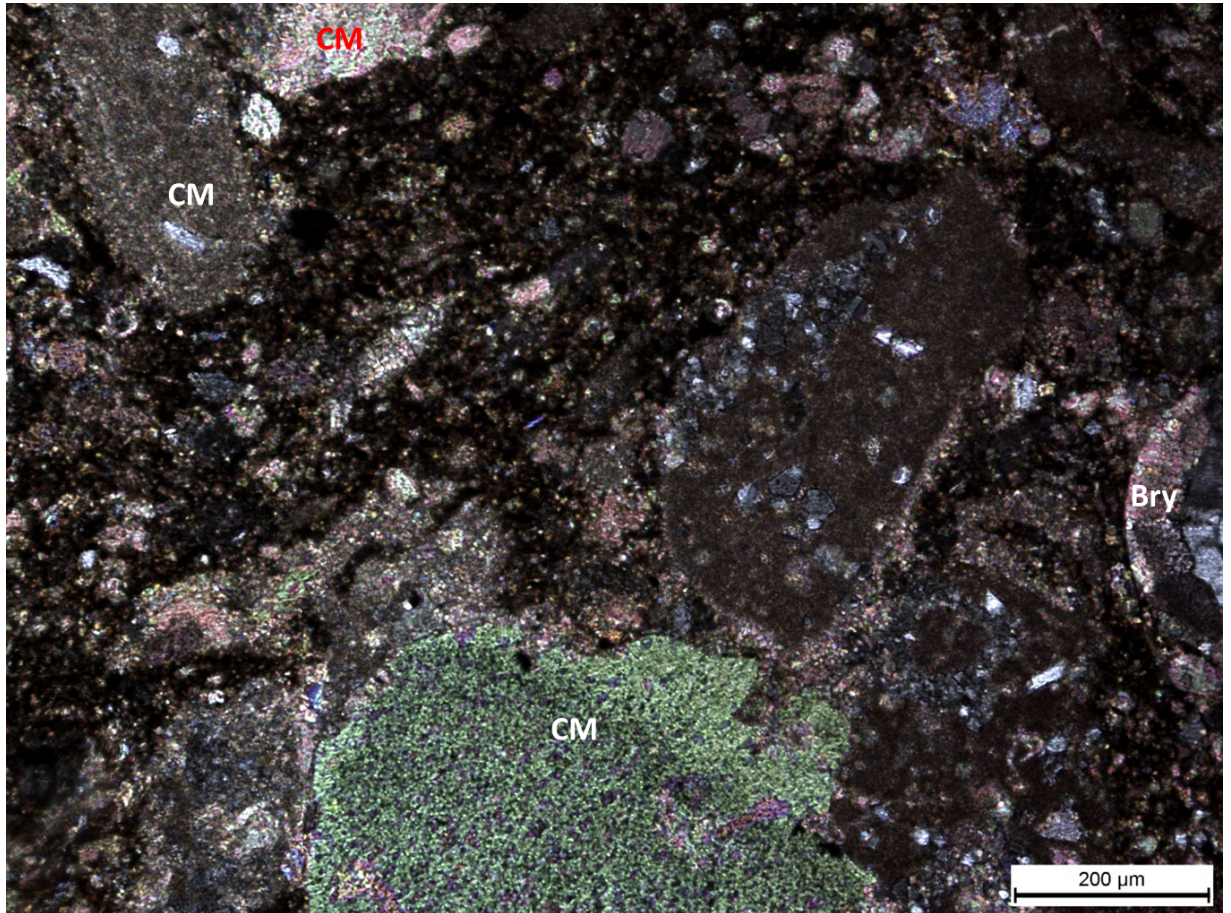
Figure 45: Thin section photomicrograph in cross-polarized light of F4/L3: ripple laminated turbidite (Tc); wackestone. XRD mineralogy of the sample is 78% calcite, 15% quartz, and 2% clay. Carbonate mud intraclasts (CM) are abundant, and a bryozoan skeletal fragment (Bry) are also found in this sample.
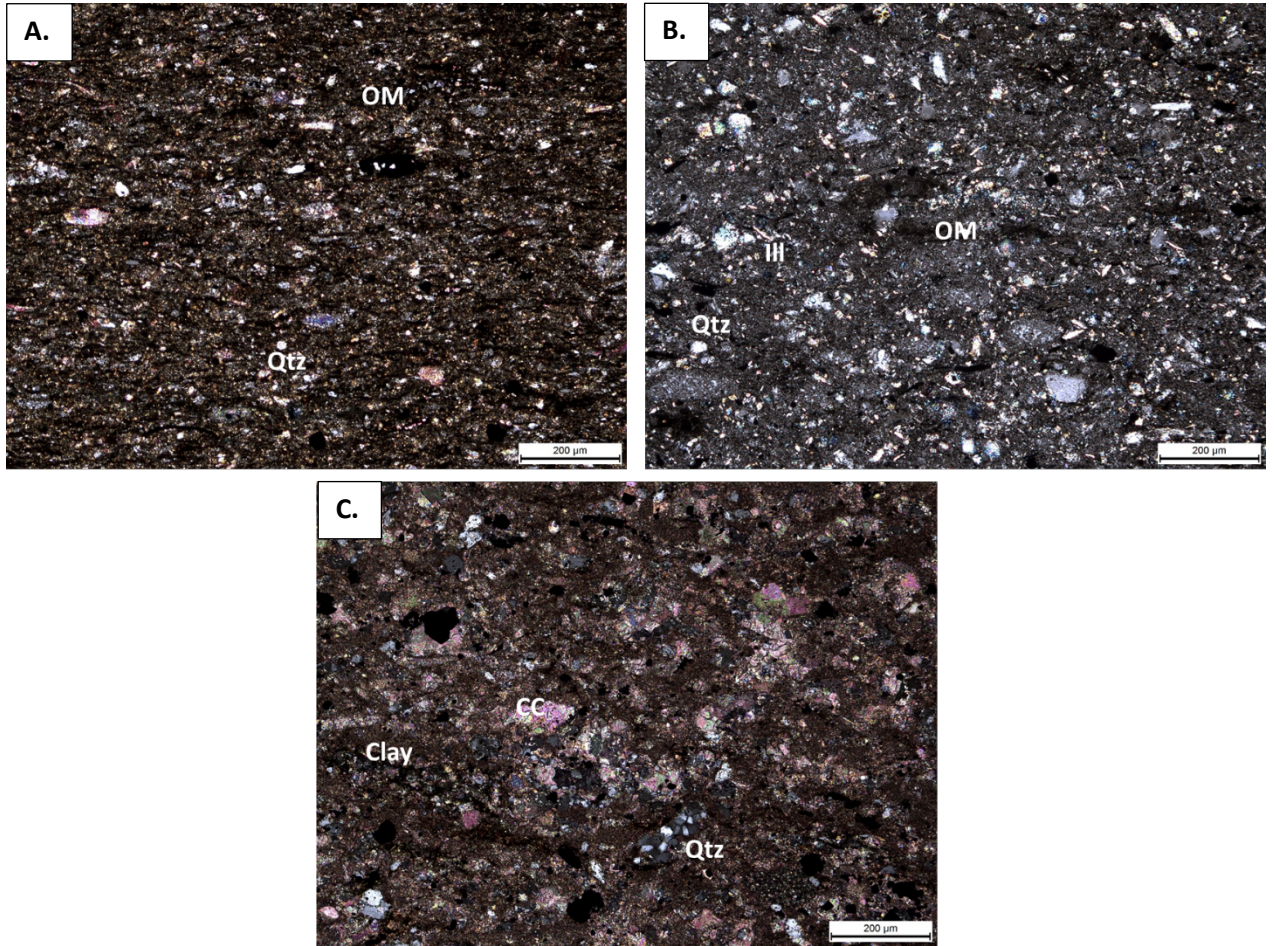
Figure 46: Thin section photomicrographs in cross-polarized light of facies F5, parallel laminated muddy turbidite (Td). Lithologically, images A and B are L1, siliceous mudstone to detrital and biogenic quartz siltstone. These two samples are abundant in quartz (Qtz) and organic matter (OM). Lesser amounts of illite (Ill) are also present. Image C is an argillaceous siliceous mudstone (L2) rich in clays, carbonate cement (cc), and quartz (Qtz).
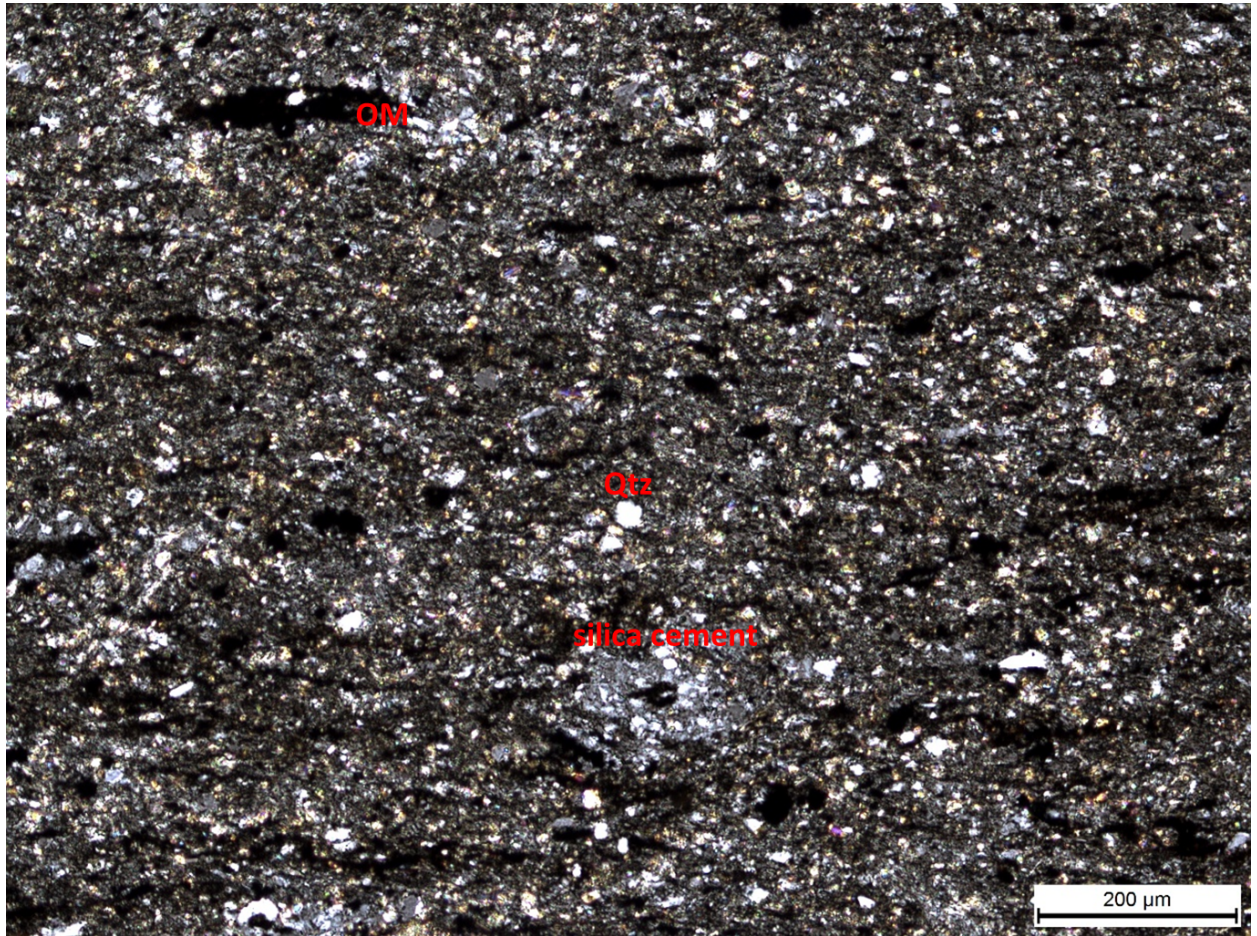
Figure 47: Thin section photomicrograph in cross-polarized light of F6/L1: massive to graded muddy turbidite (Te); siliceous mudstone to detrital and biogenic quartz siltstone. This sample is rich in detrital (Qtz) and amorphous silica cement.
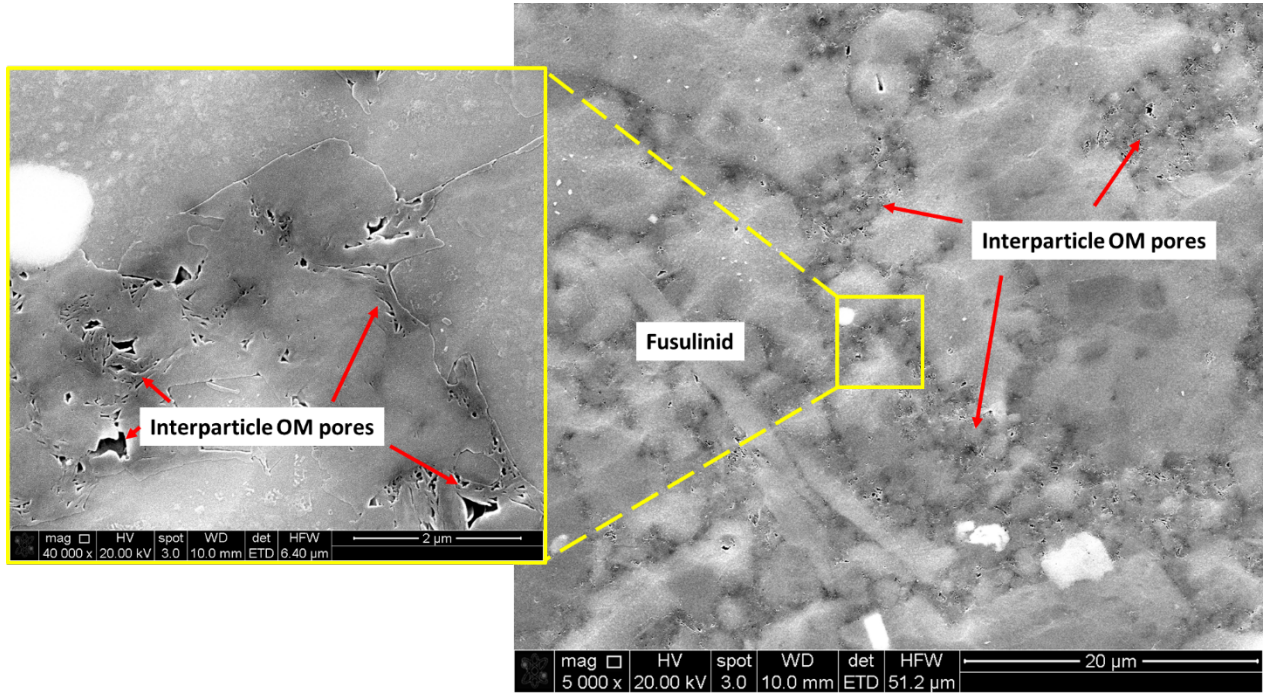
Figure 48: ESEM images of F1/L4: carbonate debrite; intraclastic, skeletal, mud dominated packstone. Interparticle organic matter pores are abundant (sample R 10807.65).
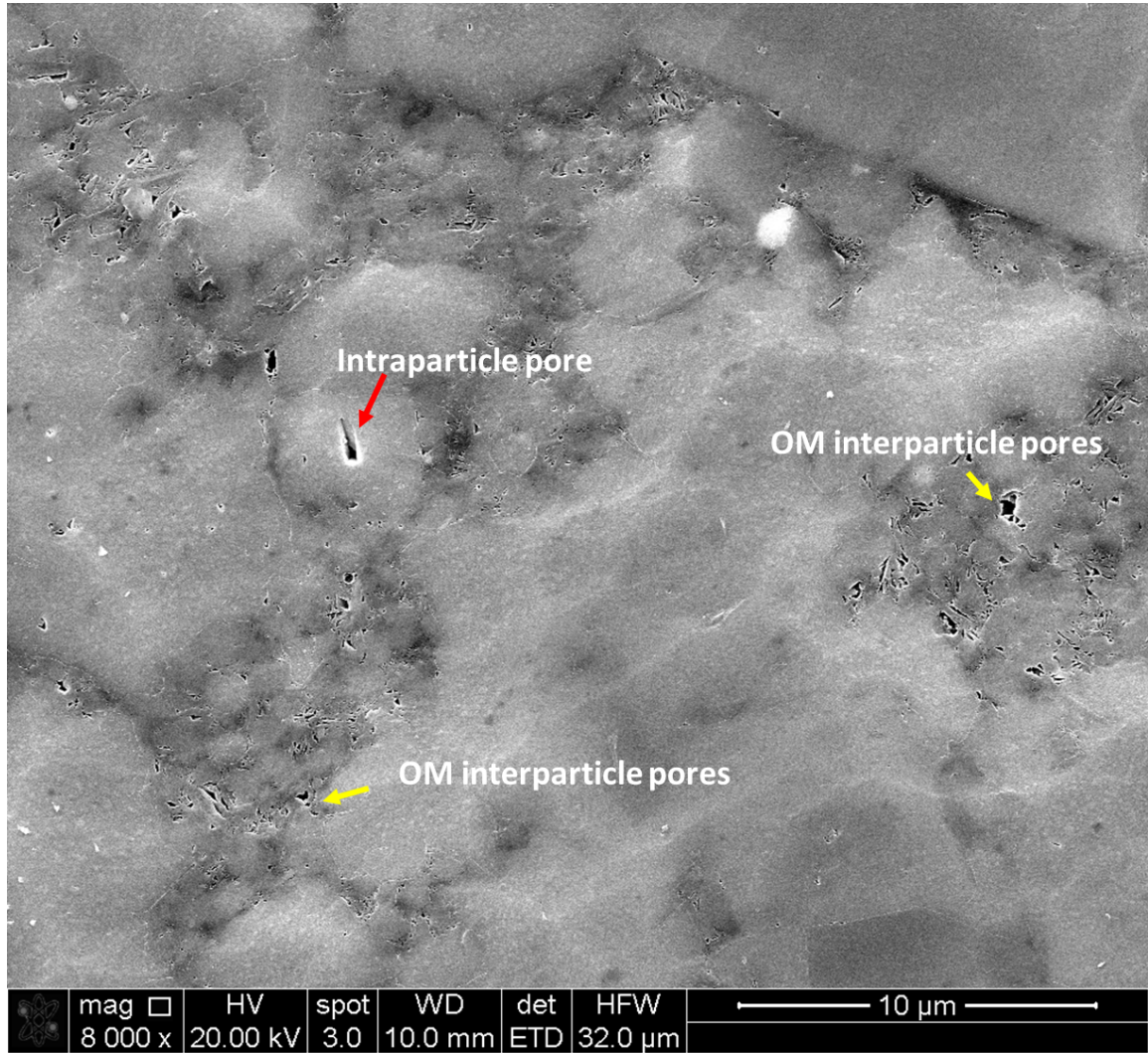
Figure 49: ESEM image of F1/L4: carbonate debrite; intraclastic, skeletal, mud dominated packstone. Interparticle and intraparticle organic matter pores are abundant as well as intraparticle pores in intraclasts (sample R 10807.65).
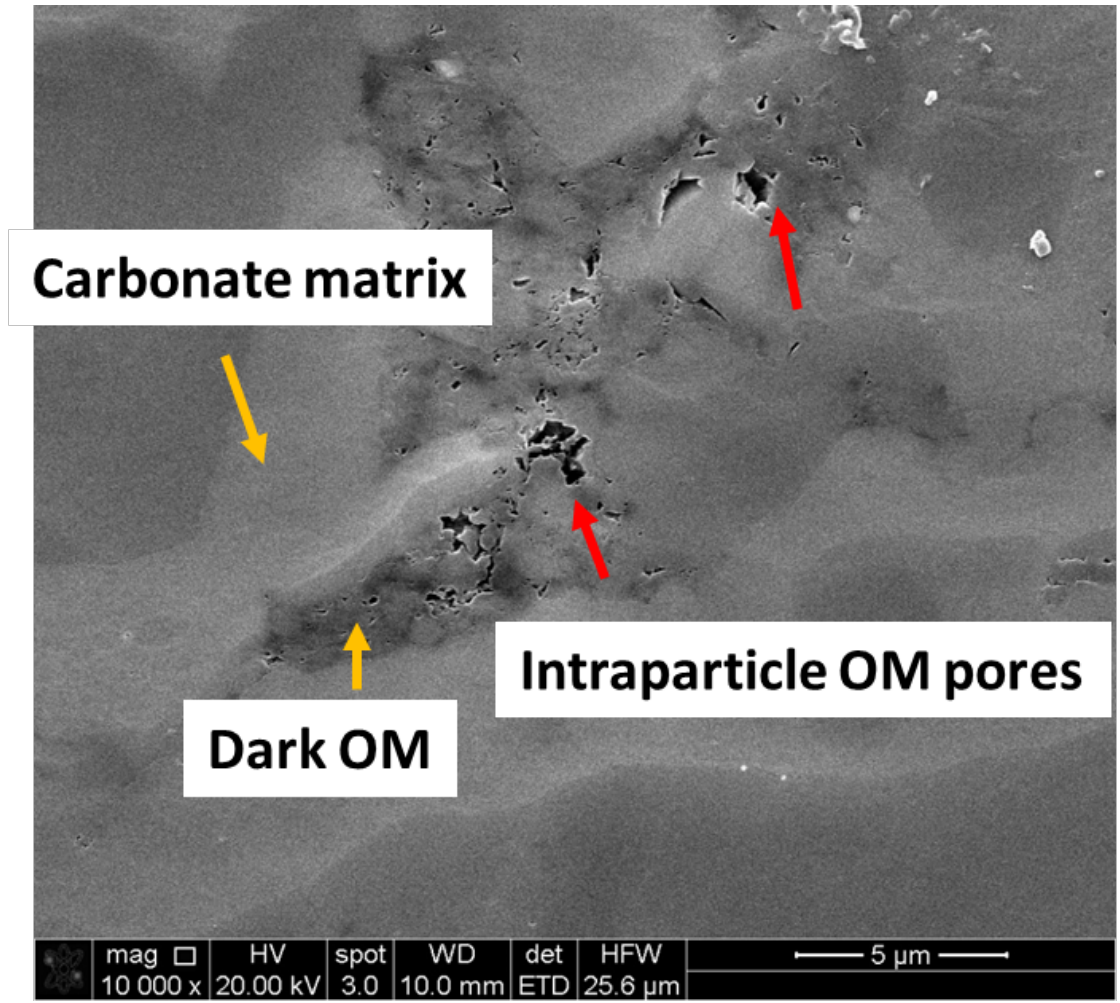
Figure 50: ESEM image of F5/L3: parallel laminated muddy turbidite (Td); carbonate mudstone. Organic matter pores are abundant, and carbonate matrix shows little to no porosity (sample R10583.80).
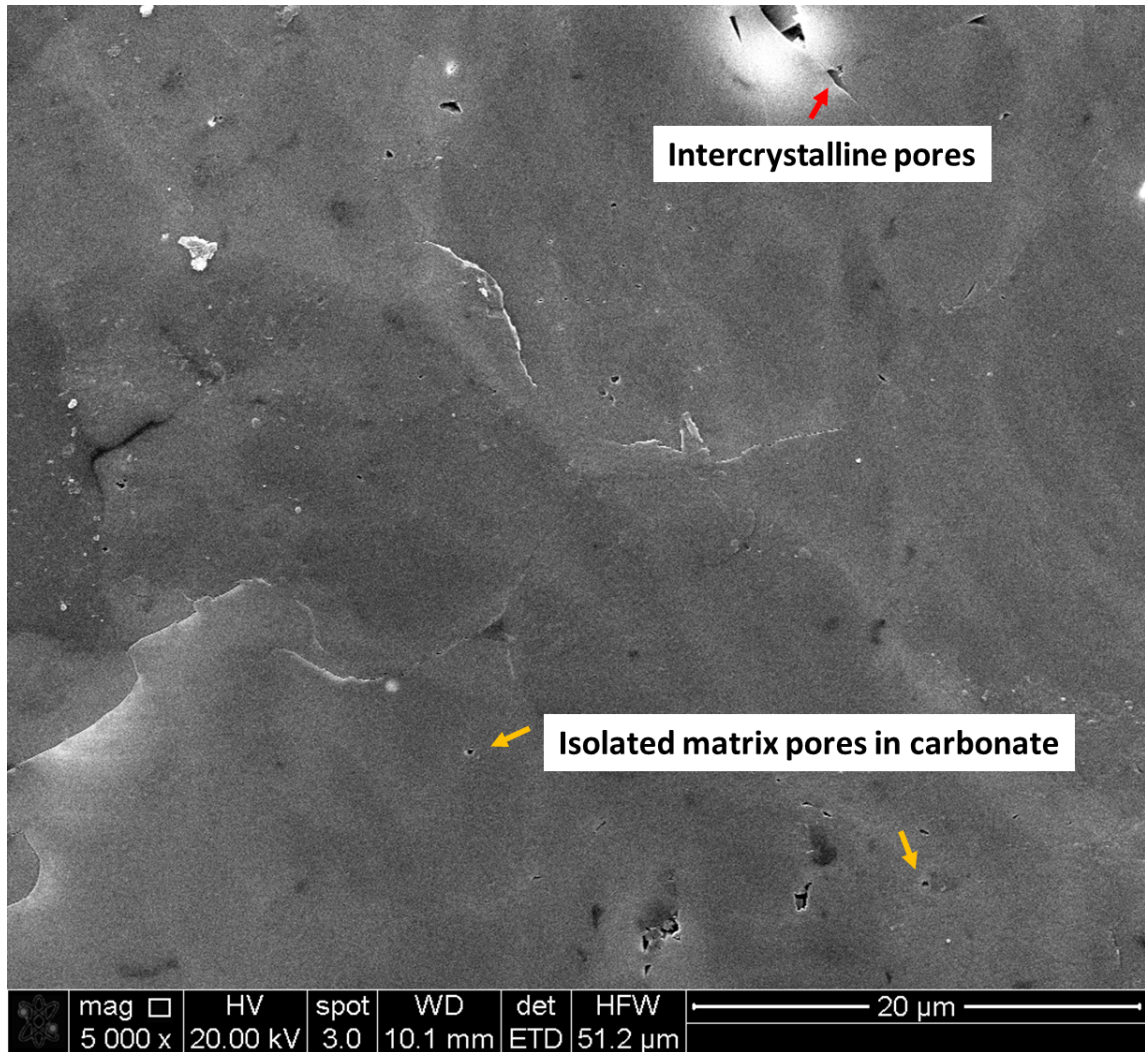
Figure 51: ESEM image of F5/L3: parallel laminated muddy turbidite (Td); carbonate mudstone. Intercrystalline pores between calcite cement and isolated matrix pores are commonly found in this sample (sample R 10583.80).
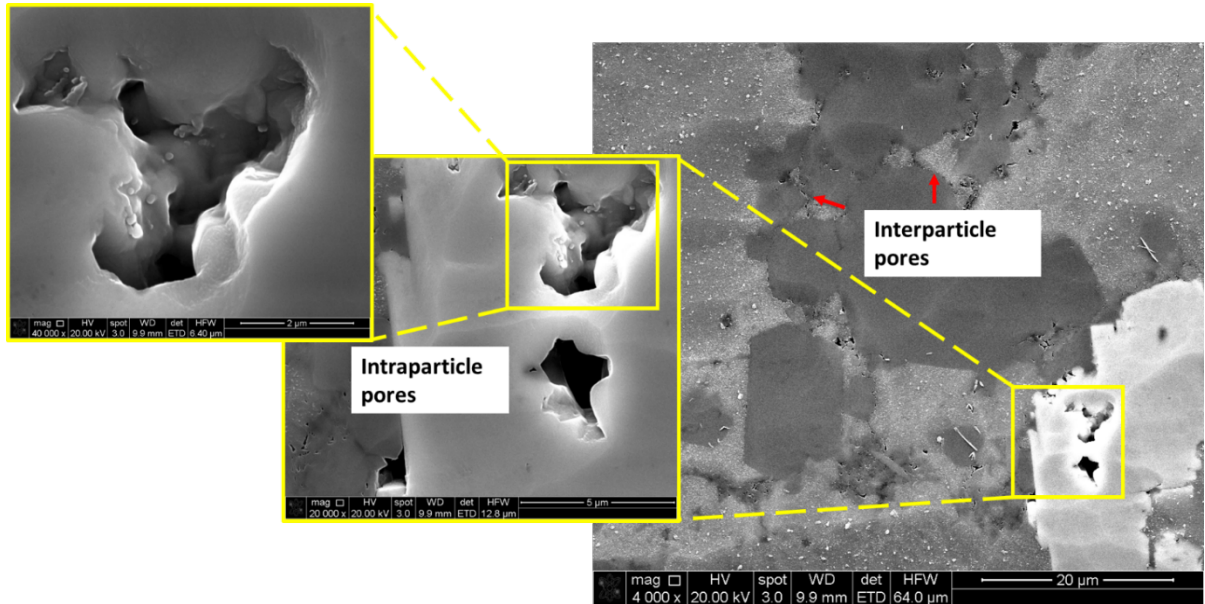
Figure 52: ESEM images of F5/L3: parallel laminated muddy turbidite (Td); carbonate mudstone-siltstone. Interparticle pores between intraclasts and intraparticles inside the intraclasts are abundant (sample R 10635.75).
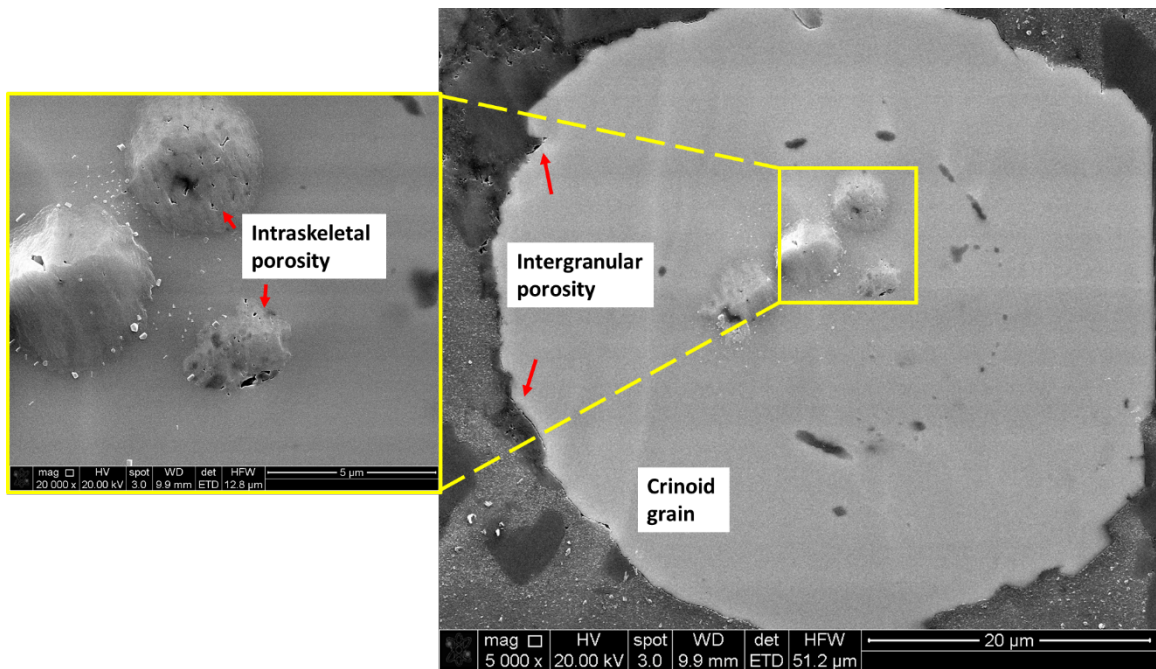
Figure 53: ESEM images of F5/L3: parallel laminated muddy turbidite (Td); carbonate mudstone-siltstone. The image shows nano-scale porosity within a crinoid grain as well as intergranular porosity around the grain (sample R 10635.75).
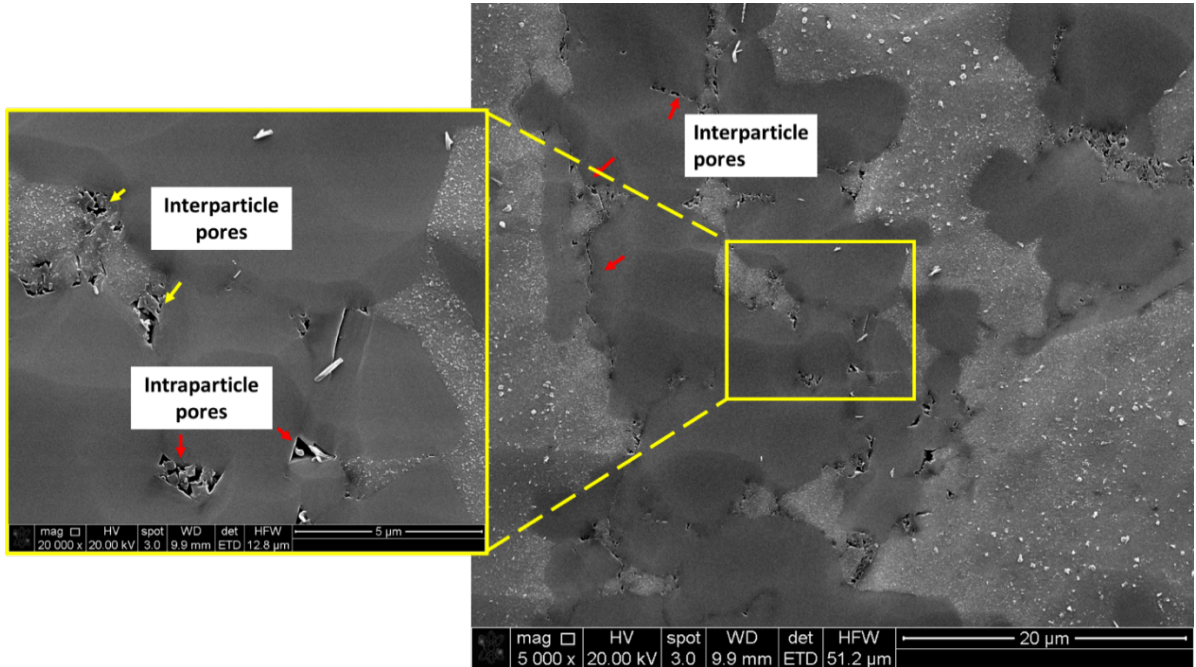
Figure 54: ESEM image of F5/L3: parallel laminated muddy turbidite (Td); carbonate mudstone-siltstone. This sample shows nanometer-scale porosity between intraclasts and inside carbonate mud intraclasts (sample R 10635.75).
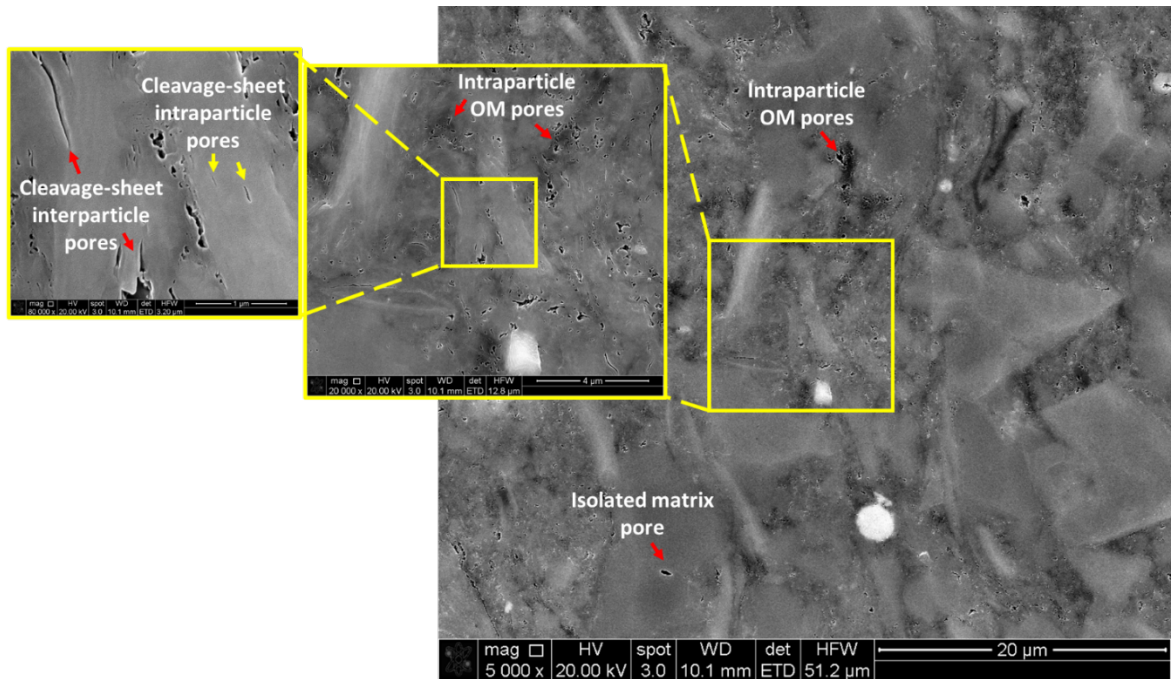
Figure 55: ESEM images of F5/L2: parallel laminated muddy turbidite (Td); argillaceous siliceous mudstone. This sample shows nanometer intraparticle and interparticle organic matter pores and cleavage-sheet pores (sample R 10672.35).
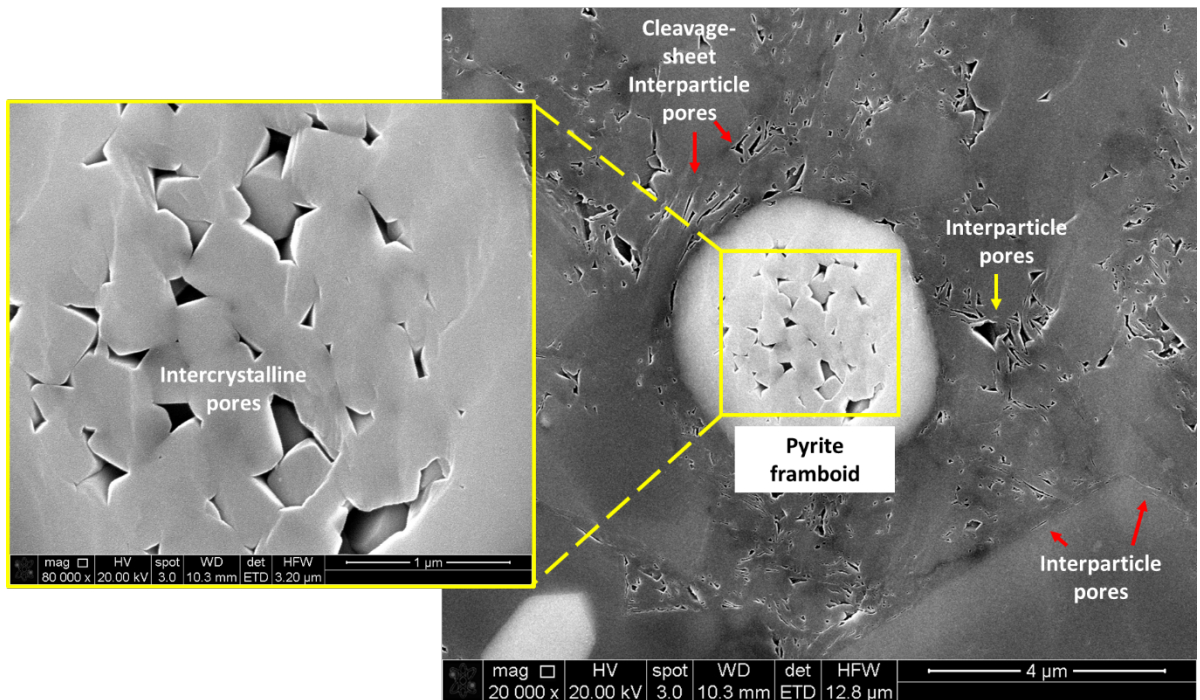
Figure 56: ESEM images of F5/L1: parallel laminated muddy turbidite (Td); detrital and biogenic quartz mudstone-siltstone. This images shows cleavage-sheet interparticle pores, interparticle pores between silica cement, and nanometer intercrystalline pores inside a pyrite framboid (sample R 10728.60).

Figure 57: ESEM Images of F6/L1: massive to normal graded muddy turbidite (Te); siliceous mudstone with calcareous grains. This sample shows intercrystalline pores between silica cement and organic matter pores (sample R 10601.60).

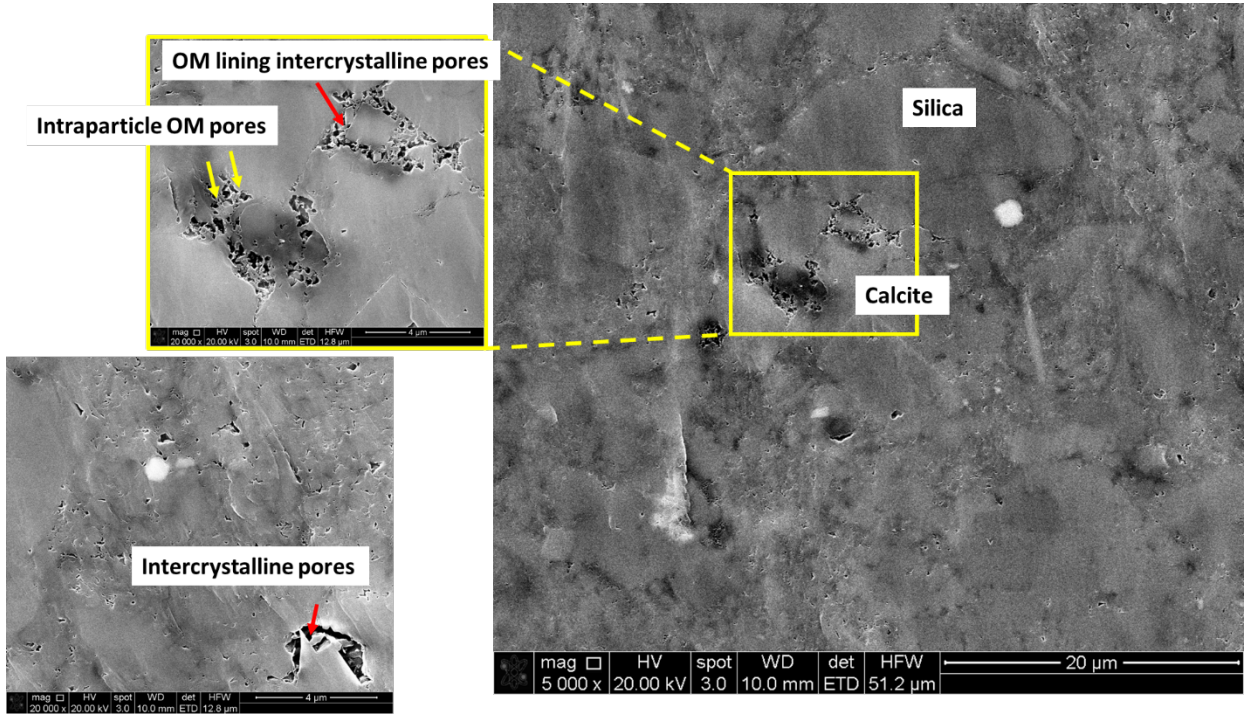| Sample ID	Facies Associations (Primary & Secondary Sedimentation Processes)	Texture/lithofacies (Dunham, 1962)	Illite/ Smectite	Illite & Mica	Chlorite	Total Clay	Calcite	Dolomite (Fe/Ca*)[1]	Quartz	K-spar	Plag.	Pyrite	Apatite	TOC weight %
R 10827.65	Facies 1: Carbonate debrite	intraclastic, skeletal, mud dominated packstone	2	7	Tr	9	53	9	24	Tr	4	1	0	0.35
R 10807.3	Facies 1: Carbonate debrite	intraclastic, skeletal, mud dominated packstone	2	7	Tr	9	47	6	31	1	3	3	0	0.57
R 10817.3	Facies 1: Carbonate debrite	skeletal, grain dominated packstone	3	6	1	10	46	7	30	1	5	1	0	0.48
R 10797.45	Facies 1: Carbonate debrite	intraclastic, skeletal, mud dominated packstone	3	11	1	15	27	14	37	1	4	2	0	0.95
R 10758.45	Facies 1: Carbonate debrite	carbonate mudstone	3	21	Tr	24	17	11	42	1	3	2	0	1.11
R 10734.35	Facies 2: (Ta) Massive, graded turbidite	skeletal wackestone	Tr	1	Tr	1	72	14	10	Tr	2	Tr	Tr	-
R 10737.2	Facies 5: (Ta) Massive, graded turbidite	skeletal wackestone	1	1	Tr	3	53	14	26	Tr	2	1	0	0.24
R 10680.85	Facies 4: (Tc) Convolute or ripple laminated turbidite	ripple cross-laminated wackestone	1	1	Tr	2	78	1	15	Tr	3	1	Tr	-
R 10660.5-10660.80	Facies 5: (Td) Parallel laminated muddy turbidite	heavily bioturbated, planar laminated carbonate mudstone	Tr	2	Tr	2	82	1	10	1	1	3	0	0.34
R 10635.6-10635.90	Facies 5: (Td) Parallel laminated muddy turbidite	planar laminated carbonate mudstone-siltstone	1	3	Tr	4	72	1	19	Tr	3	1	0	1.03
R 10597.45	Facies 5: (Td) Parallel laminated muddy turbidite	bioturbated, planar laminated carbonate mudstone	1	3	Tr	4	70	1	21	Tr	2	2	0	0.68
R 10583.7-10584.00	Facies 5: (Td) Parallel laminated muddy turbidite	planar laminated, carbonate mudstone	3	4	Tr	7	61	4	23	1	3	1	0	0.73
R 10707.8	Facies 5: (Td) Parallel laminated muddy turbidite	planar laminated carbonate mudstone	1	13	1	15	43	4	32	1	3	1	0	1.00
R 10719.6-10719.90	Facies 5: (Td) Parallel laminated muddy turbidite	bioturbated, faintly planar laminated carbonate mudstone	2	17	Tr	19	40	13	21	Tr	5	1	Tr	1.09
R 10667.45	Facies 5: (Td) Parallel laminated muddy turbidite	faintly planar laminated carbonate mudstone	3	18	Tr	21	35	3	30	1	7	2	Tr	2.25
R 10617.15	Facies 5: (Td) Parallel laminated muddy turbidite	bioturbated, planar laminated carbonate mudstone	7	10	1	18	31	1	45	1	3	1	Tr	1.24
R 10587.35	Facies 5: (Td) Parallel laminated muddy turbidite	bioturbated, faintly planar laminated carbonate mudstone	3	18	1	22	29	5	34	1	5	2	1	2.35
R 10717.15	Facies 5: (Td) Parallel laminated muddy turbidite	bioturbated, faintly planar laminated carbonate mudstone	8	16	1	25	27	13	27	1	4	2	Tr	1.24
R 10627.45-10627.75	Facies 5: (Td) Parallel laminated muddy turbidite	planar laminated detrital and biogenic quartz mudstone-siltstone with calcareous grains	6	20	1	27	19	3	41	2	5	2	Tr	3.35
R 10728.45-10728.75	Facies 5: (Td) Parallel laminated muddy turbidite	bioturbated detrital and biogenic quartz mudstone-siltstone/carbonate mudstone	5	20	1	26	17	10	35	2	7	2	1	0.93
R 10637.85	Facies 5: (Td) Parallel laminated muddy turbidite	bioturbated, planar laminated detrital biogenic quartz mudstone-siltstone with calcareous grains	5	20	1	26	11	1	55	1	4	2	0	1.82
R 10607.5	Facies 5: (Td) Parallel laminated muddy turbidite	faintly laminated, fining upwards, argillaceous siliceous mudstone with calcareous grains	5	28	1	34	10	6	36	2	8	3	1	2.74
R 10837.65	Facies 5: (Td) Parallel laminated muddy turbidite	planar laminated argillaceous siliceous mudstone	8	27	1	36	4	3	49	2	5	1	0	1.19
R 10834.05-10834.35	Facies 5: (Td) Parallel laminated muddy turbidite	planar laminated argillaceous siliceous mudstone/carbonate mudstone	6	26	1	33	4	9	39	3	9	2	1	1.94
R 10847.25	Facies 5: (Td) Parallel laminated muddy turbidite	fining upwards, planar laminated argillaceous siliceous mudstone/carbonate mudstone	5	29	1	35	3	4	43	2	10	2	1	2.01
R 10787.6	Facies 5: (Td) Parallel laminated muddy turbidite	heavily bioturbated, planar laminated argillaceous siliceous mudstone	10	22	2	34	2	3	48	2	8	3	0	1.62
R 10777.65	Facies 5: (Td) Parallel laminated muddy turbidite	bioturbated, planar laminated detrital and biogenic quartz mudstone-siltstone	5	24	1	30	1	3	58	1	6	1	0	0.74
R 10747.75	Facies 5: (Td) Parallel laminated muddy turbidite	planar laminated detrital and biogenic quartz mudstone-siltstone	6	20	1	27	1	3	57	3	8	1	0	1.09
R 10766.65	Facies 5: (Td) Parallel laminated muddy turbidite	bioturbated, planar laminated argillaceous siliceous mudstone	7	29	1	37	1	1	49	3	7	2	0	2.36
R 10627.85	Facies 5: (Td) Parallel laminated muddy turbidite	planar laminated argillaceous siliceous mudstone	6	34	Tr	40	1	5	40	3	9	2	0	1.37
R 10672.2-10672.50	Facies 5: (Td) Parallel laminated muddy turbidite	bioturbated, fining upwards argillaceous siliceous mudstone	8	38	2	48	1	3	36	2	8	2	0	2.68
R 10648.3	Facies 6: (Te) Massive to graded muddy turbidite	carbonate mudstone	3	12	1	16	47	5	24	1	5	2	Tr	-
R 10697.8	Facies 6: (Te) Massive to graded muddy turbidite	carbonate mudstone	2	11	1	14	41	6	36	Tr	2	1	0	1.82
R 10557.75	Facies 6: (Te) Massive to graded muddy turbidite	fining upwards carbonate mudstone	2	13	Tr	15	35	2	40	1	4	2	Tr	1.80
R 10577.25	Facies 6: (Te) Massive to graded muddy turbidite	carbonate/siliciclastic mudstone	8	11	1	20	35	3	38	Tr	1	1	1	2.06
R 10647.55	Facies 6: (Te) Massive to graded muddy turbidite	carbonate mudstone	3	22	Tr	25	24	8	30	1	7	3	1	2.02
R 10727.55	Facies 6: (Te) Massive to graded muddy turbidite	argillaceous siliceous mudstone/carbonate mudstone	6	25	Tr	31	15	7	37	1	6	2	1	1.24
R 10601.45-10601.75	Facies 6: (Te) Massive to graded muddy turbidite	fining upwards, quartz rich mudstone with calcareous grains	9	19	1	29	14	5	41	2	5	2	1	2.10
R 10567.2	Facies 6: (Te) Massive to graded muddy turbidite	siliciclastic mudstone	9	17	1	27	11	2	52	1	4	3	0	2.04
R 10677.55	Facies 6: (Te) Massive to graded muddy turbidite	siliciclastic mudstone with calcareous grains	4	27	1	32	9	4	42	2	8	2	1	2.38
R 10687.45	Facies 6: (Te) Massive to graded muddy turbidite	bioturbated, planar laminated argillaceous siliceous mudstone	8	30	1	39	1	3	45	2	8	2	0	0.77

Legend:
- Mud to grain dominated packstone
- Carbonate mudstone-wackestone
- Siliceous mudstone-detrital and biogenic quartz siltstone
- Argillaceous siliceous mudstone

Table 7: Facies associations, texture/lithofacies, XRD mineralogy, and TOC weight % from Core 1. Samples show a heterogeneous range in composition and facies type.

Sample ID	Facies Associations (Primary & Secondary Sedimentation Processes)	Texture/Lithofacies (Dunham, 1962)	Illite/ Smectite	Illite & Mica	Chlorite	Total Clay	Calcite	Dolomite $(Fe/Ca)^{-1}$	Quartz	K-spar	Plag.	Pyrite	Apatite	TOC weight %
A 11363	Facies 1: Carbonate debrite	mud dominated skeletal packstone	2	5	0	7	55	3	31	0	3	2	0	2.60
A 11386	Facies 1: Carbonate debrite	skeletal, grain dominated packstone	2	4	0	6	73	2	16	0	2	2	0	0.96
A 11379.3	Facies 1: Carbonate debrite	skeletal, grain dominated packstone	2	3	0	5	71	2	19	0	2	1	0	1.08
A 11312.25	Facies 2: (Ta) Massive, graded turbidite	planar laminated, pyritic, intraclastic, grain dominated packstone	0	1	0	1	75	3	15	1	2	2	0	0.35
A 11420.8	Facies 3: (Tb) Parallel laminated turbidite	siliceous mudstone-detrital and biogenic quartz siltstone	9	20	0	29	1	9	49	2	7	4	0	1.11
A 11485.7	Facies 3: (Tb) Parallel laminated turbidite	bioturbated, planar laminated siliceous mudstone- detrital and biogenic siltstone	8	17	1	26	1	16	48	1	6	2	0	0.42
A 11478.55	Facies 3: (Tb) Parallel laminated turbidite	planar laminated siliceous mudstone-detrital and biogenic quartz siltstone	7	15	1	24	1	3	63	1	6	2	0	2.62
A 11342.55	Facies 3: (Tb) Parallel laminated turbidite	planar laminated, mud dominated intraclastic packstone	1	3	0	4	54	8	30	0	3	2	0	0.62
A 11350.5	Facies 3: (Tb) Parallel laminated turbidite	fining upwards mud dominated packstone	1	3	0	4	70	4	19	0	1	2	0	1.04
A 11440.5	Facies 5: (Td) Parallel laminated muddy turbidite	planar laminated argillaceous siliceous mudstone	9	20	2	33	0	2	55	0	6	4	0	3.98
A 11389.9	Facies 5: (Td) Parallel laminated muddy turbidite	planar laminated argillaceous siliceous mudstone	8	21	0	32	1	2	49	2	9	5	0	4.91
A 11330.5	Facies 5: (Td) Parallel laminated muddy turbidite	planar laminated argillaceous siliceous mudstone	8	20	0	31	1	5	43	3	11	6	0	5.81
A 11427.6	Facies 5: (Td) Parallel laminated muddy turbidite	bioturbated, planar laminated siliceous mudstone	9	18	0	29	1	2	57	0	6	6	0	2.97
A 11368.5	Facies 5: (Td) Parallel laminated muddy turbidite	planar laminated siliceous mudstone	8	19	0	27	4	3	55	2	7	4	0	2.04
A 11277.7	Facies 5: (Td) Parallel laminated muddy turbidite	planar laminated, siliceous mudstone	9	17	0	26	3	2	51	2	8	7	0	2.91
A 11497.65	Facies 5: (Td) Parallel laminated muddy turbidite	planar laminated siliceous mudstone	7	16	2	26	1	4	59	2	7	3	0	1.80
A 11406.5	Facies 5: (Td) Parallel laminated muddy turbidite	planar laminated siliceous mudstone	7	18	0	26	5	2	53	1	7	4	2	3.33
A 11415.6	Facies 5: (Td) Parallel laminated muddy turbidite	planar laminated siliceous mudstone	8	16	0	25	2	2	56	0	8	4	3	4.33
A 11335.5	Facies 5: (Td) Parallel laminated muddy turbidite	planar laminated siliceous mudstone	6	16	0	24	3	2	57	0	6	5	4	3.96
A 11346.22	Facies 5: (Td) Parallel laminated muddy turbidite	planar laminated siliceous mudstone	6	17	0	24	0	4	62	1	6	4	0	1.31
A 11397.4	Facies 5: (Td) Parallel laminated muddy turbidite	fining upwards, planar laminated siliceous mudstone	7	16	0	22	1	1	59	1	5	3	0	2.19
A 11318.5	Facies 5: (Td) Parallel laminated muddy turbidite	planar laminated siliceous mudstone	6	15	0	22	3	3	57	1	8	6	0	3.64
A 11460.5	Facies 5: (Td) Parallel laminated muddy turbidite	bioturbated, planar laminated siliceous mudstone	6	13	1	21	0	4	66	1	6	2	0	1.61
A 11354.15	Facies 5: (Td) Parallel laminated muddy turbidite	planar laminated siliceous mudstone	6	12	0	20	7	5	49	2	8	6	4	5.25
A 11467.35	Facies 5: (Td) Parallel laminated muddy turbidite	fining upwards, dolomitic siliceous mudstone with siliciclastic intraclasts	5	11	2	18	2	32	37	1	6	4	0	1.72
A 11453.2	Facies 5: (Td) Parallel laminated muddy turbidite	bioturbated, planar laminated siliceous mudstone	1	10	1	13	1	9	72	1	3	2	0	0.80
A 11450.25	Facies 6: (Te) Massive to graded muddy turbidite	argillaceous siliceous mudstone	7	19	2	29	1	4	56	1	6	3	0	3.29
A 11298.75	Facies 6: (Te) Massive to graded muddy turbidite	siliceous mudstone	8	16	0	27	0	3	56	2	7	6	0	6.51
A 11286.5	Facies 6: (Te) Massive to graded muddy turbidite	siliceous mudstone	7	18	0	27	0	4	58	1	7	4	0	2.78
A 11302.3	Facies 6: (Te) Massive to graded muddy turbidite	siliceous mudstone with calcareous intraclasts	6	14	0	21	22	4	42	1	6	5	0	2.87
A 11410.65	Facies 6: (Te) Massive to graded muddy turbidite	fining upwards, carbonate mudstone	1	4	0	6	48	2	40	0	2	1	0	1.75

Table 8: Facies associations, texture/lithofacies, XRD mineralogy, and TOC weight % from Core 2. Samples show a heterogeneous range in composition and facies type.

Legend:
- ■ Mud to grain dominated packstone
- ■ Carbonate mudstone-wackestone
- ■ Siliceous mudstone-detrital and biogenic quartz siltstone
- ■ Argillaceous siliceous mudstone

Sample ID	Facies Associations (Primary & Secondary Sedimentation Processes)	Texture/Lithofacies (Dunham, 1962)	Porosity (%)	Perm. (mD)
R 1075845	Facies 1: Carbonate debrite	carbonate mudstone	8.70	0.001660
R 1079745	Facies 1: Carbonate debrite	intraclastic, skeletal, mud dominated packstone	6.90*	0.0003*
R 108073	Facies 1: Carbonate debrite	intraclastic, skeletal, mud dominated packstone	4.50	0.000830
R 108173	Facies 1: Carbonate debrite	skeletal, grain dominated packstone	4.10*	<.0001*
R 1082765	Facies 1: Carbonate debrite	intraclastic, skeletal, mud dominated packstone	4.00*	<.0001*
R 1073435	Facies 2: (Ta) Massive, graded turbidite	skeletal wackestone	5.20	0.004900
R 107372	Facies 2: (Ta) Massive, graded turbidite	skeletal wackestone	3.50	0.000195
R 10583.7-10584.00	Facies 5: (Td) Parallel laminated muddy turbidite	planar laminated, carbonate mudstone	5.00	0.001380
R 1059745	Facies 5: (Td) Parallel laminated muddy turbidite	bioturbated, planar laminated carbonate mudstone	2.30	0.000083
R 106075	Facies 5: (Td) Parallel laminated muddy turbidite	faintly laminated, fining upwards, argillaceous siliceous mudstone with calcareous grains	10.10	0.002170
R 1061715	Facies 5: (Td) Parallel laminated muddy turbidite	bioturbated, planar laminated carbonate mudstone	7.10	0.001350
R 1062785	Facies 5: (Td) Parallel laminated muddy turbidite	planar laminated argillaceous siliceous mudstone	9.40	0.003000
R 10635.60-10635.90	Facies 5: (Td) Parallel laminated muddy turbidite	planar laminated carbonate mudstone-siltstone	5.00	0.001270
R 1063785	Facies 5: (Td) Parallel laminated muddy turbidite	bioturbated, planar laminated detrital biogenic quartz mudstone-siltstone with calcareous grains	10.80	0.002030
R 1065775	Facies 5: (Td) Parallel laminated muddy turbidite	fining upwards carbonate mudstone	8.10	0.002560
R 10660.50-10660.80	Facies 5: (Td) Parallel laminated muddy turbidite	heavily bioturbated, planar laminated carbonate mudstone	1.40	0.000169
R 1066745	Facies 5: (Td) Parallel laminated muddy turbidite	faintly planar laminated carbonate mudstone	7.90	0.002500
R 10672.20-10672.50	Facies 5: (Td) Parallel laminated muddy turbidite	bioturbated, fining upwards argillaceous siliceous mudstone	11.00	0.002090
R 10707.8	Facies 5: (Td) Parallel laminated muddy turbidite	planar laminated carbonate mudstone	6.50	0.001190
R 1071715	Facies 5: (Td) Parallel laminated muddy turbidite	bioturbated, faintly planar laminated carbonate mudstone	7.60	0.002160
R 10719.60-10719.90	Facies 5: (Td) Parallel laminated muddy turbidite	bioturbated, faintly planar laminated carbonate mudstone	7.40	0.001020
R 10728.45-10728.75	Facies 5: (Td) Parallel laminated muddy turbidite	bioturbated detrital and biogenic quartz mudstone-siltstone/carbonate mudstone	8.40	0.001200
R 1076665	Facies 5: (Td) Parallel laminated muddy turbidite	bioturbated, planar laminated argillaceous siliceous mudstone	11.70	0.001780
R 1077765	Facies 5: (Td) Parallel laminated muddy turbidite	bioturbated, planar laminated detrital and biogenic quartz mudstone-siltstone	12.70	0.001090
R 10787.6	Facies 5: (Td) Parallel laminated muddy turbidite	heavily bioturbated, planar laminated argillaceous siliceous mudstone	9.50	0.002330
R 10834.05-10834.35	Facies 5: (Td) Parallel laminated muddy turbidite	planar laminated argillaceous siliceous mudstone/carbonate mudstone	10.00	0.001080
R 1083765	Facies 5: (Td) Parallel laminated muddy turbidite	planar laminated argillaceous siliceous mudstone	10.60	0.003090
R 1084725	Facies 5: (Td) Parallel laminated muddy turbidite	fining upwards, planar laminated argillaceous siliceous mudstone/carbonate mudstone	10.40	0.002020
R 105672	Facies 6: (Te) Massive to graded muddy turbidite	siliceous mudstone	9.40	0.002590
R 10601.45-10601.75	Facies 6: (Te) Massive to graded muddy turbidite	fining upwards, quartz rich mudstone with calcareous grains	11.00	0.001740
R 10627.45-10627.75	Facies 5: (Td) Parallel laminated muddy turbidite	planar laminated detrital and biogenic quartz mudstone-siltstone with calcareous grains	11.50	0.002520
R 1064755	Facies 6: (Te) Massive to graded muddy turbidite	carbonate mudstone	8.20	0.002990
R 1067755	Facies 6: (Te) Massive to graded muddy turbidite	siliciclastic mudstone with calcareous grains	10.30	0.002580
R 1068745	Facies 6: (Te) Massive to graded muddy turbidite	bioturbated, planar laminated argillaceous siliceous mudstone	11.50	0.003270
R 106978	Facies 6: (Te) Massive to graded muddy turbidite	carbonate mudstone	7.00	0.001220
R 1072755	Facies 6: (Te) Massive to graded muddy turbidite	argillaceous siliceous mudstone/carbonate mudstone	9.60	0.001540

Legend:
- Mud to grain dominated packstone
- Carbonate mudstone-wackestone
- Siliceous mudstone-detrital and biogenic quartz siltstone
- Argillaceous siliceous mudstone

- Dry & Dean Stark Extracted porosity
- Matrix perm., Dry & Dean Stark Extracted

*Dry Helium porosity, NCS
*Klinkenberg perm. NCS

Table 9: Facies, lithofacies, porosity, and permeability values measured from Core 1. Values are sorted by facies type, and colors highlight lithofacies types 1-4.

Sample ID	Facies Associations (Primary & Secondary Sedimentation Processes)	Texture/Lithofacies (Dunham, 1962)	Porosity (%)	Perm. (mD)
A 11363	Facies 1: Carbonate debrite	mud dominated skeletal packstone	*7.41	*n/a
A 11379.00 - 11379.60	Facies 1: Carbonate debrite	skeletal, grain dominated packstone	5.30	0.000022
A 11379.3	Facies 1: Carbonate debrite	skeletal, grain dominated packstone	*4.49	*n/a
A 11386	Facies 1: Carbonate debrite	skeletal, grain dominated packstone	*4.06	*0.000068
A 11312.25	Facies 2: (Ta) Massive, graded turbidite	planar laminated, pyritic, intraclastic, grain dominated packstone	*1.12	*n/a
A 11342.55	Facies 3: (Tb) Parallel laminated turbidite	planar laminated, mud dominated intraclastic packstone	*2.13	*0.311432
A 11420.8	Facies 3: (Tb) Parallel laminated turbidite	siliceous mudstone-detrital and biogenic quartz siltstone	*10.79	*n/a
A 11476.40 - 11476.80	Facies 3: (Tb) Parallel laminated turbidite	bioturbated, planar laminated detrital and siliciclastic clastic siltstone	11.10	0.000507
A 11478.25 - 11478.85	Facies 3: (Tb) Parallel laminated turbidite	planar laminated siliceous mudstone-detrital and biogenic quartz siltstone	13.42	> 0.001
A 11485.40 - 11486.00	Facies 3: (Tb) Parallel laminated turbidite	bioturbated, planar laminated siliceous mudstone- detrital and biogenic siltstone	10.73	0.000949
A 11277.40 - 11278.00	Facies 5: (Td) Parallel laminated muddy turbidite	planar laminated, siliceous mudstone	10.65	0.000493
A 11309.35 - 11309.70	Facies 5: (Td) Parallel laminated muddy turbidite	Planar laminated carbonate mudstone	8.95	0.000293
A 11318.20 - 11318.80	Facies 5: (Td) Parallel laminated muddy turbidite	planar laminated siliceous mudstone	11.07	0.000620
A 11319.60 - 11320.10	Facies 5: (Td) Parallel laminated muddy turbidite	bioturbated, planar laminated siliceous mudstone	9.13	0.000198
A 11330.25 - 11330.75	Facies 5: (Td) Parallel laminated muddy turbidite	planar laminated argillaceous siliceous mudstone	10.19	0.000593
A 11335.20 - 11335.75	Facies 5: (Td) Parallel laminated muddy turbidite	planar laminated siliceous mudstone	11.26	0.000668
A 11345.95 - 11346.50	Facies 5: (Td) Parallel laminated muddy turbidite	planar laminated siliceous mudstone	13.19	> 0.001
A 11350.5	Facies 5: (Td) Parallel laminated muddy turbidite	planar laminated siliceous mudstone	*1.86	*0.000278
A 11353.85 - 11354.40	Facies 5: (Td) Parallel laminated muddy turbidite	planar laminated siliceous mudstone	11.51	0.000761
A 11368.20 - 11368.80	Facies 5: (Td) Parallel laminated muddy turbidite	planar laminated siliceous mudstone	11.89	0.000913
A 11389.60 - 11390.20	Facies 5: (Td) Parallel laminated muddy turbidite	planar laminated argillaceous siliceous mudstone	13.71	> 0.001
A 11397.15 - 11397.65	Facies 5: (Td) Parallel laminated muddy turbidite	fining upwards, planar laminated siliceous mudstone	13.26	> 0.001
A 11415.30 - 11415.90	Facies 5: (Td) Parallel laminated muddy turbidite	planar laminated siliceous mudstone	13.14	> 0.001
A 11427.30 - 11427.90	Facies 5: (Td) Parallel laminated muddy turbidite	bioturbated, planar laminated siliceous mudstone	12.77	> 0.001
A 11440.20 - 11440.80	Facies 5: (Td) Parallel laminated muddy turbidite	planar laminated siliceous mudstone	12.95	> 0.001
A 11440.5	Facies 5: (Td) Parallel laminated muddy turbidite	planar laminated argillaceous siliceous mudstone	*11.61	*0.049147
A 11453.2	Facies 5: (Td) Parallel laminated muddy turbidite	bioturbated, planar laminated siliceous mudstone	*12.81	*0.096823
A 11460.5	Facies 5: (Td) Parallel laminated muddy turbidite	bioturbated, planar laminated siliceous mudstone	*12.47	*0.340395
A 11467.05 - 11467.65	Facies 5: (Td) Parallel laminated muddy turbidite	fining upwards, dolomitic siliceous mudstone with siliciclastic intraclasts	9.66	0.000660
A 11467.75	Facies 5: (Td) Parallel laminated muddy turbidite	fining upwards, planar laminated carbonate mudstone with siliciclastic intraclasts	*11.94	*0.071880
A 11497.65	Facies 5: (Td) Parallel laminated muddy turbidite	planar laminated siliceous mudstone	10.78	>.0001
A 11286.15 - 11286.70	Facies 6: (Te) Massive to graded muddy turbidite	siliceous mudstone	11.36	0.000697
A 11298.45 - 11299.00	Facies 6: (Te) Massive to graded muddy turbidite	siliceous mudstone	11.27	0.000669
A 11302.3	Facies 6: (Te) Massive to graded muddy turbidite	siliceous mudstone with calcareous intraclasts	*6.76	*0.000282
A 11305.7	Facies 6: (Te) Massive to graded muddy turbidite	carbonate mudstone	*5.22	*0.000179
A 11406.20 - 11406.80	Facies 5: (Td) Parallel laminated muddy turbidite	planar laminated siliceous mudstone	13.16	> 0.001
A 11410.65	Facies 6: (Te) Massive to graded muddy turbidite	fining upwards, carbonate mudstone	*6.48	*3.322574
A 11450.00 - 11450.55	Facies 6: (Te) Massive to graded muddy turbidite	argillaceous siliceous mudstone	12.60	0.000891
A 11487.10 - 11487.50	Facies 6: (Te) Massive to graded muddy turbidite	siliceous mudstone	12.83	> 0.001

Table 10: Facies, lithofacies, porosity, and permeability values measured from Core 2. Values are sorted by facies type, and colors highlight lithofacies types 1-4.

Legend:
- Mud to grain dominated packstone
- Carbonate mudstone-wackestone
- Siliceous mudstone-detrital and biogenic quartz siltstone
- Argillaceous siliceous mudstone

- Dry & Dean Stark Extracted porosity
- Matrix perm., Dry & Dean Stark Extracted

*Dry Helium porosity, NCS
*Klinkenberg perm. NCS

VITA

Maria Therese Reistroffer

Candidate for the Degree of

Master of Science

Thesis: DEPOSITIONAL PROCESSES AND RESERVOIR QUALITY OF THE LOWER PERMIAN WOLFCAMP FORMATION IN THE DELAWARE BASIN, WEST TEXAS

Major Field: Geology

Biographical:

Education:

Completed the requirements for the Master of Science in Geology at Oklahoma State University, Stillwater, Oklahoma in May, 2021.

Completed the requirements for the Bachelor of Science in Geology at The University of Texas at Austin, Austin, Texas in 2017.

Experience:

Geoscience Intern at EOG Resources, Oklahoma City, OK- Summer 2019

Professional Memberships:

American Association of Petroleum Geologists
Society for Sedimentary Geology
Association for Women Geoscientists
Geological Society of America
American Institute of Professional Geologists